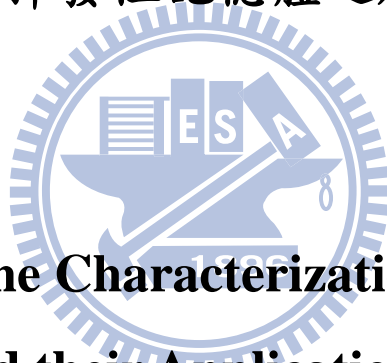# 國 立 交 通 大 學

電子工程學系　電子研究所碩士班

碩 士 論 文

高介電常數材料的特性分析及其在多晶矽奈米線非揮發性記憶體之應用

A Study on the Characterization of High-κ Materials and their Applications to Poly-Si Nanowire Nonvolatile Memory Devices

研 究 生：蘇段凱

指導教授：林鴻志　博士

　　　　　黃調元　博士

中 華 民 國 一 百 年 八 月

高介電常數材料的特性分析及其在多晶矽奈米
線非揮發性記憶體之應用

A Study on the Characterization of High-κ Materials and their Applications to Poly-Si Nanowire Nonvolatile Memory Devices

研 究 生：蘇段凱　　　　　　　Student：Tuan-Kai Su

指導教授：林鴻志　博士　　　　Advisors：Dr. Horng-Chih Lin

　　　　　黃調元　博士　　　　　　　　　　Dr. Tiao-Yuan Huang

國 立 交 通 大 學

電子工程學系　電子研究所碩士班

碩 士 論 文

中 華 民 國 一 百 年 八 月

高介電常數材料的特性分析及其在多晶矽奈米線非揮發性記憶體之應用

研究生：蘇段凱　　　　　　　　　　指導教授：林鴻志 博士

黃調元 博士

國立交通大學

電子工程學系　　電子研究所碩士班

摘要

在本論文中，我們藉由簡單的金氧半(MOS)電容結構，來研究高介電常數(high-κ)材料，包括二氧化鉿(HfO_2)以及氧化鋁(Al_2O_3)的特性。我們改變沉積後高溫退火(post-deposition-annealing)的溫度，來研究其對高介電常數材料的影響。我們發現，對於氧化鋁來說，高溫退火可以使介電常數更高，並降低漏電流；而對二氧化鉿來說，高溫退火亦可以使介電常數上昇，但同時也會使漏電流增加。這是因為在高溫的退火過程中，二氧化鉿會產生結晶的現象。我們也由量測出的數據，去萃取介面缺陷密度，而證實高溫退火可以使介面缺陷密度降低。此外，我們也量測二氧化鉿電容的遲滯現象(hysteresis)，藉以觀察它捕捉電荷的能力。

我們也利用本實驗室最近發展出的多晶矽奈米線製程，來製作奈米線元件，此製程無須使用先進且昂貴的設備，其製作流程簡單且極富彈性。我們採用氧化鋁為阻擋氧化層以及二氧化鉿為電荷捕捉層，來製作 TAHOS 奈米線非揮發性記

憶體元件。相對於以氮化矽為電子捕捉層的傳統元件，TAHOS 元件展現出較佳的驅動電流以及次臨界擺幅(S.S)，此外在寫入/抹除的效率上也有大幅的改善。

在可靠度方面，由於邊角效應(corner effect)的影響，使得大量的介面缺陷產生，因而在經歷忍耐度(endurance)測試後，次臨界擺幅及臨界電壓均會上升。而在電荷保持(retention)方面，預測在經過十年儲存期後，全部的元件均仍可維持 0.5 V 以上的記憶窗。

A Study on the Characterization of High-κ Materials and their Applications to Poly-Si Nanowire Nonvolatile Memory Devices

Student : Tuan-Kai Su

Advisors : Dr. Horng-Chih Lin

Dr. Tiao-Yuan Huang

Department of Electronics Engineering and Institute of Electronics
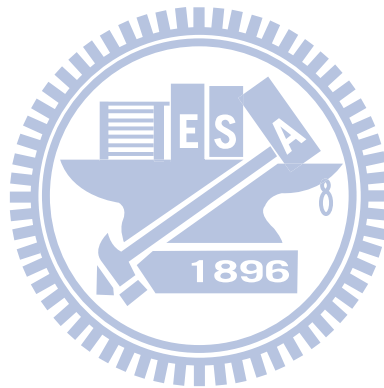
National Chiao Tung University, Hsinchu, Taiwan

Abstract

In this thesis, we have investigated the basic characteristics of two high-κ materials (*i.e.*, HfO_2 and Al_2O_3) with MOS capacitors. The effects of post-deposition-annealing (PDA) temperature on the properties of the dielectrics are studied. For Al_2O_3, a higher temperature tends to provide better film quality and higher permittivity. While for HfO_2, a higher temperature also results in a higher permittivity, albeit the leakage current is also higher because of the film crystallization. The interface trap density is decreased after the PDA treatment. We also exploit the trapping capability of the HfO_2 by studying the hysteresis characteristics of the C-V measurements.

We have also employed a simple and flexible way that was recently developed

by our group to fabricate the NW devices. With the adoption of high-κ materials, a gate-all-around NW TAHOS NVM device was implemented. As compared with the NW SONOS NVM device with the same physical thickness in the dielectric stack, the TAHOS device possesses higher drive current and superior SS owing to the much reduced equivalent oxide thickness. Moreover, NW TAHOS devices also show significantly improved P/E speed.

For endurance test, the SS values of all splits of devices increase with increasing cycles because of the corner effect. The data retention measurements performed on these devices predict that the memory window can be larger than 0.5 V after 10 years at room temperature.

Acknowledgement

Contents

List of Figures

Chapter 2

Chapter 3

List of Tables

Chapter 2

Chapter 3

Chapter 1

Introduction

1-1　Overview of Multiple Gate Structures and Nanowires

The state-of-the-art technology node of semiconductor manufacturing is 28 nm and on the way to 22 nm. As the device scales down to nano scale, the worsened threshold voltage roll-off and degraded subthreshold swing phenomena due to lateral electric field penetration from the drain, known as the short-channel-effects (SCEs), are becoming increasingly more difficult to keep at bay. In order to suppress the SCEs, the adoption of multiple-gated (MG) structures presents a feasible and promising way to enhance the gate controllability [1-5]. A large number of studies and development works on MG structures have been launched, such as double-gated FinFET [1-1], tri-gated (TG) FETs [1-2], Ω-gated FETs [1-3], and gate-all-around (GAA) structures [1-4][1-6][1-8].　In the above-mentioned structures, GAA is demonstrated to be the most ideal configuration considering the channel electrostatic controllability [1-6][1-7][1-8].

Recently, nanowires (NWs) have become an attractive scheme since they exhibit

a range of device functions and at the same time serve as bridging wires. By taking

advantage of the high surface-to-volume ratio inherent in a NW structure, the carrier

transport in it would be promptly influenced by the surface condition. Such a feature

opens up many exciting opportunities for numerous applications. For example, Y. Cui

et al. [1-9] have developed nanowire for high performance field-effect transistors. F.

Patolsky *et al.* [1-10] and Y. Cui *et al.* [1-11] have used nanowire transistors as

biological and chemical sensors because of their high sensitivity. A NW is also

attractive for memory devices because it can provide higher program/erase efficiency

and low voltage operation [1-12].

1-2   Overview of SONOS Flash Memory

Data storage market based on NAND-type flash memory devices has grown

explosively in recent years because of the increasing demands of portable electronic

products. Because the data can be retained when power is switched off, NAND-type

flash memory is widely employed in numerous portable products such as iphone, ipad,

digital cameras, and mp3 players *etc*. In addition, the fabrication process is

compatible with the mainstream CMOS process, making it easily integratable in

electronic systems. In recent years, nonvolatile memory (NVM) devices are moving

forward to meet the demand of high density, low cost, fast operation speed, and good

reliability [1-13]. In this regard, the scaling of NAND-type flash memory has been aggressively pursued in recent years [1-14]. Although floating-gate (FG) flash memory is still the work horse of the market today, FG flash memory devices are vulnerable to single defect in the tunnel oxide which could result in fatal data loss [1-15]. This, together with the FG coupling issue [1-16], has seriously limited the future scaling of the FG devices. Recently, the SONOS devices have thus emerged as a potential candidate for replacing the FG devices as the future main-stream NVM due to their inherent merits, such as the capability of using thinner tunnel oxide and thus lower operation voltage, and the immunity to gate coupling issue [1-17]. The main difference between FG and SONOS devices is the type of charge storage medium. Unlike conventional FG devices, the electrons are stored in discrete traps of nitride-based dielectric in SONOS and are not susceptible to the defects in the tunnel oxide generated during operation. Hence the SONOS exhibits better tunnel oxide reliability than FG [1-18].

Today, polycrystalline thin film transistors (poly-Si TFTs) SONOS have attracted much attention for the purpose of high density storage applications [1-19]. However, there are still some challenges to be addressed such as low memory speed and poor subthreshold swing (S.S.) in poly-Si TFTs [1-20]. By utilizing nanowire (NW) TFT structure, further improvement in S.S. and reduction of leakage current could be

achieved [1-20]. Improved NVM characteristics have also been demonstrated in poly-Si NW SONOS-TFTs [1-20]. Such SONOS-TFT is thereby highly promising for future system-on-panel display applications.

1-3 Overview of High-κ Applications

As the FG NVM facing the scaling limit, the SONOS memory has turned out to attract much attention. However, there still exist some issues in scaling for the SONOS [1-20]. For example, although a thicker tunnel oxide is more reliable in retention, it would degrade the erase efficiency. Although band-to-band tunneling hot hole injection (BTBHHI) is effective for erasing with thick tunnel oxide, it is not suitable for NAND-type Flash as it makes the device vulnerable to the side effects brought about by the hot holes [1-21]. For higher program/erase efficiency, an ultra-thin tunnel oxide is preferable. However, thinner tunnel oxide will cause data retention concern [1-18]. Such a dilemma could be addressed with the implementation of high-κ materials and metal gate electrodes [1-22]. In order to achieve faster memory characteristics, a substantial amount of research works have been established on MONOS (Metal-SiO_2-Si_3N_4-SiO_2-Silicon)-type memory devices [1-14], including engineering of gate electrode [1-23], blocking oxide [1-23][1-24], trapping layer [1-25][1-26][1-27], and even tunnel oxide [1-26]. In charge trapping memories, the

charges are stored in discrete traps of the storage medium. High dielectric constant

(high-κ) materials such as HfO_2 [1-20], Al_2O_3 [1-28], La_2O_3 [1-29] and ZrO_2 [1-30]

are known to possess higher trap density, and thus considered as suitable materials for

charge-trapping layers. On the other hand, gate injection electron current is

undesirable during erase operation, so high-κ materials like Al_2O_3 is adopted to reduce

the electric field across the blocking oxide. Finally, the adoption of high work

function metal gates increases the barrier height for electrons and hence also reduces

the electron injection probability from the gate. From this point of view, metal gate

electrodes such as TiN and TaN with a work function higher than the commonly-used

n^+-poly-Si are widely employed [1-26][1-31]. By combining the above advantages, a

new device called TAHOS ($TiN-Al_2O_3-HfO_2-SiO_2-Si$) structure has been proposed for

next-generation NVM devices [1-32]. The utilization of high-κ dielectrics in such a

scheme will further reduce the effective-oxide-thickness (EOT) and favors the device

scaling trend.

1-4 Motivation

For the next-generation flash memory, high operation speed and high density are

desirable. As have been pointed out in previous work [1-33], a nanowire transistor

wrapped with ONO/gate stacks outperforms the planar one in speed and stays fair in

reliability concerns. But the memory window may be limited by the nitride-based charge trapping mechanism. So in this thesis we explore the feasibility of using high-κ materials as an alternative and *hope* to find some useful candidates which contain high trap density to improve the memory window. Moreover, owing to the inherent characteristics of high dielectric constant materials, operation speed can be improved because of the thinner EOT. To further promote the device performance, we also employ high work function metal gate to reduce the gate injection current during the erasing process. Accordingly, SONOS-like charge trap memory devices with combination of the above-mentioned features are fabricated and characterized in this study with an aim at improving the memory characteristics.

1-5　Organization of this Thesis

In this thesis, a general background of polysilicon nanowire transistors, SONOS memory and high-κ materials are introduced in Chapter 1. In Chapter 2, we investigate devices with a simple MOS structure to investigate the characteristics of high-κ materials. In Chapter 3, a TAHOS nanowire transistor is presented, and we will discuss the memory characteristics of the fabricated devices. In Chapter 4, we will summarize all we observed and make brief conclusions. Finally, some suggestion will be proposed for the future work.

Chapter 2

Fabrication and Characterization

of High-κ MOS Capacitors

2-1 Brief Introduction of Atomic Layer Deposition

Recently, the scaling of complementary metal-oxide-semiconductor (CMOS) transistors has reached nano-scale regime, which requires ultra-thin gate silicon dioxide (SiO_2) to obtain desirable device performance. However, continuous shrinkage of the silicon dioxide would lead to undesirable gate leakage current. Accordingly, it is necessary to look for new materials with higher dielectric constant (κ) to replace the conventional SiO_2 with a physically thicker layer. A list of promising candidates is shown in Table 2.1 [2-1]. For the demand of ultra thin oxide and thickness uniformity, atomic-layer-deposition (ALD) has been adopted to meet these requirements. ALD was first developed in the 1970s with the name of atomic-layer-epitaxy (ALE), and was used for thin-film electroluminescent (TFEL) flat panel applications [2-2]. Nowadays ALD is getting more attraction as a result of decreasing device dimensions and increasing aspect ratio in integrated circuits (ICs), due to its excellent surface control and self-limiting growth mechanism.

The growth of ALD is composed of alternate pulsing of the precursor gases onto the substrate surface and subsequent chemisorption of the precursors. The reactor is

purged with an inert gas between the precursor pulses. Therefore, a typical ALD process can be simply described as follows: (a) Exposure of the first precursor, (b) purge of the reaction chamber, (c) exposure of the second precursor, and (d) a further purge of the reaction chamber. These four basic steps constitute one cycle of ALD process, and only a monolayer will be deposited in one cycle. So the film thickness can be accurately controlled by this self-limiting mechanism. Another advantage of ALD is the superior step coverage which is conducive to excellent conformal deposition on extremely non-planar surface topographies [2-3, 2-4, 2-5]. Owing to these inherent characteristics of ALD, it becomes a promising candidate in nano-scale IC processing. In this thesis, we employed ALD in our process for a precise thickness control of high-κ layers.

2-2 Device Structure and Process Flow of the MOS Capacitors
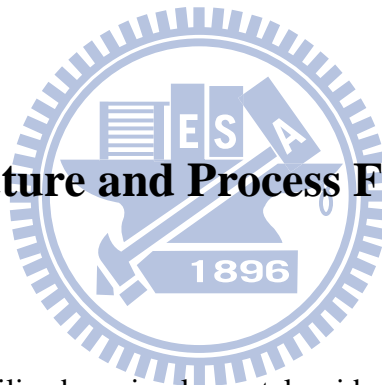
In this thesis, we utilized a simple metal-oxide-silicon (MOS) structure to investigate the characteristics of high-κ layers. First, we used 6-inch p-type (100) bare silicon wafers as starting substrates [Fig. 2.1(a)], with resistivity in the range of 2 to 7 $\Omega \cdot$ cm. After RCA clean, the wafers received a rapid-thermal-oxidation (RTO) at 500 ^{o}C for 10 sec to form an interfacial layer [Fig. 2.1 (b)]. The thickness of the interfacial layer is approximately 1 nm **as** measured by an ellipsometer. In the subsequent step, we used an ALD system to deposit the high-κ layer immediately [Fig. 2.1(c)]. For studying the influence of different post-deposition-anneal (PDA) temperatures, we manufactured different splits of samples. The detailed experiment split table is shown in Table 2.2. Then we used physical-vapor-deposition (PVD) to deposit Al-Si-Cu of

500 nm as the top gate material, followed by a photolithographic step to generate phototresist patterns of gate electrodes, and then using a mixture of acetic acid, phosphoric acid, and nitric acid to remove the exposed Al-Si-Cu and define the gate electrode [Fig. 2.1(d)]. In the final step, we also employed PVD to deposit Al-Si-Cu of 500 nm to serve as the back electrode [Fig. 2.1(e)] to accomplish the MOS capacitors. Capacitance-voltage (C-V) and current-voltage (I-V) measurements were then utilized to probe the characteristics of the high-κ layers.

2-3 Measurement Setup and Electrical Characterization

The C-V and I-V characteristics were evaluated by an automated measurement setup constructed by HP 4156A and Agilent 4284A precision semiconductor parameter analyzers, Agilent TM 5250A switch, and the Interactive Characterization Software (ICS). During the measurements, the temperature was controlled at a stable value by a temperature-regulated chuck.

During the C-V measurements, because of the concern of high leakage current from the high-κ layer, we adopted parallel equivalent circuit model. The frequency of measured capacitance was varied from 5k to 500k Hz. After the measurements, we used the following equation to extract the capacitance-equivalent-thickness (CET) of the high-κ layers,

$$CET = \frac{\varepsilon_0 \varepsilon_{SiO2} A}{C_{acc.}}. \qquad \text{(Eq. 2-1)}$$

In the above equation, A means the area of the measured capacitor, and the value is 1.52×10^{-3} cm^2 in this study. $C_{acc.}$ represents the accumulation capacitance of the

capacitor. ε_0 and ε_{SiO2} indicate the permittivity of vacuum and silicon dioxide, respectively. We also measured the gate leakage current density of the capacitor to analyze the influence of different PDA temperatures.

On the other hand, as a high series resistance, R_s, exists in the capacitor, the measured capacitance would have a deviation from the true oxide capacitance [Fig. 2.2] [2-6]. This deviation is getting larger with increasing measurement frequency [Fig. 2.3 (a)]. This effect can be resolved by using the following equations to calibrate the measurement results:

$$C_c = \frac{(G_m^2 + \omega^2 C_m^2)C_m}{a^2 + \omega^2 C_m^2},$$ (Eq. 2-2)

and

$$G_c = \frac{(G_m^2 + \omega^2 C_m^2)a}{a^2 + \omega^2 C_m^2},$$ (Eq. 2-3)

where C_c, C_m, G_c, G_m are the calibrated capacitance, measured capacitance, calibrated conductance, and measured conductance, respectively,   is the frequency, and $a = G_m - (G_m^2 + \omega^2 C_m^2)R_s$. R_s can be written as the following equation:

$$R_s = \frac{G_{acc}}{G_{acc}^2 + (\omega C_{acc})^2}.$$ (Eq. 2-4)

Here we use the MOS capacitor with HfO$_2$ of 5 nm and annealing at 500 ^{o}C for 30 s as an example [Fig. 2.3 (a)~(d)]. As we can see, the capacitance and conductance are strongly affected by the series resistance [Figs. 2.3 (a), (c)]. After calibration, difference among the capacitances measured at different frequencies would become much smaller [Fig. 2.3 (b)], and the lost conductance peak in Fig. 2.3 (c) appears again [Fig. 2.3 (d)]. The re-appearance of normal conductance characteristics allows us to extract the interface trap density. The conductance method was first proposed by Nicollian and Goetzberger in 1967 [2-7]. Hill *et al.* further developed a single

frequency approach for interface-state density approximation in 1980 [2-8]. We used the following equation to extract the interface trap density [2-9],

$$D_{it} = \frac{2}{qA} \frac{G_{c,\max} / \omega}{[(G_{c,\max} / \omega C_{ox})^2 + (1 - C_c / C_{ox})^2]}. \qquad \text{(Eq. 2-5)}$$

Here, $G_{m,\max}$ indicates the maximal value of the measured conductance, and C_c is the corrected capacitance along with the $G_{c,\max}$.

In addition, we also measured the hysteresis phenomena to study the trapping characteristics of the high-κ layers. The measurement was executed by first sweeping gate voltage from 3 V to -3 V and then sweeping back to 3 V.

2-4 Device Characteristics of MOS Capacitors

2-4.1 Basic Material Analyses

First, we utilized X-ray diffraction (XRD) to characterize the micro-structural properties of the HfO$_2$ samples with various film thickness and PDA temperature. As shown in Fig. 2.4, the as-deposited samples appear to be amorphous in nature as expected, while the annealed samples show evidence of the crystalline phase. This phenomenon has received much attention because the adoption of high-κ materials is an important topic for IC industry in recent years [2-10]. It is clearly found that the PDA temperature exhibits strong influence on the crystalline properties of the HfO$_2$ films. That is, the film exhibits more crystalline phases with increasing PDA temperature. It is also noteworthy that for the thicker HfO$_2$, the XRD results reveal more crystalline phases, possibly due to more nucleation sites contained in the thicker film. Unfortunately, for logic devices, the crystalline structure of the dielectric may

aggravate gate leakage. But this phenomenon could be beneficial for memory applications, as will be discussed in the following sections.

2-4.2   Fundamental J-V and C-V Characteristics of MOS Capacitors

In this section, we used the samples in Table 2.2 to explore the influences of PDA temperature and duration. The capacitance value was corrected by the series resistance effect as mentioned in Section 2-3. First, the samples of Al_2O_3 films with thickness of 5 nm were examined. The capacitance is found to increase with the annealing temperature [Fig. 2.5 (a)], which could be ascribed to the defect repairing during annealing. Accordingly, as the dielectric becomes more robust, the gate leakage current reduces. A dramatic improvement of gate leakage is indeed observed for the sample receiving 900 ^{o}C-30 sec annealing as compared with the as-deposited one [Fig. 2.5 (b)]. When we extend the annealing duration to 60 sec, the capacitance can be further raised [Fig. 2.6 (a)]. This indicates that the annealing time is also an important concern for the film quality. However, the leakage current increases as the annealing time is increased from 30 to 60 sec, as depicted in Fig. 2.6 (b). This may be due to the occurrence of the Al_2O_3 film crystallization with longer annealing time. Extra leakage current paths likely appear at the crystallized grain boundaries [2-11]. Moreover, the samples with 5 nm-HfO_2 are also investigated. As the C-V curves shown in Fig. 2.7 (a), the as-deposited film shows higher capacitance than the sample with 500 ^{o}C-30 sec annealing, which may be resulted from the oxygen diffusion to the interface during the annealing, thus leading to a thicker interfacial layer. However, as the annealing temperature increases, a higher capacitance value is observed which is

attributed to the improved film quality with higher dielectric constant [Fig. 2.7 (a)]. On the other hand, the J-V curves in Fig. 2.7(b) exhibit higher leakage current for the as-deposited film, compared with the samples receiving high temperature annealing, which can be ascribed to the interfacial layer growth effect, [2-12]. Nevertheless, when comparing the samples receiving different annealing temperatures, a slightly increased leakage current with higher PDA temperature is observed. Higher temperature also favors film crystallization, as shown in Fig. 2.4, and therefore resulting in a higher leakage [2-13]. For a thicker sample (10 nm), the trends in C-V characteristics [Fig. 2.8 (a)] are similar to those observed in [Fig. 2.7 (a)]. But it is interesting to see that the leakage current of the as-deposited sample is lower than the annealed ones [Fig. 2.8 (b)]. This implies that the film crystallization extent turns out to be the dominant factor in the present case, which is also evidenced from the XRD results as revealed in Fig. 2.4.
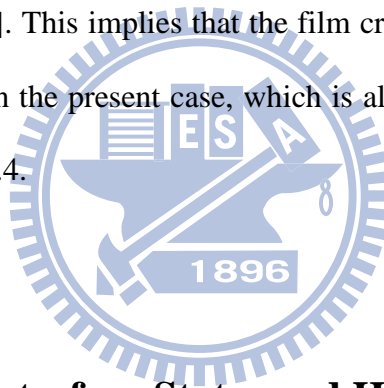
2-4.3   Analyses of Interface States and Hysteresis Phenomena

Thermally grown SiO_2 is usually treated as an ideal dielectric when contacting with the silicon substrate. Actually, the measured electrical characteristics are affected by some positive charges near the silicon/SiO_2 interface or trap charges in the bulk oxide. Other types of charges are either positive or negative ones trapped by interface states and mobile ionic charges which are generated during the fabrication process [2-14]. The electrical properties of devices are very sensitive to the interface state density (D_{it}). The interface states are located at or very close to the semiconductor/oxide interface with energy distributed along the bandgap of the

semiconductor. These states may trap electrons or holes at the interface and then become charged. All the charged states can be taken as interface charges (Q_{it}). When a high-κ material is used as the gate dielectric, the concern of interface state becomes more important. Moreover, formation of the interfacial layers is usually inevitable when using high-κ materials in semiconductor fabrication because of the existence of high temperature process step in the following manufacturing procedure. When high-κ materials are first introduced, people simply accept such interfacial layer that grows naturally after the deposition of high-κ materials. But in recent years, it has been recognized that high D_{it} associated with such interfacial layer will seriously aggravate the electrical properties. In line of this, nowadays people are apt to intentionally deposit an interfacial layer with desirable quality before the high-κ film deposition [2-15]. In our experiment, a RTO oxide layer was formed prior to the high-κ film deposition. The forming condition was conducted in O_2 (with 10 % N_2) atmosphere at 500 ^{o}C for 10 s. And then the D_{it} was extracted by the conductance method with single frequency approximation [2-5]. Just like many data proposed before, the D_{it} of as-deposited HfO_2 is in the order of 1E12 to 1E13 (eV^{-1}cm^{-2}) [2-16]. After the PDA treatment, the D_{it} decreases significantly [Fig. 2.10]. Although the major gas is N_2 during PDA, there still exists approximately 5 % O_2 presenting in the chamber. It is possible that the oxygen can diffuse to the interface to improve the interface quality. When the temperature rises from 500 ^{o}C to 800 ^{o}C, the D_{it} increases slightly. This may result from the fact that the coefficient of thermal expansion (CTE) of HfO_2 ($6.5\times10^{-6} K^{-1}$) [2-17] is much larger than that of SiO_2 ($0.5\times10^{-6} K^{-1}$) [2-18] or Si ($2.6\times10^{-6} K^{-1}$) [2-18]. And another possibility is the diffusion of impurities or defects to this interface [2-19]. Furthermore, the oxygen compensating phenomenon is more obvious for the 5 nm-HfO_2 sample annealed at 900 ^{o}C for 30 sec, in which the

lowest D_{it} can be achieved (6×10^{11} ev^{-1}cm^{-2}) among all the samples.

As abovementioned, there are many kinds of charges in the oxide or oxide/silicon surface. Owing to the innate high defect density, a transistor with high-κ materials tends to have flat-band voltage shift after forward and backward gate voltage sweeping, which is usually called the hysteresis [2-20]. This phenomenon is undesirable for fundamental logic devices but can be exploited for nonvolatile memory applications because of its capability of trapping charges. Therefore, in order to use HfO$_2$ as the charge trapping layer, we preliminarily investigate the hysteresis characteristics of the HfO$_2$ capacitor samples with three different thicknesses. In the measurement, all the samples were operated with the gate bias sweeping from inversion to accumulation and then backward. The sweeping voltage range is ±3 V. We found that the hysteresis increases with increasing film thickness, implying that the number of trapping sites increases with film thickness. Next, the influence of PDA will be discussed. From the XRD data, the HfO$_2$ films have shown signs of crystallization even with the low annealing temperature of 500 ^{o}C. The hysteresis of the 5 nm and 10 nm as-deposited samples are 132 mV and 518 mV, respectively. After 500 ^{o}C-30 sec PDA treatment, the values increase to 270 mV and 840 mV, respectively [Fig 2.11]. This might be due to the incomplete film crystallization during the PDA process and thus more trapping sites generated at intra/inter grains. Another interesting thing is that the hysteresis decreases when we further raise the annealing temperature. From the XRD data, some grain orientations disappear as the annealing temperature is higher. This means the grains became larger at the higher annealing temperature. Therefore, some crystalline defects could be significantly repaired during high temperature annealing.

2-5   Summary

In this chapter, fundamental material and electrical characteristics of high–κ materials are studied. We have successfully fabricated and characterized MOS capacitors with HfO_2 or Al_2O_3 dielectric of different thicknesses. The crystallization of HfO_2 after high temperature annealing was confirmed by XRD data. For Al_2O_3 samples, the crystallization-free annealing temperature could be as high as 800 ^{o}C without causing a high gate leakage. When the annealing time is extended to 60 sec, the dielectric constant can reach a higher value, suggesting the improved film quality. On the other hand, the HfO_2 samples seem to be more vulnerable to the PDA treatment. Annealing at 500 ^{o}C and higher temperatures could reduce the gate leakage significantly owing to more pronounced interfacial layer re-growth for 5 nm-HfO_2 samples. But the HfO_2 thin films also become crystallized during the annealing and the gate leakage is closely affected by the annealing, especially for the thicker HfO_2 samples. D_{it} and hysteresis effects were also probed to discuss the influence of annealing temperature. Based on these results, we opt for 600 ^{o}C/30 sec annealing condition for the high-κ based memory devices and the device characteristics are presented and discussed in Chapter 3.

Tables

Table 2.1.　Potential candidates for gate dielectric of future CMOS technology.

	κ	Band Gap (eV)	CB offset (eV)
Si		1.1	
SiO_2	3.9	9	3.2
Si_3N_4	7	5.3	2.4
Al_2O_3	9	8.8	2.8
Ta_2O_5	22	4.4	0.35
TiO_2	80	3.5	0
$SrTiO_3$	2000	3.2	0
ZrO_2	25	5.8	1.5
HfO_2	25	5.8	1.4
$HfSiO_4$	11	6.5	1.8
La_2O_3	30	6	2.3
Y_2O_3	15	6	2.3
$a\text{-}LaAlO_3$	30	5.6	1.8

Table 2.2.　Split table for MOS capacitors.

	HfO_2			Al_2O_3	
	5 nm	10 nm	15 nm	5 nm	10 nm
PDA	◆	◆	◆	◆	◆
500℃,30s	◆	◆		◆	
600℃,30s	◆	◆	◆	◆	
700℃,30s	◆	◆		◆	
800℃,30s	◆	◆	◆	◆	
900℃,30s	◆	◆		◆	
500℃,60s	◆				
600℃,60s	◆			◆	◆
700℃,60s	◆			◆	
800℃,60s				◆	◆

Chapter 3

Fabrication and Characterization of MAHOS MOS Capacitors and TAHOS NW-Channel TFTs

3-1 Device Structure and Process Flow for Fabricating the MAHOS Capacitors

The structure and layout are the same as those mentioned in Chapter 2, so the description below is brief. The process flows for fabricating different types of capacitors are shown in Fig. 3.1. 6-inch p-type (100) bare silicon wafers were used as starting substrates [Fig. 3.1(a)], with resistivity ranging from 2 to 7 $\Omega \cdot$ cm. Three major structures, namely, MONOS, MANOS, MAHOS, were fabricated and characterized in this experiment and details about the dielectric composition of the splits are shown in Table 3.1. In the MAHOS structure, HfO_2 films deposited at different temperatures are specifically addressed. The major objectives are to reduce the thermal budget and increase the trapping sites in the trapping layer. After RCA cleaning, low pressure chemical vapor deposition (LPCVD) furnace was used to

deposit TEOS oxide with nominal thickness of 3 nm as the tunnel oxide in all devices [Fig. 3.1 (b)]. Afterwards, the atomic layer deposition (ALD) HfO_2 or LPCVD nitride serving as the trapping layer and ALD Al_2O_3 or LPCVD oxide serving as the block oxide were deposited subsequently [Fig. 3.1 (b)]. Then, physical vapor deposition (PVD) was used to deposit 500 nm-thick Al-Si-Cu as the top gate electrode [Fig. 3.1 (c)]. The final step was the deposition of PVD Al-Si-Cu with thickness of 500 nm as the back electrode [Fig. 3.1 (d)].

3-2 Device Structure and Process Flow of the TAHOS NW-TFTs

Fig. 3.2 shows the top and cross-sectional views of the fabricated SONOS-type poly-Si NWFET with gate-all-around (GAA) structure. It can be seen that the NW channels are surrounded by the gate. Figs. 3.3(a) ~ (k) depict the major process steps of fabricating the devices. All devices in this work were fabricated on 6-inch bare silicon wafers capped with a 200 nm-thick wet oxide. First, a 40 nm bottom nitride layer was deposited by LPVCD. Then, a 40 nm TEOS oxide and a 30 nm nitride dummy layer (hard mask layer) were deposited sequentially [Fig. 3.3 (a)]. After a standard I-line lithographic step, the nitride/TEOS dummy layer was patterned by anisotropic reactive plasma etching [Fig. 3.3 (b)]. In this etching step, the etching time was carefully controlled to stop right on the top of the bottom nitride layer. Then, we used diluted HF (DHF) to etch the dummy structure and form rectangular-shaped cavities at both sides of the dummy patterns [Fig. 3.3 (c)]. Note that the size of NW channels could be adjusted by controlling the etching time. After forming the cavities, a 100 nm undoped amorphous-Si (α-Si) was deposited by LPCVD to serve as the

channel material [Fig. 3.3 (d)]. Afterwards, an annealing step was performed at 600 ^{o}C in N$_2$ ambient for 24 hours to transform the α-Si into polycrystalline phase [Fig. 3.3 (e)]. Then by adopting a dry etching step with endpoint detection, the NW channels were formed in the cavities [Fig. 3.3 (f)]. Subsequently, *in situ* phosphorus-doped poly-Si was deposited by LPCVD at 550 $^{\circ}$C and 600 mtorr with the PH$_3$ flux of 15 sccm [Fig. 3.3 (g)]. Then S/D patterns were defined through an I-line stepper, followed by an anisotropic dry etching step to define S/D [Fig. 3.3 (h)]. It should be noted that the devices whose S/D regions are formed by employing *in situ* doping technique show better performance than those formed by ion-implanted poly-Si [3-1]. Afterwards, wet etch steps were used to remove the nitride layer and dummy TEOS with hot H$_3$PO$_4$ and DHF, respectively. In order to form the suspended NW channels hanging between the S/D regions, the bottom nitride was completely stripped off by hot H$_3$PO$_4$ [Fig. 3.3 (i)]. All wafers were then deposited with a 3 nm TEOS oxide as the tunnel oxide. Wafers were then split to form the three major structures in our experiment, For TONOS and TANOS structures, a 7 nm silicon nitride layer was deposited as the trapping layer after the tunnel oxide deposition. The TONOS device was then deposited with a 12 nm TEOS oxide which serves as the block oxide subsequently. For TANOS device, a 12 nm-thick ALD Al$_2$O$_3$ was deposited as the block oxide. While for devices of the third type, ALD was used to sequentially deposit HfO$_2$ and Al$_2$O$_3$ as the trapping layer and block oxide, respectively, after the tunnel oxide deposition [Fig. 3.3 (j)]. In this structure, the deposition temperature of HfO$_2$ was varied from 250°C to 100°C to study its effects on the TAHOS device characteristics. The process conditions are summarized in Table 3.1. Afterwards, a 6 nm TiN was deposited with ALD to serve as the gate for all splits. Owing to the conformity of ALD process, this step was used to ensure the

channel is surrounded by the gate. Next, we adopted PVD to further deposit a TiN of 150 nm to complete the gate electrode. After depositing a 500 nm passivation oxide layer and opening contact holes, a standard metallization step was performed to complete the device fabrication.

3-3   Basic Material Analysis

In this section, we investigate the structural characteristics of the fabricated devices, including MOS capacitors and NWs. All devices with high-κ layers were subjected to a 600°C-30s annealing step. TEM pictures and XRD were employed as the analysis method. Fig. 3.4 (a) is the TEM picture of a TONOS structure and Fig. 3.4 (b) is for a TAHOS device. Because the etching rate is not controlled precisely, the NW dimension is larger than our expectation (actual size is shown in the TEM picture). For the rectangular-shaped NW, the corner will enhance the electric field and affect the electrical characteristics which will be discussed later. Figs. 3.4 (c) ~ (e) depict the TEM images of MOS capacitor stacks. It is obvious that the HfO_2 is evidently crystallized for all the deposition temperatures used. The most interesting thing is that the Al_2O_3 film retains its amorphous nature in the MANOS structure [Fig. 3.4 (c)]. In contrast, the Al_2O_3 film in the MAHOS structure is crystallized evidently [Figs. 3.4 (d) & (e)]. The reason is presumably due to the underneath crystallized HfO_2 which helps the crystallization of Al_2O_3 in some specific direction. Combining the TEM pictures and XRD data [Fig. 3.5] , the crystalline nature of HfO_2 can be easily proofed. In the XRD data, we can find out that the samples deposited at a lower deposition temperature exhibit more crystallization textures. According to the results we discussed in Chapter 2, samples deposited at a lower temperature could contain more trapping sites. For nonvolatile memory application, this phenomenon can help

achieve larger memory window.

3-4 Analysis of Nonvolatile Memory Capacitors

3-4.1 Measurement Setup

The capacitance-voltage (C-V) characteristics were evaluated by an automated measurement setup constructed by Agilent 4284A precision semiconductor parameter analyzer, an Aglient TM 5250A switch, a pulse generator Agilent-81110A, and the Interactive Characterization Software (ICS). During all measurements, the temperature was controlled at a stable value by a temperature-regulated chuck. For basic C-V measurements, we adopted a parallel equivalent circuit model. The frequency of the measured capacitance was set at 100k Hz. After the measurement of capacitance, the following equation was used to extract the capacitance-equivalent-thickness (CET) of the capacitor:

$$CET = \frac{\varepsilon_0 \varepsilon_{SiO2} A}{C_{acc.}}. \qquad \text{(Eq. 3-1)}$$

On the above equation, A means the area of the measured capacitor, and the value is assumed to be 1.52×10^{-3} cm^2 here. $C_{acc.}$ represents the accumulation capacitance of the capacitor. ε_0 and ε_{SiO2} indicate the permittivity of vacuum and silicon dioxide, respectively.

3-4.2 Basic Capacitance-Voltage Analysis

Fig. 3.6 depicts the C-V curves of all devices. The measurements were conducted from inversion to accumulation conditions. The accumulation capacitance and extracted CET are shown in Table 3.2. First, the MANOS device exhibits higher

capacitance than MONOS owing to the higher permittivity of Al_2O_3. The permittivity of Al_2O_3 is nearly 8 based on the result presented in Chapter 2. MAHOS devices exhibit higher capacitance than other two structures. This comes from the contribution of HfO_2 whose permittivity is nearly 16. We can verify the measured CET by the following equation:.

$$CET = \varepsilon_{SiO_2}(\frac{t_{TO}}{\varepsilon_{TO}} + \frac{t_{TL}}{\varepsilon_{TL}} + \frac{t_{BO}}{\varepsilon_{BO}}) \, . \qquad \text{(Eq. 3-2)}$$

The calculated CET values are shown in Table 3.2, and the results are close to the measured ones. Looking at the plots in Fig. 3.5 carefully, small differences in C_{acc} can be found among the MAHOS-A ~ D samples. These differences can be an indication that the deposition temperature of ALD chamber would more or less influence the film quality of HfO_2 [3-2]. Another important thing that should be noted is the flat-band voltage differences among all samples. A former study on hafnium oxide has shown that the oxygen vacancy defects could present in HfO_2 [3-3]. The flat-band voltage shift is mainly caused by the positive fixed oxide charge (Q_{ot}) which is related to the oxygen vacancies formed during the process. The quantities of oxygen vacancy rise when the deposition temperature decreases.

3-4.3 Nonvolatile Memory Characteristics

In this section, two kinds of memory characteristics are evaluated with planar MOS capacitors. The first one is the hysteresis effect. We use a wide round-trip sweeping voltage range to estimate the trapping efficiency of the capacitors. The results are shown in Fig. 3.7 and Table 3.3. Conventional O/N/O stack depicts the smallest window. Although the two nitride-based devices have the same trapping layer,

there's an obvious difference in the memory window. The main reason is postulated to be due to the excessive charge trapping sites presenting in the Al_2O_3 or Al_2O_3/Si_3N_4 interface [3-4]. The MAHOS devices reveal excellent trapping efficiency as we expect. MAHOS-A whose HfO_2 was deposited at the lowest temperature shows the best window (12.16 V), almost 7 times larger than that of the MONOS devices. But it is hard to calculate the trap density precisely with the measurements, since the measured memory window is affected by the programming and erasing effects during the positive and negative sweeping, respectively.

For indentifying the trap density more precisely, we use another way to measure it. First, a fresh C-V curve is measured, than we apply a positive DC bias with long duration (60 sec) to inject electrons into the trapping layer. C-V characterization is then performed again to check the resultant C-V shift. The results are shown in Fig. 3.9. Just like the band diagrams shown in Fig. 3.8, electrons tunnel through the tunneling oxide to the trapping layer as a high positive gate voltage is applied. Owing to their different film composition, the electric field distribution inside each device is different. MAHOS devices have the strongest electric field in the tunneling oxide which enhances tunnel mechanism even as the applied gate voltage is the same as that on other types of samples. After the application of a high bias for a sufficiently long time, negative charges are stored in the trapping layer and the measured C-V curve shifts positively. By fitting the measured data with the following equation, the trapped charge density can be calculated:

$$N_{charge} = \Delta V_{FB} \times C_{total} .$$ (Eq. 3-3)

The measured data and extracted charge density are shown in Table 3.4. The time duration with the applied high bias is decided after a number of testing measurements are done. As a longer time is taken, the flat-band voltage shift is not significant. The

extracted data clearly verify that excess charges can be trapped when the Al_2O_3 is used as the bock oxide. The adoption of HfO_2 can increase the memory window dramatically. Another phenomenon that should be pointed out is that a higher charge density can be achieved with the HfO_2 deposited at a lower temperature. The maximum charge density is roughly 1.5×10^{13} (cm^{-2}), about 7 times larger than the density of the MONOS samples.

3-5 Characterization of TAHOS NW-TFTs

3-5.1 Transfer Characteristics

Fig. 3.10 depicts the transfer characteristics of all NW devices with TiN gate. TiN gate is used for suppression of gate injection during erase operation because of the higher work function [3-5]. All measured devices in this figure have a nominal channel length of 0.4 μm and the EOT can be estimated by data presented in former section. The extracted subthreshold swing (S.S.) of TAHOS device is 168 (mV/dec), which is better than the extracted S.S. values of the other two devices of about 200 mV/dec. The major improvement comes from the smaller EOT in the TAHOS devices which has been investigated in former sections. For the TANOS device, the threshold voltage is larger than that of the TONOS counterpart, which can be explained by the inherently negative fixed charges in the Al_2O_3 [3-6]. In contrast, the TAHOS devices depict the lowest threshold voltage. Although there are still negative charges in the Al_2O_3, the large amount of fixed positive charges in HfO_2 can shift the threshold voltage negatively. The smallest EOT of the TAHOS devices also contribute to the the smallest threshold voltage, too.

3-5.2　Program/Erase Operation Analyses

The basic mechanisms of the program and erase are related to the carriers transport through tunnel oxide. In early years, several carrier transport mechanisms such as channel hot electron injection (CHEI) [3-7], Fowler-Nordheim (F-N) tunneling [3-8], direct tunneling (DT) [3-9], and band-to-band tunneling (BTBT) [3-10] have been developed for SONOS operation. Since the channel of our devices is formed by poly-Si, grain boundaries may scatter the electrons when transporting in the channel. Therefore, these electrons are difficult to gain sufficient energy to become hot. As a result, CHEI is not a suitable method for programming operation in our devices. In this study, we therefore employ the F-N tunneling as the method of P/E operations in the poly-Si NW MONOS devices. In programming operation, both source and drain are grounded while a positive voltage is applied to the gate to induce a large electric field across the gate dielectric. Electrons in the channel can tunnel through the thin tunneling oxide and be captured by the traps in the nitride or hafnium oxide layer. Under erasing operation, both source and drain are grounded and a negative voltage is applied to the gate. High electric field causes holes to inject into nitride or the trapped electrons to de-trap from the trapping layer.

In this study, we keep each layer (i.e., blocking oxide, trapping layer, tunneling oxide) in all splits with the same physical thickness rather than the same EOT, since the objective is to study the feasibility of high-κ metal gate technology with GAA nanowire device architecture for nonvolatile memory application. The purpose of growing equal physical thickness of each layer is to enhance the electric field in the tunneling oxide and reduce the electric field in the blocking oxide in the nanowire TAHOS devices, as a consequence of using high dielectric constant materials. Under P/E operation, F-N tunneling is employed as mentioned before. For programming, the

fresh transfer curve will be measured first and the programmed transfer curve will be measured subsequently after a programming pulse is applied. The P/E characteristics of TONOS device are taken as examples, as shown in Fig. 3.11. The threshold voltage is extracted by constant current method at a magnitude of 1 nA. Fig. 3.11 (a) depicts the programming results, a 2.1 V memory window can be achieved after a 13 V programming pulse for 100 μs. For the erase operation, we start by programming the device with about 2.5 V shift in V_{th} first, then use a negative gate bias pulse to erase the devices. Fig. 3.11 (b) depicts an example of erasing a TONOS device, the memory window is about 1.5 V after applying a -11 V/1 ms pulse. The P/E characteristics of the three types of devices are shown in Figs. 3.12, 3.13, and 3.14, respectively. The TAHOS device is the one with its HfO_2 grown at 250^oC. The influence of deposition temperature will be discussed later. Figs. 3.12 (a), 3.13 (a), and 3.14 (a) depict the V_{th} shift versus programming time for different stack of GAA NW devices with gate biases of 9 V, 10 V, 11 V, 12 V, 13 V, 14 V and 15 V, respectively. Figs. 3.12 (b), 3.13 (b), and 3.14 (b) depict the V_{th} shift versus erasing time for different stack of GAA NW devices with gate biases of -9 V, -10 V, -11 V, -12 V, and -13 V, respectively. As shown in the figures, the V_{th} shift increases when prolonging the operation or increasing the gate bias due to the correspondingly larger F-N tunneling currents. If the target V_{th} shift is 1 V, the TONOS device requires a 14 V/100 ns pulse condition to reach the specification. For the TANOS device, the bias could be lowered to 12 V while the time duration remains unchanged to reach the same V_{th} shift. A further enhancement can be achieved by the TAHOS architecture as we predicted. This phenomenon is desirable for the low power operation in future NVM. The key reason is the reduced EOT which is attributed to the use of high-κ materials. As the band diagrams shown in Fig.3.15, the reduced EOT because of the use of high-κ

blocking oxide and trapping layers causes an enhanced electric field strength across the tunneling oxide and a greater program efficiency. Another reason for the enhancement of programming efficiency is the difference in conduction band offset (ΔEc). The ΔEc between SiO_2 and HfO_2 is 1.7eV which is larger than that between SiO_2 and Si_3N_4 (1.1 eV). Since we adopt F-N tunneling as the method of P/E operation, the larger ΔEc between tunneling oxide and trapping layer is more favorable for carrier trapping. The programming speed characteristics for three splits of devices with an identical gate bias of 13 V are shown in Fig. 3.16. A strong enhancement of programming efficiency can be gained by adopting Al_2O_3 as the blocking oxide. Further improvement can be achieved in TAHOS device by the reasons of higher permittivity and trapping sites of HfO_2 trapping layer. Under the erasing operation, the smaller EOT of the high-κ layer also enhances the electric field across the tunneling oxide, as can be seen from the band diagrams shown in Figs. 3.17 (a) ~ (c). The erasing speed characteristics for the three types of devices with an identical gate bias of -11 V are shown in Fig. 3.18. The major erasing mechanism of the TONOS and TANOS devices is the electron detrapping rather than the hole injection from the substrate [3-11]. So the slight improvement by adopting Al_2O_3 as the blocking oxide could be attributed to the higher electric field across the tunneling oxide. One thing should be pointed out is the dramatic enhancement of the TAHOS device. As has been pointed out in the literatures [3-12], the charges are stored close to the Si_3N_4/Al_2O_3 interface for the TANOS devices, so the P/E operation is strongly related to the interface properties between trapping layer and blocking oxide. In TAHOS devices, the Al_2O_3 deposited on the HfO_2 tends to be crystallized after annealing, as has been indicated in Fig. 3.4(d), while the interface is also rougher than the Si_3N_4 /Al_2O_3 case. By this view point, the excessive charges can be trapped at the

HfO$_2$/Al$_2$O$_3$ surface, so a larger memory window can be achieved.

In this study, TAHOS-NW devices with varying ALD-HfO$_2$ deposition temperature were also fabricated. The deposition temperatures were 100°C, 150°C, 200°C, and 250°C. With the analysis made in the previous section, the trap density only differs slightly among the deposited thin films. The programming and erasing characteristics are shown in Figs. 3.19(a) and (b), respectively. The differences in P/E efficiency among the four devices are very slight. However, we still can observe a rough trend that for the TAHOS device with ALD-HfO$_2$ deposited at a higher temperature, the P/E rate would be retarded owing to the reduced trap density inside the film.

3-5.3   Reliability Characteristics

Reliability of the nonvolatile flash memory is a crucial issue for practical application. In this thesis we examine two important topics of reliability, namely, data retention and endurance. Data retention refers to the ability to keep the storage charges in the trapping layer and provide enough memory window so the logic states can be easily distinguished. Generally, a memory window larger than 0.5V after ten years is necessary for commercial products. Fig. 3.20 depicts the migration paths of the trapped charges, including trap-to-band tunneling (path (a)), trap-to-trap tunneling (path (b)), band-to-trap tunneling (path (c)), and thermal excitation (path (d)) [3-13]. The charges can also move from site to site with level inside the bandgap by the Frenkel-Poole emission, especially under the high electric field. The data loss paths mainly occur at the tunneling oxide due to the thinner physical thickness. For faster P/E speed, the tunneling oxide needs to be scaled down, but there's a trade-off between the P/E speed and the data retention. Under this view point, the adoption of

high-κ materials may help, although it is not investigated in this study. As mentioned in previous section, the physical thickness of the gate dielectric of each split of devices is set the same on purpose for comparison.

Fig. 3.21 depicts the retention characteristics of the fabricated devices. The fresh memory window is all set at a 2-V window. The two nitride-based devices have a comparable predicted memory window after 10-years retention, while the TAHOS device has poorer retention performance. The possible reason for the poorer retention of the TAHOS device is the excessive charges trapped at the shallower traps at the HfO_2/Al_2O_3 interface can easily tunnel through Al_2O_3 by trap-to-band tunneling. By the abovementioned TEM image, the interface of HfO_2/Al_2O_3 is a little rough, and the crystalline nature of Al_2O_3 also provides trap sites for leaking out of the stored charges. So the electron can migrate to the shallower trap and tunnel through blocking oxide by trap-assisted tunneling.

Endurance is another important characteristic in NVM applications. Ideally, the program and erase states can stay unchanged after the P/E cycles. Since high voltage is applied during each program/erase operation, the energetic carriers would degrade the tunneling oxide and generate additional oxide and interface traps, resulting in the degeneration of the device performance. These traps can also become the charge loss paths. Fortunately, today the endurance requirement is relaxed from 10^6 P/E cycles for 128MB density to 10^4 P/E cycles for 2GB density [3-14]. The endurance characteristics of the TONOS and TAHOS devices are shown in Fig. 3.22. The transfer curves of the two devices recorded at the first and 100th cycles are also provided in Figs. 3.23 (a) and (b), respectively. We can find out that the S.S. of both devices is gravely degraded after the P/E cycles. This is due to the interface state generation during the P/E stress. As the TEM images shown in Fig. 3.4, the NW is

rectangular in shape, so the electric field distribution is non-uniform around the NW. The electric field is dramatically larger at the corner of NW. This can cause a large amount of interface state generation wherein and increase the S.S. Another phenomenon that should be pointed out is the trend of the window closure found in the TAHOS device, but not in the TONOS devices. The upward shift of the erase state in the TAHOS device can be explained by the accumulation of electrons in deep traps which cannot be easily removed, resulting in an increase in V_{th}.

3-6 Summary

In this chapter, the applications of high-κ materials, such as HfO_2 and Al_2O_3, to the SONOS-type NVM have been investigated. We studied their electrical properties through simple MOS capacitor and GAA-NW structures. The trap sites in HfO_2 are higher than those in Si_3N_4. The adoption of high-κ layers can also help enhance the P/E efficiency owing to the EOT reduction. Therefore, a lower operation voltage can be achieved to reduce the power consumption of commercial products. We also assessed the reliability properties such as retention and endurance characteristics. It is shown that the replacement of nitride with HfO_2 as a storage layer would degrade the reliability performance. Nonetheless, such an issue should be resolvable if the physical thickness of the high-κ materials is further optimized.

Tables

Table 3.1. Film composition of different splits of the MOS capacitors.

	Block Oxide	Trapping Layer	Tunnel Oxide
MONOS	SiO_2 – 12 nm	Si_3N_4 – 7 nm	SiO_2 – 3 nm
MANOS	Al_2O_3 – 12 nm	Si_3N_4 – 7 nm	SiO_2 – 3 nm
MAHOS-A	Al_2O_3 – 12 nm	$HfO_2(100^oC)$ – 7 nm	SiO_2 – 3 nm
MAHOS-B	Al_2O_3 – 12 nm	$HfO_2(150^oC)$ – 7 nm	SiO_2 – 3 nm
MAHOS-C	Al_2O_3 – 12 nm	$HfO_2(200^oC)$ – 7 nm	SiO_2 – 3 nm
MAHOS-D	Al_2O_3 – 12 nm	$HfO_2(250^oC)$ – 7 nm	SiO_2 – 3 nm

Table 3.2. Measured accumulation capacitance, CET, and estimated CET.

	C_{acc}	CET	Estimated CET
MONOS	3.14E-10 F	16.7 nm	17.9 nm
MANOS	3.93E-10 F	13.3 nm	13.75 nm
MAHOS-A	4.42E-10 F	11.9 nm	11.55 nm
MAHOS-B	4.58E-10 F	11.5 nm	11.55 nm
MAHOS-C	4.69E-10 F	11.2 nm	11.55 nm
MAHOS-D	4.79E-10 F	11.0 nm	11.55 nm

Table 3.3. Hysteresis window of the MOS capacitors with different sweeping voltage ranges.

	±10 V Hysteresis	±15 V Hysteresis
MONOS	1.79 V	1.65 V
MANOS	0.33 V	2.63 V
MAHOS-A	1.92 V	12.16 V
MAHOS-B	2.37 V	11.85 V
MAHOS-C	2.61 V	11.06 V
MAHOS-D	2.50 V	10.46 V

Table 3.4.　Memory window and the extracted charge density from the results shown in Fig. 3.7.

	Window	N_{charge}
MONOS	1.8 V	2.32E+12 cm^{-2}
MANOS	5.3 V	8.56E+12 cm^{-2}
MAHOS-A	8.2 V	1.49E+13 cm^{-2}
MAHOS-B	7.6 V	1.43E+13 cm^{-2}
MAHOS-C	7.2 V	1.39E+13 cm^{-2}
MAHOS-D	6.1 V	1.20E+13 cm^{-2}

Chapter 4

Conclusion and Future Work

4-1   Conclusion

This thesis focuses on the study of properties of high-κ materials and their applications to nonvolatile memory devices with poly-Si NW channels. We utilize the fabrication of top-down NW method without involving advanced lithography technology.   In former studies [4-1, 4-2], NW SONOS devices with GAA configuration have been demonstrated to exhibit greatly enhanced P/E efficiency. In this study, we have investigated the properties of high-κ materials such as Al_2O_3 and HfO_2. These materials are further implemented in the NW SONOS-like NVM to enhance the P/E efficiency. For gate dielectric stacks with same physical thickness, the results show that the utilization of the high-κ materials can improve the drive current and S.S. of the devices because of lower EOT. The experimental results also show that the adoption of Al_2O_3 as the blocking oxide can enhance the electric field across the tunneling oxide and thus fasten the P/E speed. Furthermore, the adoption of HfO_2 as the trapping layer can also enhance the P/E efficiency and widen the memory window. The use of high-work-function metal gates suppresses gate electron injection from the gate during erasing. By these results, the NW-TAHOS device can operate at lower voltage and therefore with reduced power consumption. For retention test, the

NW-TAHOS device shows poorer but acceptable memory window at the 10 years prediction. For the endurance test, all devices depict degraded S.S. after some P/E cycles. This is attributed to the rectangular form of the NW. The electric field is stronger at the corners during P/E operation, causing a large amount of interface states generation wherein. For this reason, the degradation in S.S. is not surprising.

4-2   Suggested Future Work

This study has demonstrated the feasibility of utilizing high-κ materials for next generation NVM as well as for 3-D stack NVM technology. But there are still some issues that should be solved. First, some former reports have shown that the thickness of each layer in the gate dielectric stack can greatly affect the characteristics of NVM [4-3, 4-4] and should be optimized to reach faster P/E speed and larger memory window. Furthermore, the annealing temperature and time should be optimized, too. Second, to further enhance the device performance, the NW should be shrunk to smaller size. If achievable, a NW having a circular-shaped cross-section is preferred. Such a NW possesses highly uniform electric field on the channel surface and thus suppresses the corner effect. Third, a device called Junctionless SONOS has attracted much attention recently [4-5]. By utilizing this technology and incorporating high-κ materials, the P/E speed can be further enhanced. Finally, the use of band-engineered tunneling oxide and blocking oxide can help improve the charge retention [4-6]. Modulation of the film composition during deposition is essential for realization of the goal.

References

Chapter 1

[1-1]   D. Hisamoto, W. C. Lee, J. Kedzierski, H. Takeuchi, K. Asano, C. Kuo, E. Anderson, T. J. King, J. Bokor, and C. Hu, "FinFET-a self-aligned double-gate MOSFET scalable to 20 nm," *IEEE Trans. Electron Devices*, vol. 47, no. 12, pp. 2320-2325, Dec. 2002.

[1-2]   B. Doyle, S. Datta, M. Doczy, S. Hareland, B. Jin, J. Kavalieros, T. Linton, A. Murthy, R. Rios, and R. Chau, "High performance fully-depleted tri-gate CMOS transistors," *IEEE Electron Device Lett.*, vol. 24, no. 4, pp. 263-265, Apr. 2003.

[1-3]   F. L. Yang, H. Y. Chen, F. C. Chen, C. C. Huang, C. Y. Chang, H. K. Chiu, C. C. Lee, C. C. Chen, H. T. Huang, C. J. Chen, H. J. Tao, Y. C. Yeo, and C. Hu, "25 nm CMOS omega FETs," *IEDM Tech. Dig.*, pp.255-258, 2002.

[1-4]   J. P. Colinge, M. H. Gao, A. R. Rodriguez, H. Maes, and C. Claeys, "Silicon-on-insulator gate-all-around device," *IEDM Tech. Dig.*, pp.595-598, 1990.

[1-5]   T. Poiroux, M. Vinet, O. Faynot, J. Widiez, J. Lolivier, T. Ernst, B. Previtali and S. Deleonibus. "Multiple gate devices: advantages and challenges," *Microelectronic Engineering,* vol.80, pp 378-385, 2005.

[1-6]   S. Monfray, T. Skotniki, Y. Morand, S. Descombes, P. Coronel, P. Mazoyer, S. Harrison, P. Ribot, A. Talbot, D. Dutartre, M. Haond, R. Palla, Y. Le Friec, F. Leverd, M. E. Nier, C. Vizioz, and D. Louis, "50 nm-gate all around (GAA)–silicon on nothing (SON)–devices: A simple way to co-integration of GAA transistors with bulk MOSFET process," *VLSI Symp. Tech. Dig.*, pp. 108-109, 2002.

[1-7]   J. T. Park and J. P. Colinge, "Multiple-gate SOI MOSFETs: Device design guidelines," *IEEE Trans. Electron Devices*, vol. 49, no. 12, pp. 2222-2229, 2002.

[1-8]   N. Singh, A. Agarwal, L. K. Bera, T. Y. Liow, R. Yang, S. C. Rustagi, C. H. Tung, R. Kumar, G. Q. Lo, N. Balasubramanian, and D. L. Kwon, "High-performance fully depleted silicon nanowire (diameter 5 nm) gate-all-around CMOS devices," *IEEE Electron Device Lett.*, vol. 27, no. 5, pp. 383-386, 2006.

[1-9]   Y. Cui, Z. Zhong, D. Wang, W. U. Wang, and C. M. Lieber, "High performance silicon nanowire field effect transistors," *Nano Lett.*, vol. 3, no. 2, pp.149-152, 2003.

[1-10] F. Patolsky and C. M. Lieber, "Nanowire nanosensors," *Materials today*, vol.

8, pp. 20-28, 2005.

[1-11] Y. Cui, Q. Wei, H. Park, and C. M. Lieber, "Highly sensitive and selective detection of biological and chemical species," *Science.*, vol. 293, no. 17, pp.1289-1292, 2001.

[1-12] Q. Li, X. X. Zhu, H. D. Xiong, S. M. Koo, D. E. Ioannou, J. J. Kopanski, J. S. Suehle and C. A. Richter, "Silicon nanowire on oxide/nitride/oxide for memory application," *Nanotechnology*, vol. 18, 2007.

[1-13] M. H. Lankhorst, B. W. Ketelaars, and R. Wolters, "Low-cost and nanoscale non-volatile memory concept for future silicon chips," *Nature*, vol. 236, no. 4, pp. 36–49, 2005.

[1-14] Y. Shin, J. Choi, C. Kang, C. Lee, K. T. Park, J. S. Lee, J. Sel, V. Kim, B. Choi, J. Sim, D. Kim, H. J. Cho, and K. Kim, "A novel NAND-type MONOS memory using 63nm process technology for multi-gigabit flash EEPROMs," *IEDM Tech. Dig.*, pp. 327-330, 2005.

[1-15] C. Y. Lu, K. Y. Hsieh and R. Liu, "Future challenges of flash memory technologies," *Microelectronic Engineering*, vol. 86, no. 3, pp. 283-286, 2009.

[1-16] J. D. Lee, S. H. Hur, and J. D. Choi, "Effects of floating-gate interference on NAND flash memory cell operation," *IEEE Electron Device Lett.*, vol. 23, no. 5, pp. 264-266, 2002.

[1-17] Z. J. Tang, Z. G. Liu and X. H. Zhu, "Progress of high-κ dielectrics applicable to SONOS-type nonvolatile semiconductor Memories," *Transactions on Electrical and Electronics Materials*, vol. 11, no. 4, pp. 155-165, 2010.

[1-18] M. H. White, D. A. Adams, and J. Bu, "On the go with SONOS," *IEEE Circuits and Devices Magazine,* vol. 16, no. 4, pp. 22-31, 2000.

[1-19] S. C. Chen, T. C. Chang, P. T. Liu, Y. C. Wu, P. H. Yeh, C. F. Weng, S. M. Sze, C. Y. Chang and C. H. Lien, "Nonvolatile polycrystalline silicon thin-film-transistor memory with oxide/nitride/oxide stack gate dielectrics and nanowire channels," *Appl. Phys. Lett.,* vol. 90, p.122111, 2007.

[1-20] J. Fu, N. Singh, C. Zhu, G. Q. Lo, and D. L. Kwong, "Integration of high-κ dielectrics and metal gate on gate-all-around Si-nanowire-based architecture for high-speed nonvolatile charge-trapping memory," *IEEE Electron Device Lett.*, vol. 30, no. 6, pp. 662-664, 2009.

[1-21] Y. H. Hsiao, H. T. Lue, M. Y. Lee, S. C. Huang, T. Y. Chou, S. Y. Wang, K. Y. Hsieh, R. Liu, and C. Y. Lu, "A study of SONOS charge loss mechanism after hot-hole stressing using trap-layer engineering and electrical re-fill methods," *International Reliability Phys. Symp.*, pp. 695-696, 2008.

[1-22] V. A. Gritsenko, K. A. Nasyrov, Y. N. Novikov, A. L. Aseev, S. Y. Yoon, J. W. Lee, E. H. Lee, and C. W. Kim, "A new low voltage fast SONOS

memory with high-κ dielectric," *Solid-State Electronics*, vol. 47, no. 10, pp. 1651-1656, 2003.

[1-23] C. H. Lee, K. I. Choi, M. K. Cho, Y. H. Song, K. C. Park and K. Kim, "A novel SONOS structure of $SiO_2/SiN/Al_2O_3$ with TaN metal gate for multi-giga bit flash memories," *IEDM Tech. Dig.,* pp.613-616, 2003.

[1-24] C. H. Lee, S. H. Hur, Y. C. Shin, J. H. Choi, D. G. Park, and K. Kim, "Charge-trapping device structure of $SiO_2/SiN/high-κ$ dielectric Al_2O_3 for high-density flash memory," *Appl. Phys. Lett.,* vol. 86, no.15, p.152908 2005.

[1-25] T. M. Pan, and W. W. Yeh, "A high-κ Y_2O_3 charge trapping layer for nonvolatile memory application," *Appl. Phys. Lett.,* vol. 92, no.17, p.173506 2008.

[1-26] X. Wang, and D. L. Kwong, "A novel high-κ SONOS memory using $TaN/Al_2O_3/Ta_2O_5/HfO_2/Si$ structure for fast speed and long retention operation," *IEEE Trans. Electron Devices*, vol. 53, no. 1, pp. 78-82, 2006.

[1-27] H. C. You, T. H. Hsu, F. H. Ko, J. W. Huang, W. L. Yang and T. F. Lei, "SONOS-type flash memory using an HfO_2 as a charge trapping layer deposited by the sol–gel spin-coating method," *IEEE Electron Device Lett.*, vol. 27, no. 8, pp. 653-655, 2006.

[1-28] M. Specht, H. Reisinger, F. Hofmann, T. Schulz, E. Landgraf, R. J. Luyken, W. Rösner, M. Grieb, and L. Risch, "Charge trapping memory structures with Al_2O_3 trapping dielectric for high-temperature applications," *Solid-State Electronics*, vol. 49, no. 5, pp. 716-720, 2005.

[1-29] Y. H. Lin, T. Y. Yang, C. H. Chien, and T. F. Lei, "2-Bit lanthanum oxide trapping layer nonvolatile flash memory," *International Conference on Solid-State Devices and materials (SSDM)*, pp. 558-559, 2006.

[1-30] M. S. Joo, S. R. Lee, H. Yang, K. Hong, S. A. Jang, J. Koo, J. Kim, S. Shin, M. Kim, S. Pyi, N. Kwak, and J. W. Kim, "The incorporation effect of thin Al_2O_3 layers on ZrO_2-Al_2O_3 nanolaminates in the composite oxide-high-κ-oxide stack for the floating gate flash memory devices," *International Conference on Solid-State Devices and materials (SSDM)*, pp. 983-984, 2006.

[1-31] Y. Q. Wang, G. Samudra, D. Y. Gao, C. Shen, W. S. Hwang, G. Zhang, Y. C. Yeo, and W. J. Yoo, "Fast erasing and highly reliable MONOS type memory with HfO_2 high-κ trapping layer and Si_3N_4/SiO_2 tunneling stack," *IEDM Tech. Dig.*, pp. 971-974, 2006.

[1-32] J. Fu, Singh, B. Yang, C. X. Zhu, G. Q. Lo, and D. L. Kwong, "Si-nanowire TAHOS ($TaN/Al_2O_3/HfO_2/SiO_2/Si$) nonvolatile memory cell," *Proc. ESSDERC*, pp.138-141, 2008.

[1-33] J. Fu, N. Singh, K. D. Buddharaju, S. H. G. Teo, C. Shen, Y. Jiang, C. X. Zhu,

M. B. Yu, G. Q. Lo, N. Balasubramanian, D. L. Kwong, E. Gnani, and G. Baccarani, "Si-nanowire based gate-all-around nonvolatile SONOS memory cell," *IEEE Electron Device Lett.*, vol. 29, no. 5, pp. 518–521, 2008.

Chapter 2

[2-1] J. Robertson, " Band offsets of wide-band-gap oxides and implications for future electronic devices," *J. Vac. Sci. Technol. B,* vol. 18, pp. 1785-1791, 2000.

[2-2] T. Suntola, M. Ahonen, M. Pessa, and T. Suntola, U.S. Patent 4 058 430, 1977.

[2-3] R. G. Gordon, D. Hausmann, E. Kim, and J. Shepard, "A kinetic model for step coverage by atomic layer deposition in narrow holes or trenches," *Chem. Vap. Deposition*, vol. 9, no. 2, pp. 73-78, 2003.

[2-4] H. J. Fan, M. Knez, R Scholz, K. Nielsch, E. Pippel, D. Hesse, M. Zacharias, and U. Gosele, " Monocrystalline spinel nanotube fabrication based on the Kirkendall effect," *Nat. Mater.*, vol. 5, pp. 627-631, 2006.

[2-5] M. Knez, A. Kadri, C. Wege, U. Gösele, H. Jeske, and K. Nielsch, " Atomic layer deposition on biological macromolecules: metal oxide coating of tobacco mosaic virus and ferritin," *Nano Lett.* , vol. 6, no.6, pp. 1172-1177 2006.

[2-6] Y. Senzaki, S. Park, H. Chatham, L. Bartholomew, and W. Nieveen, "Atomic layer deposition of hafnium oxide and hafnium silicate thin films using liquid precursors and ozone," *J. Vac. Sci. Technol. A*, vol. 22, no.4, pp. 1175-1181 2004.

[2-7] E. H. Nicollian, and J. R. Brews, *MOS (Metal Oxide Semiconductor) Physics and Technology*: John Wiley, 1982.

[2-8] E. H. Nicollian and A. Goetzberger, "The Si-SiO$_2$ interface - electrical properties as determined by the metal-insulator-silicon conductance technique," *Bell System Technical Journal*, vol. 46, no.6, pp. 1055-1133, 1967.

[2-9] W. A. Hill and C. C. Coleman, "A single frequency approximation for interface-state density determination," *Solid State Electron.*, vol. 23, no. 9, pp. 987–993, 1980.

[2-10] X. Zhao and D. Vanderbilt, "First-principles study of structural, vibrational, and lattice dielectric properties of hafnium oxide," *Phys. Rev. B.*, vol. 65, no. 23, p. 233 106, 2002.

[2-11] N. V. Nguyen, A. V. Davydov, D. C. Horowitz, and M. M. Frank, "Sub-bandgap defect states in polycrystalline hafnium oxide and their suppression by admixture of silicon," *Appl. Phys. Lett.*, vol. 87, no. 17, p.192903, 2005.

[2-12] F. Bohra, B. Jiang, and J. M. Zuo, "Textured crystallization of ultrathin hafnium oxide films on silicon substrate," *Appl. Phys. Lett.*, vol. 90, no. 16, p.161917, 2007.

[2-13] J. Aarik, J. Sundqvist, A. Aidla, J. Lu, T. Sajavaara, K. Kukli and A. Hårsta, "Texture development in nanocrystalline hafnium dioxide thin films grown by atomic layer deposition," *Thin Solid Films* vol. 220, no. 1-2 , pp. 105-113, 2002.

[2-14] B. E. Deal, "Standardized terminology for oxide charges associated with thermally oxidized silicon," *IEEE Trans. Electron Devices*, vol. 27, no. 3, pp. 606–608, 1980.

[2-15] G. Bersuker, C. S. Park, J. Barnett, P. S. Lysaght, P. D. Kirsch, C. D. Young, R. Choi, B. H. Lee, B. Foran, K. van Benthem, S. J. Pennycook, P. M. Lenahan, and J. T. Ryan, "The effect of interfacial layer properties on the performance of Hf-based gate stack devices," *J. Appl. Phys.*, vol. 100, no. 9, pp. 094-108, Nov. 2006.

[2-16] P. K. Hurley, K. Cherkaoui, E. O'Connor, M. C. Lemme, H. D. B. Gottlob, M. Schmidt, S. Hall, Y. Lu, O. Buiu, B. Raeissi, J. Piscator, O. Engström, and S. B. Newcomb, "Interface defects in HfO_2, LaSiOx, and Gd_2O_3 high-κ/metal-gate structures on silicon," *J. Electrochem. Soc.*, vol. 155, no. 2, pp. G13–G20, Dec. 2008.

[2-17] H. Holleck, "Material selection for hard coatings," *J. Vac. Sci. Technol. A, Vac. Surf. Films,* vol. 4, pp. 2661–2669, 1986.

[2-18] S. A. Campbell, *The Science and Engineering of Microelectronic Fabrication*, 2nd ed. New York: Oxford, p. 585 , 2001.

[2-19] Z. Zhang, M. Li, and S. A. Campbell, "A Study on charge reduction in HfO_2 gate Stacks," *IEEE Trans. Electron Devices*, vol. 52, no.8, pp. 1839-1844, 2005.

[2-20] K. Kukli, M. Ritala, T. Sajavaara, J. Keinonen and M. Leskelä , "Comparison of hafnium oxide films grown by atomic layer deposition from iodide and chloride precursors," *Thin Solid Films*, vol. 416, no.1-2, pp. 72-79, 2002.

Chapter 3

[3-1] W. C. Chen, H. C. Lin, Y. C. Chang, C. D. Lin, and T. Y. Huang, "*In situ* doped source drain for performance enhancement of double-gated poly-Si nanowire transistors," *IEEE Trans. Electron Devices*, vol. 57, no.7, pp. 1608-1615, Jul. 2010.

[3-2] X. Liu, S. Ramanathan, A. Longdergan, A. Srivastava, E. Lee, T. E. Seidel, J. T. Barton, D. Pang, and R. G. Gordonb, "ALD of hafnium oxide thin films

from tetrakis„(ethylmethylamino)…hafnium and ozone," *J. Electrochem. Soc.*, vol. 152, no. 3, pp. G213–G219, Dec. 2008.

[3-3] K. Tse and J. Robertson, "Defects and their passivation in high-κ gate oxides," *Microelectron. Eng.*, vol. 84, pp. 663–668, 2007.

[3-4] A. Kerber, E. Cartier, R. Degraeve, L. Pantisano, Ph. Roussel, and G. Groeseneken, "Strong correlation between dielectric reliability and charge trapping in SiO$_2$/Al$_2$O$_3$ gate stacks with TiN electrodes," in *Proc. VLSI Technol. Symp.*, pp. 76–77, 2002.

[3-5] M. Lukosius, Ch. Wenger, S. Pasko, H.-J. Mussig, B. Seitzinger, Ch. Lohe, "Atomic vapor deposition of titanium nitride as metal electrodes for gate-last CMOS and MIM devices," *Chem. Vap. Depos.*, vol. 14, pp. 123–128, 2008.

[3-6] G. D.Wilk, R. M.Wallace, and J. M. Anthony, "High-κ gate dielectrics: Current status and materials properties considerations," *J. Appl. Phys.*, vol. 89, pp. 5243–5275, 2001.

[3-7] B. Eitan and D. F. Bentchkowsky, "Hot electron injection into the oxide in n-channel MOS-devices," *IEEE Trans. Electron Devices*, vol. 28, pp. 328-340, 1981.

[3-8] M. Lenzlinger, E. H. Snow, "Fowler-Nordheim tunneling in thermally grown SiO$_2$," *J. Appl. Phys.*, vol. 40, pp. 278-283, 1969.

[3-9] H. Bachhofer, H. Reisinger, E. Bertagnolli, and H. von Philipsborn, "Transient conduction in multidielectric silicon-oxide-nitride-oxide semiconductor structures," *J. Appl. Phys.*, vol. 89, no. 5, pp. 2791-2800, 2001.

[3-10] T. Ohnakado, K. Mitsunaga, M. Nunoshita, H. Onoda, K. Sakakibara, N. Tsuji, N. Ajika, M. Hatanaka, and H. Miyoshi, "Novel electron injection method using band-to-band tunneling induced hot electrons (BBHE) for flash memory with a p-channel cell," *IEDM Tech. Dig.*, Dec. 1995, pp. 279–282.

[3-11] S. Lai, H. Lue, J. Hsieh, M. Yang, Y. Chiou, C. Wu, T. Wu, G. Luo, C. Chien, E. Lai, K. Hsieh, R. Liu, and C. Lu, "Study of the erase mechanism of MANOS (metal/Al$_2$O$_3$/SiN/SiO$_2$/Si) device," *IEEE Electron Device Lett.*, vol. 28, no. 7, pp. 643–645, 2007.

[3-12] L. Vandelli, A. Padovani, and L. Larcher, "Role and compensation of holes and electrons under erase of TANOS memories: Evidences of dipole formation and its impact on reliability," *Proc. IEEE Int. Reliab. Phys. Symp* , pp. 731–737, 2010.

[3-13] Y. Yang and M. H. White, "Charge retention of scaled SONOS nonvolatile memory devices at elevated temperatures," *Solid-State Electron.*, vol. 44, pp. 949–958, 2000.

[3-14] K. Kim and J. Choi, "Future outlook of NAND flash technology for 40nm

node and beyond," *Non-Volatile Semiconductor Memory Workshop*, pp. 9-11, 2006.

Chapter 4

[4-1] H. H. Hsu, T. W. Liu, L. Chan, C. D. Lin, T. Y. Huang, and H. C. Lin, "Fabrication and characterization of multiple-gated poly-Si nanowire thin-film transistors and impacts of multiple-gate structures on device fluctuations," *IEEE Trans. Electron Devices*, vol. 55, no. 11, pp. 3063–3069, 2008.

[4-2] J. Fu, Y. Jiang, N. Singh, C. X. Zhu, G. Q. Lo, and D. L. Kwong, "Polycrystalline Si nanowire SONOS nonvolatile memory cell fabricated on a gate-all-around (GAA) channel architecture," *IEEE Electron Device Lett.*, vol. 30, no. 3, pp. 246–249, 2009.

[4-3] C. H. Lee, S. H. Hur, Y. C. Shin, J. H. Choi, D. G. Park, and K. Kim, "Charge-trapping device structure of SiO_2/Si_3N_4/high-κ dielectric Al_2O_3 for high-density flash memory," *Appl. Phys. Lett.*, vol. 86, p.152908, 2005.

[4-4] S.Maikap, H. Y. Lee, T.Wang, P. Tzeng, C. C.Wang, L. S. Lee, K. C. Liu, J. Yang, and M. Tsai, "Charge trapping characteristics of atomic-layer deposited HfO_2 films with Al_2O_3 as a blocking oxide for high-density non-volatile memory device applications," *Semicond. Sci. Technol.*, vol. 22, no. 8, pp. 884–889, 2007.

[4-5] H. T. Lue, E. K. Lai, Y. H. Hsiao, S. P. Hong, M. T. Wu, F. H. Hsu, N. Z. Lien, S. Y. Wang, L. W. Yang, T. Yang, K. C. Chen, K. Y. Hsieh, R. Liu, and C. Y. Lu, "A novel junction-free BE-SONOS NAND flash," *VLSI Symp. Tech. Dig.*, pp. 140–141, 2008.

[4-6] D. Gilmer, N. Goel, H. Park, C. Park, S. Verma, G. Bersuker, P. Lysaght, H. Tseng, P. Kirsch, K. Saraswat, and R. Jammy, "Engineering the complete MANOS-type NVM stack for best in class retention performance," *IEDM Tech. Dig.*, pp. 439–442, 2009.

Figures
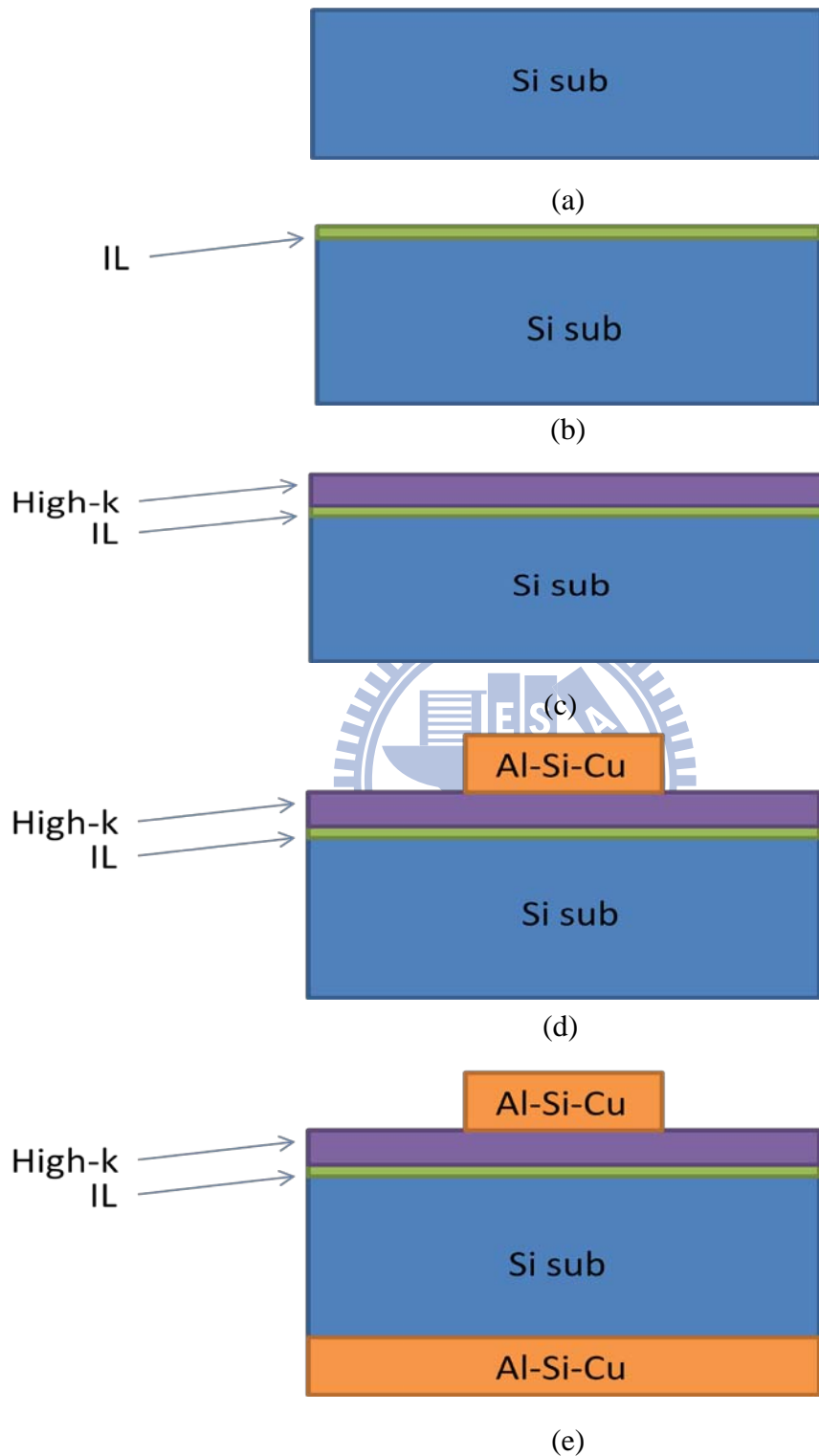
Figure 2.1.   Key fabrication steps of an MOS capacitor. (a) Start with a bare silicon substrate. (b) Formation of an interfacial layer by RTO. (c) Deposition of a high-κ layer by ALD and PDA. (d) Top electrode deposition and patterning. (e) Back electrode deposition.

(a)

(b)
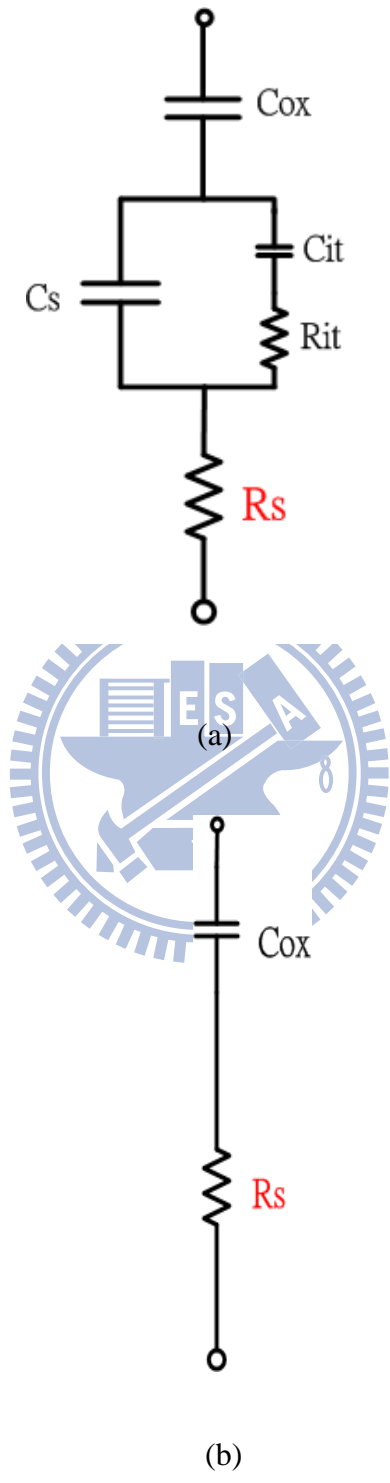
Figure 2.2.   (a) Equivalent circuit of a MOS capacitor including series resistance R_s.

(b) Simplified version of (a).

(a)
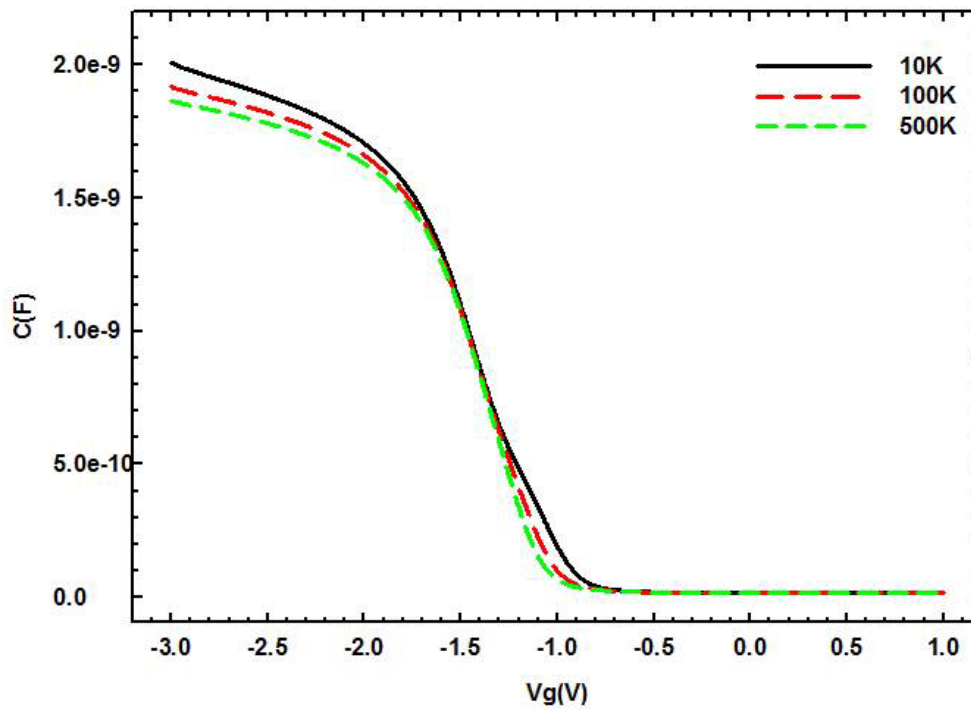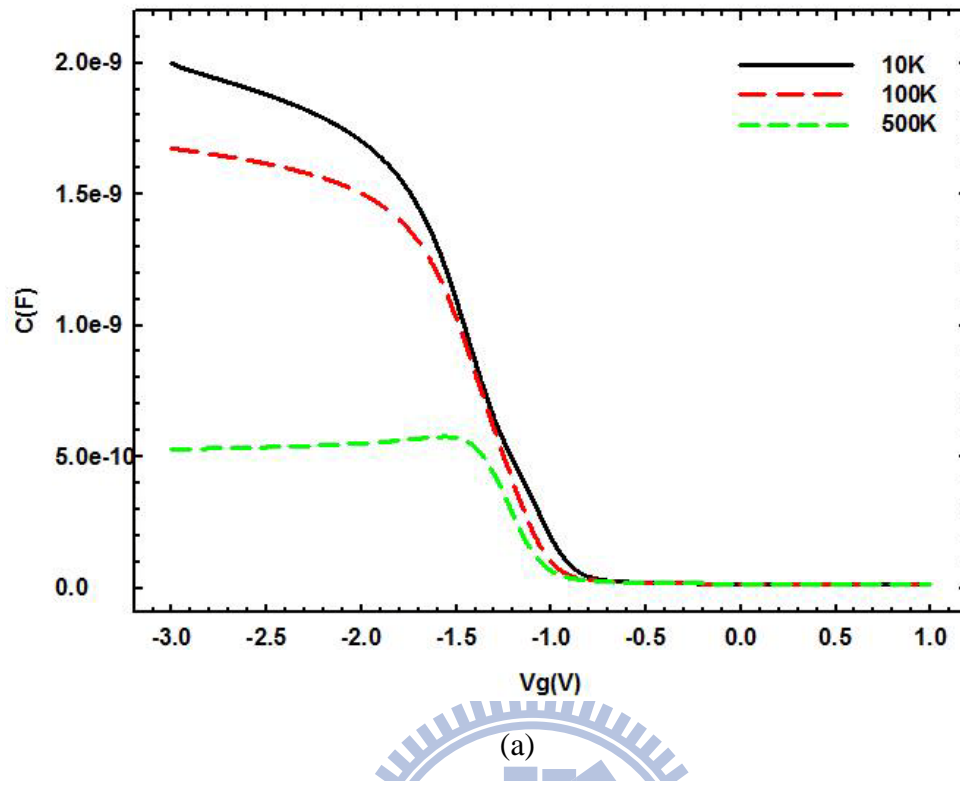
(b)

Figure 2.3.   (a) C-V plots of an MOS capacitor measured at different frequencies. (b) C-V plots of the corrected data.

(c)
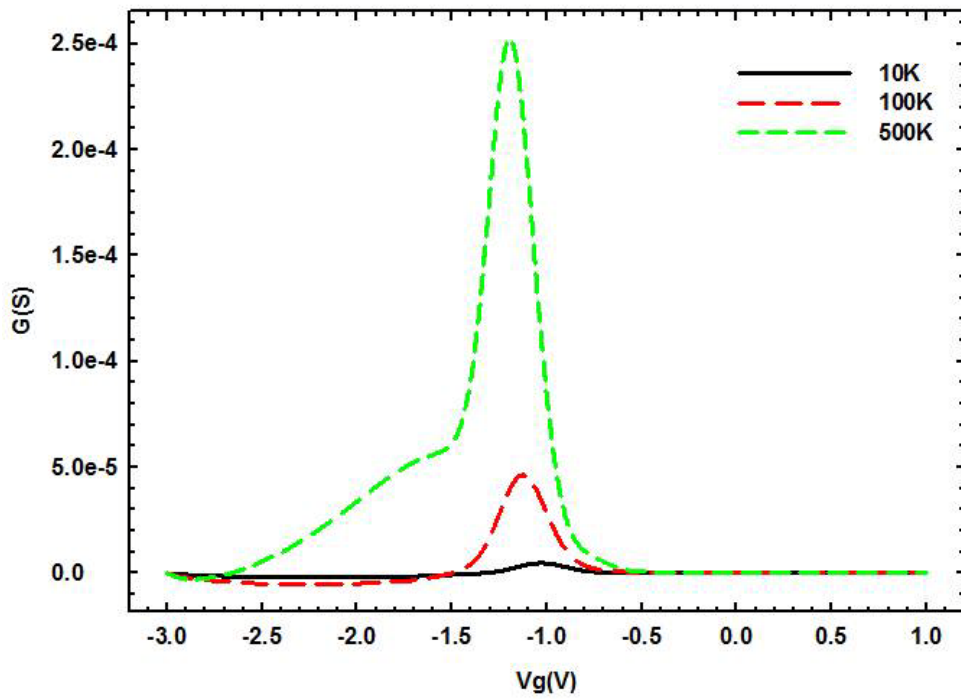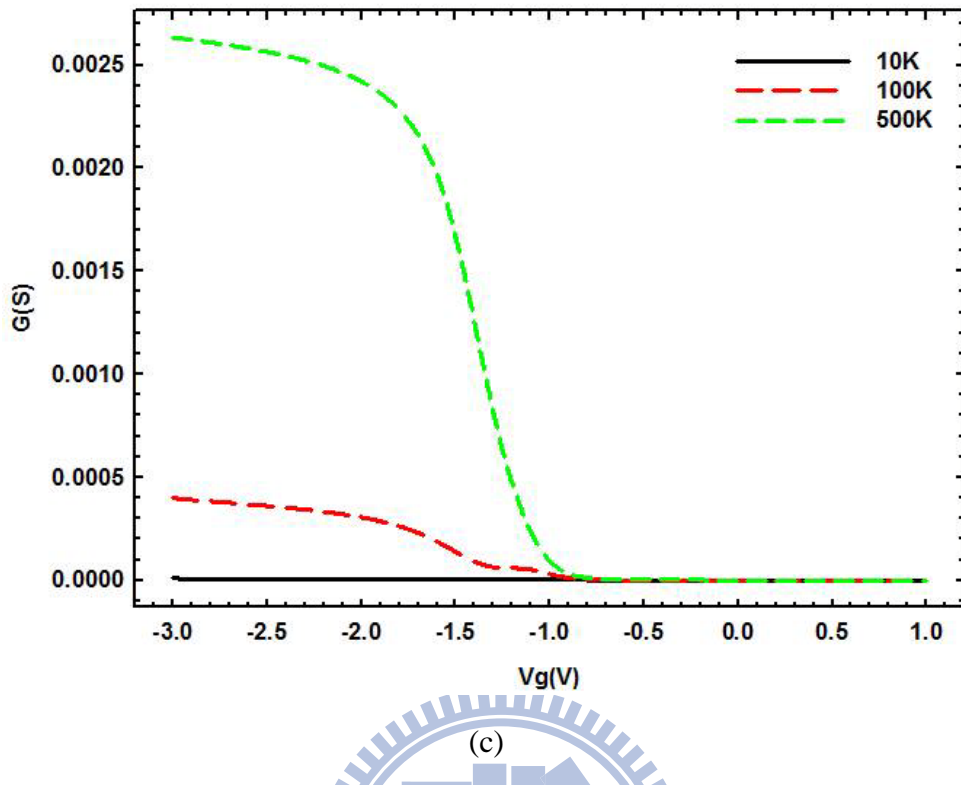
(d)

Figure 2.3. (c) G-V plots of an MOS capacitor measured at different frequencies. (d) G-V plots of the corrected data.
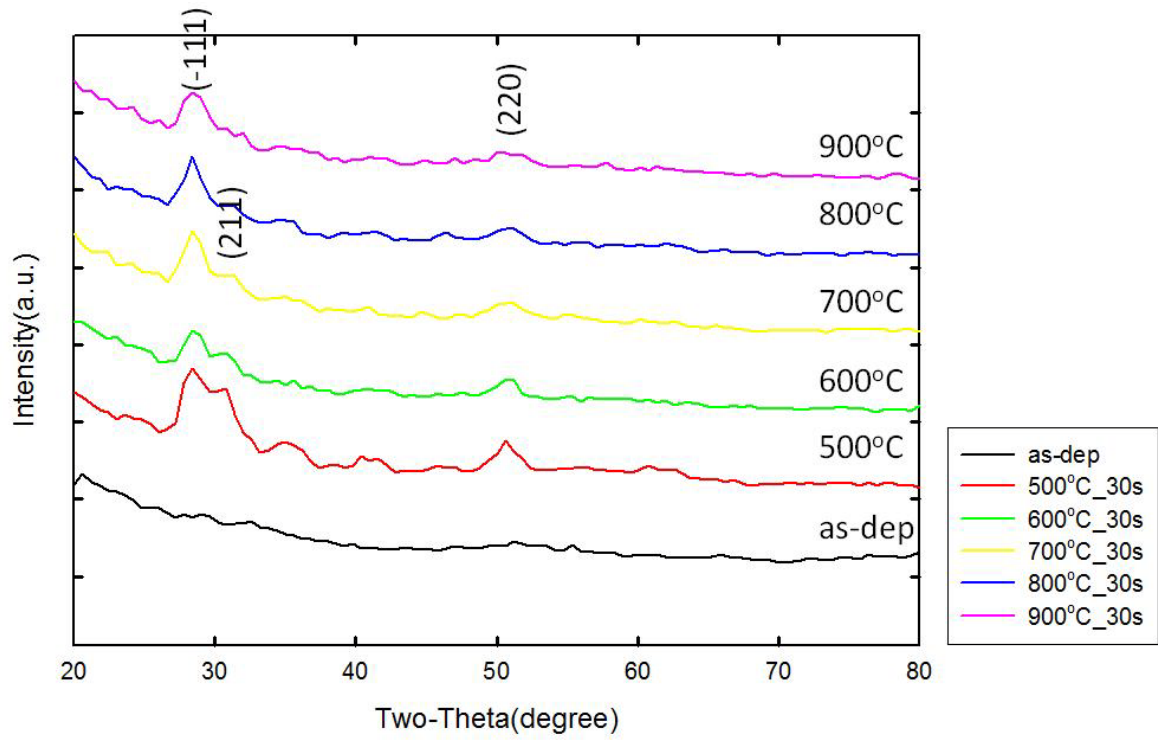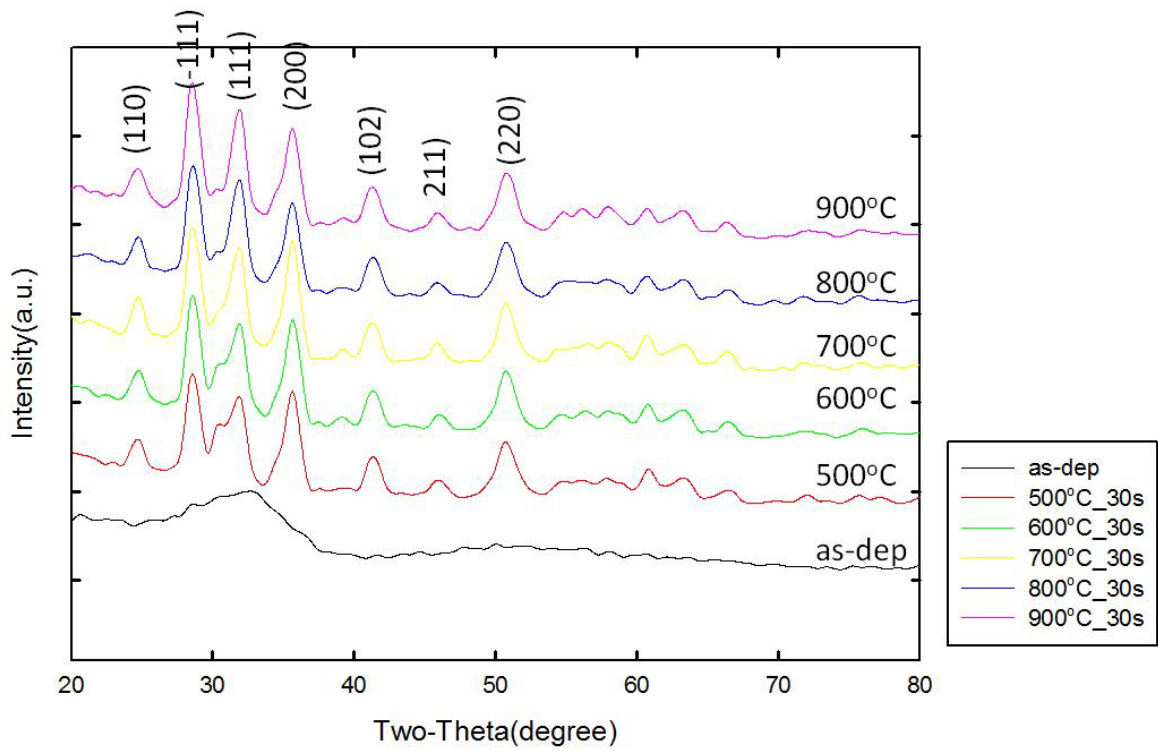
Figure 2.4. XRD data for the HfO$_2$ samples of (a) 5 nm and (b) 10 nm thickness.

(a)
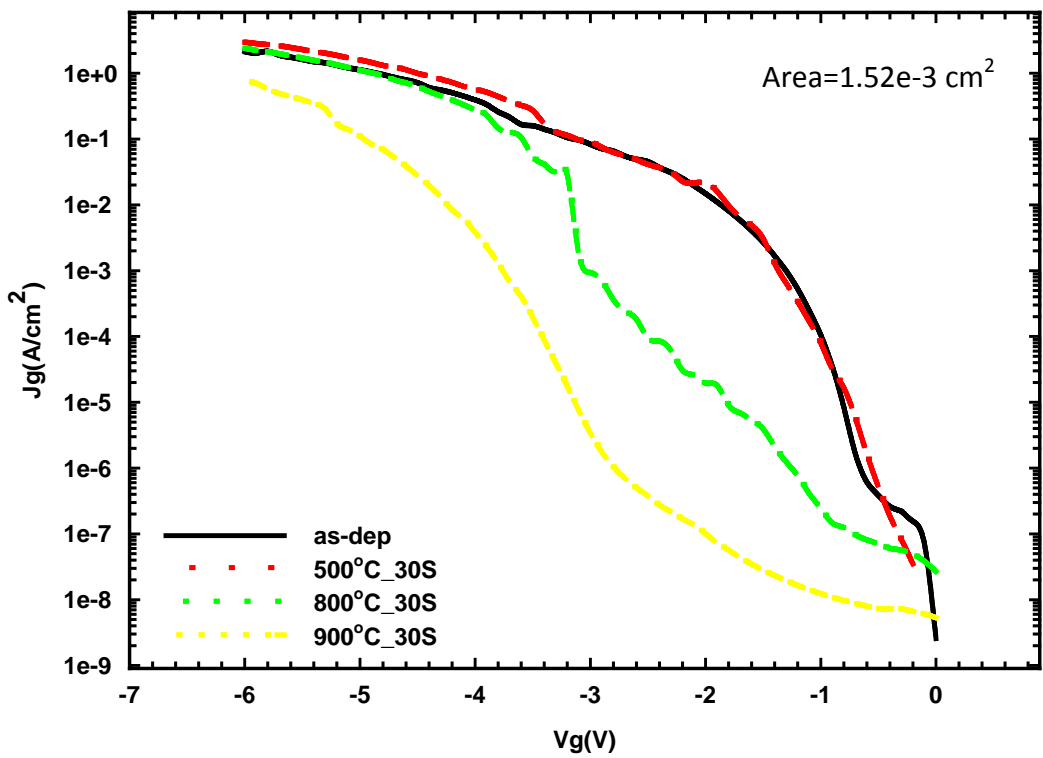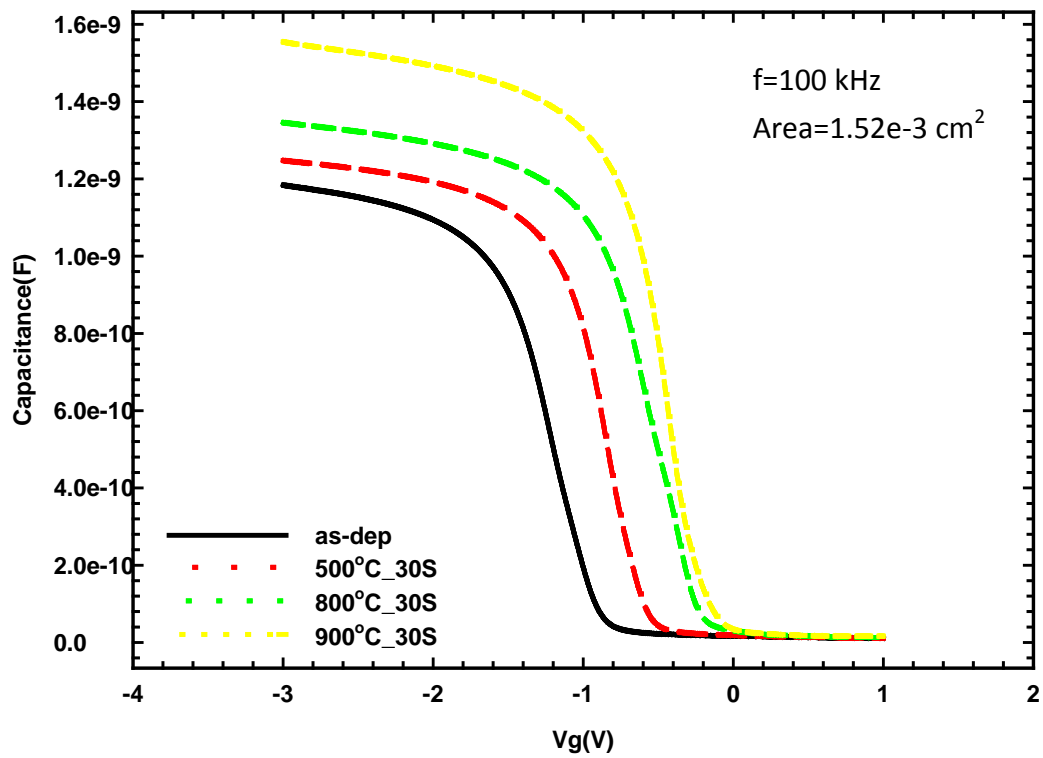
(b)

Figure 2.5. (a) C-V and (b) J-V curves of 5 nm-Al$_2$O$_3$ samples with various PDA conditions.

(a)
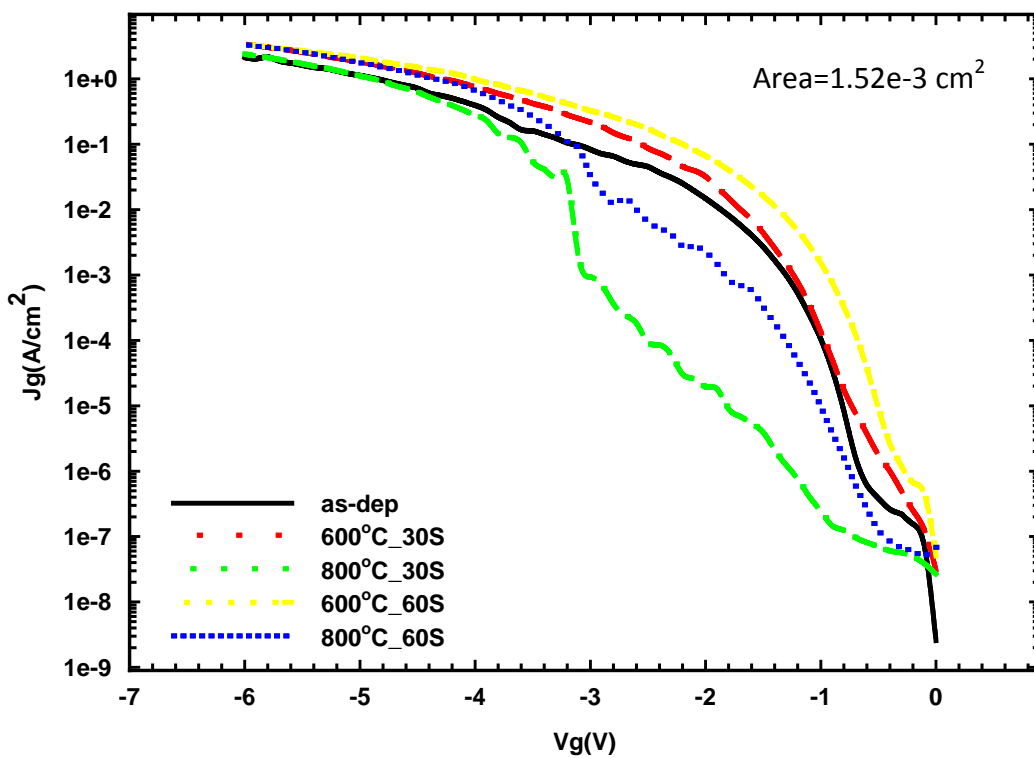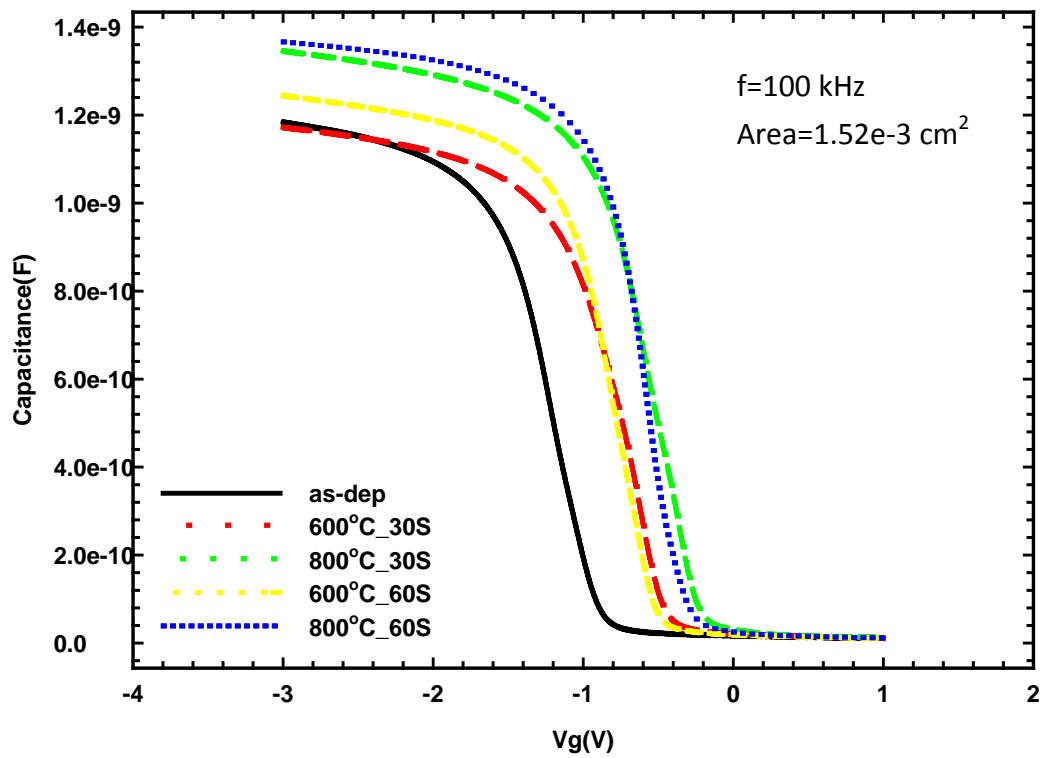
(b)

Figure 2.6.   (a) C-V and (b) J-V curves of 5 nm-Al$_2$O$_3$ samples with various PDA conditions.

(a)
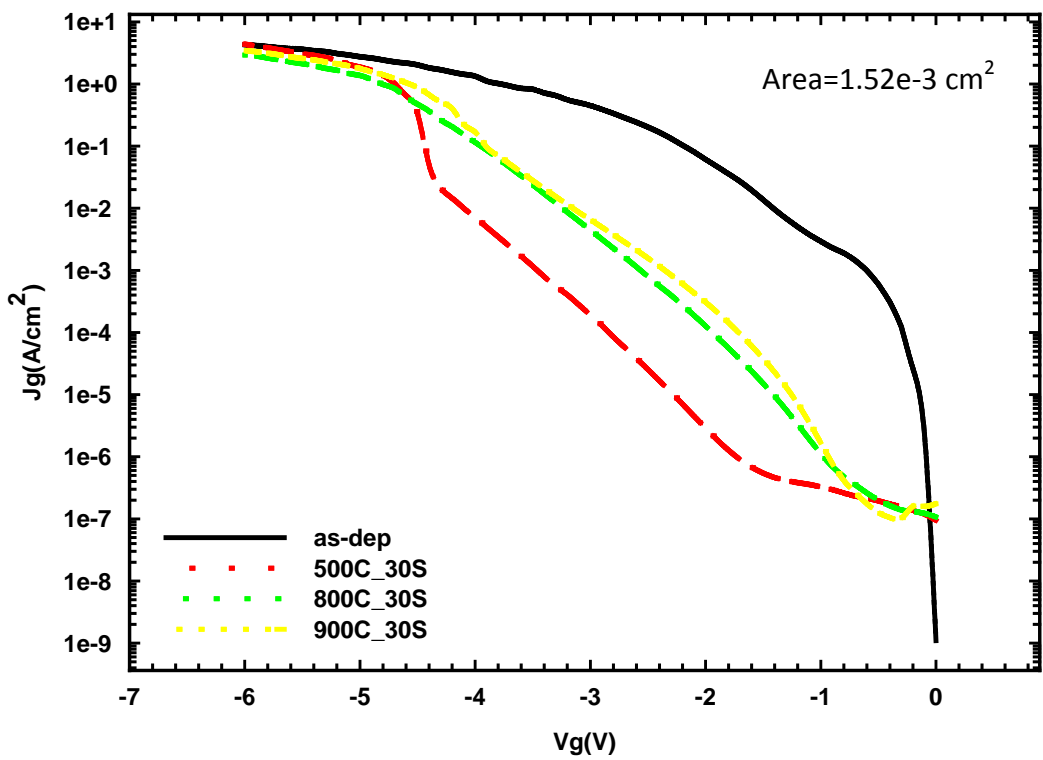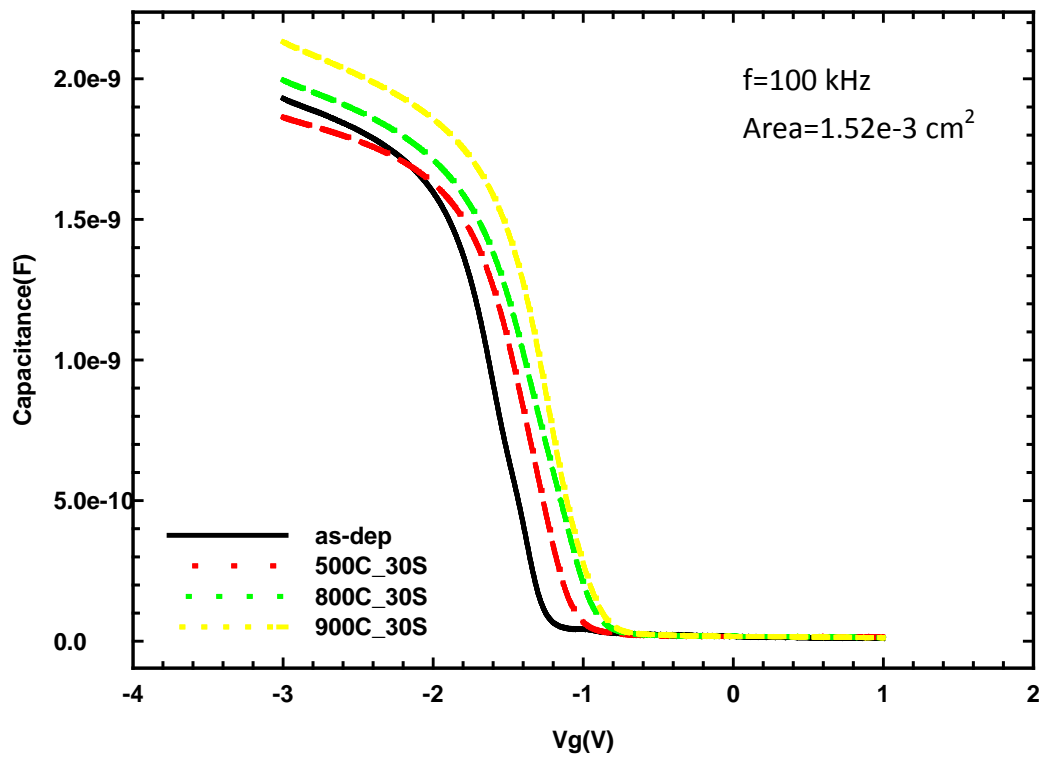
(b)

Figure 2.7.　(a) C-V and (b) J-V curve of 5 nm-HfO$_2$ samples with various PDA conditions.

(a)
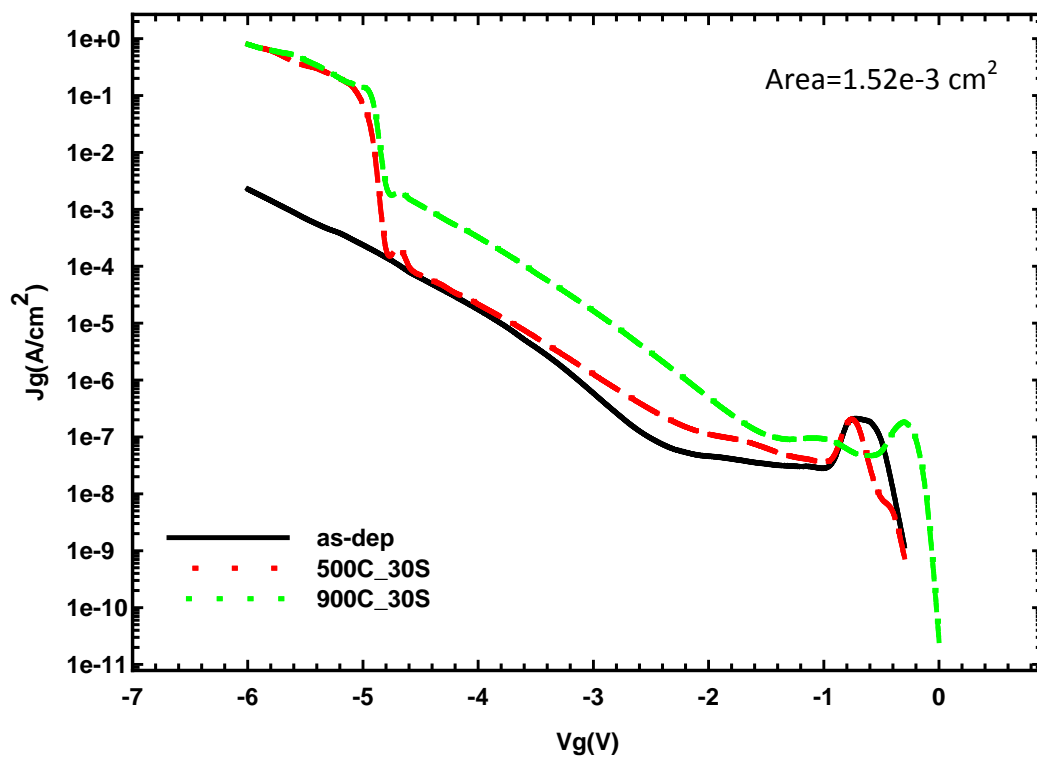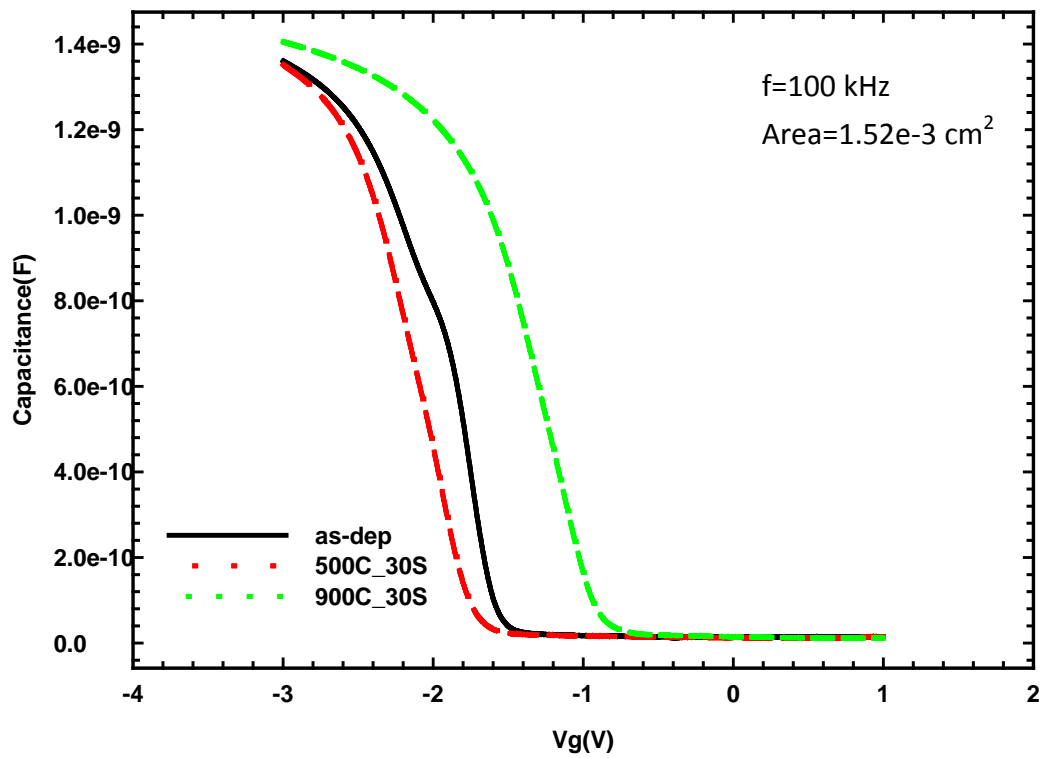
(b)

Figure 2.8. (a) C-V and (b) J-V curves of 10 nm-HfO$_2$ samples with various PDA conditions.
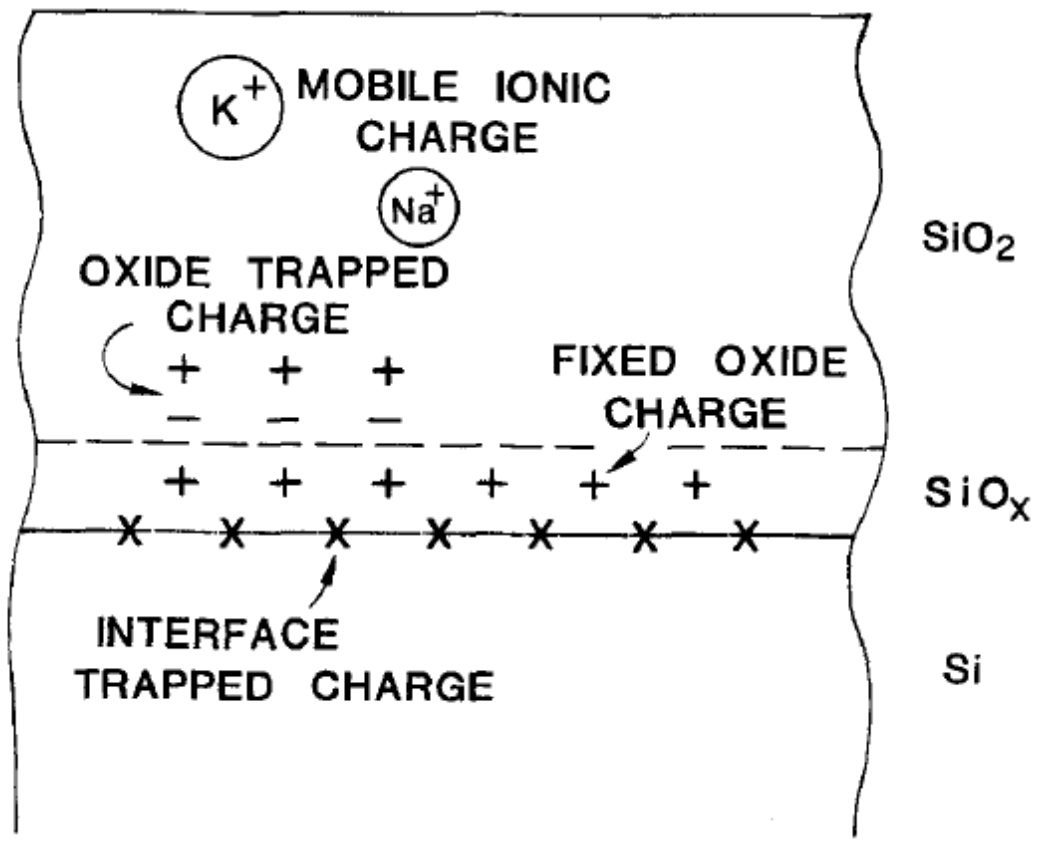
Figure 2.9. Schematic showing different types of charges presenting in the silicon dioxide/Si system [2-14].

(a)
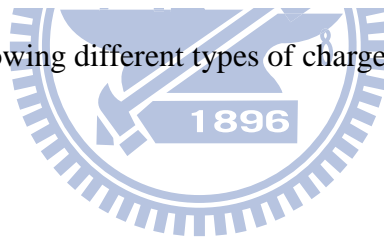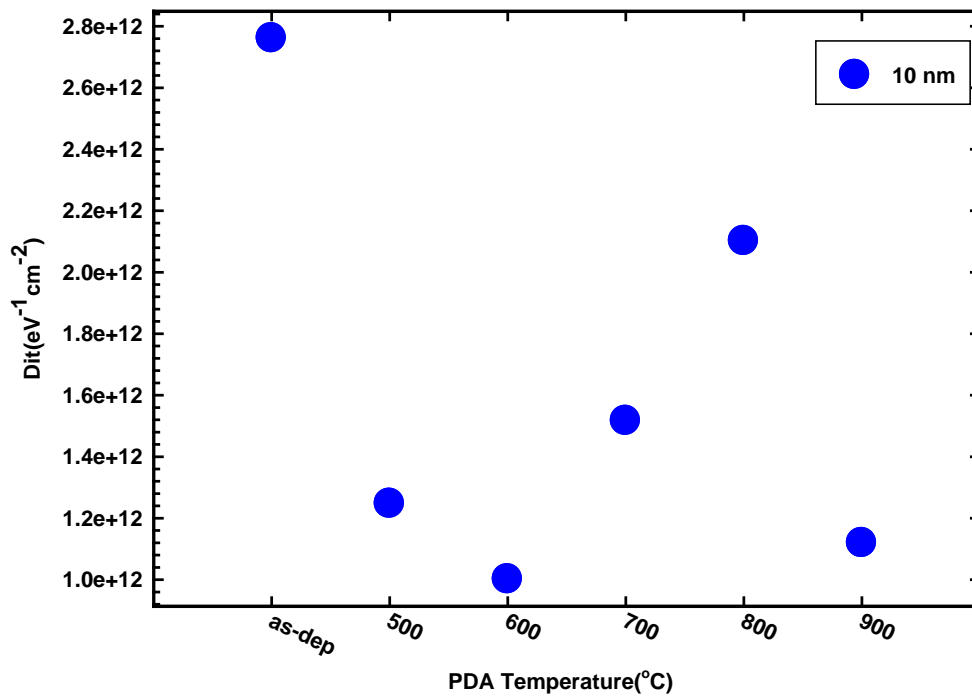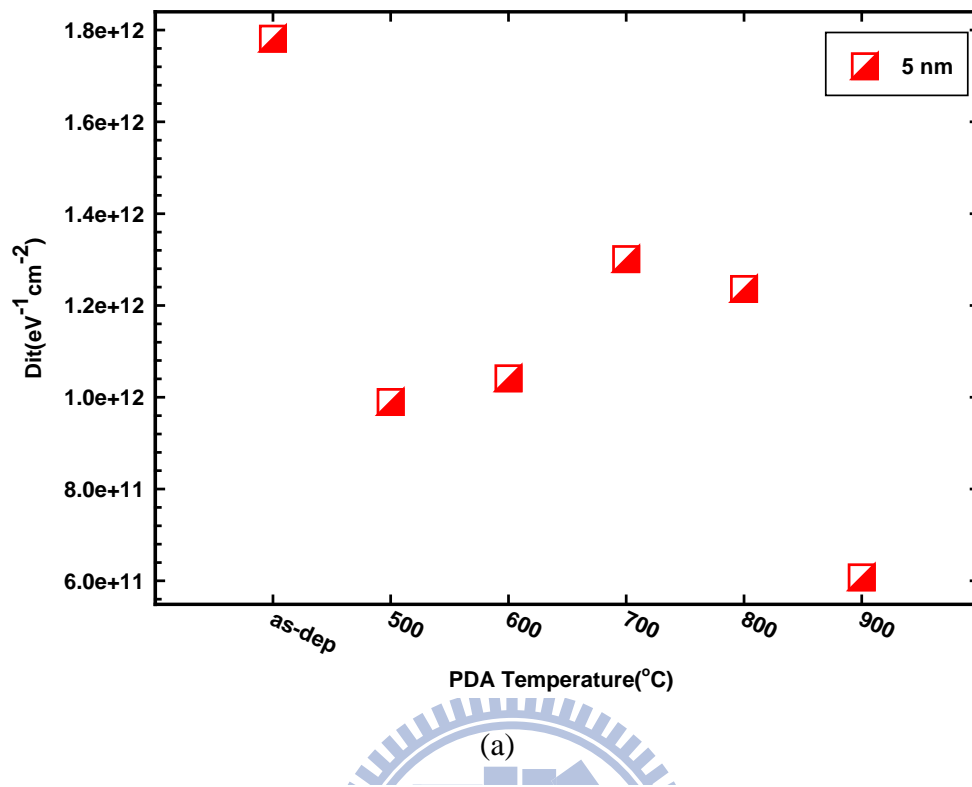
(b)

Figure 2.10. The extracted interface states density of (a) 5 nm and (b) 10 nm HfO$_2$ samples annealed at different temperatures for 30 sec.
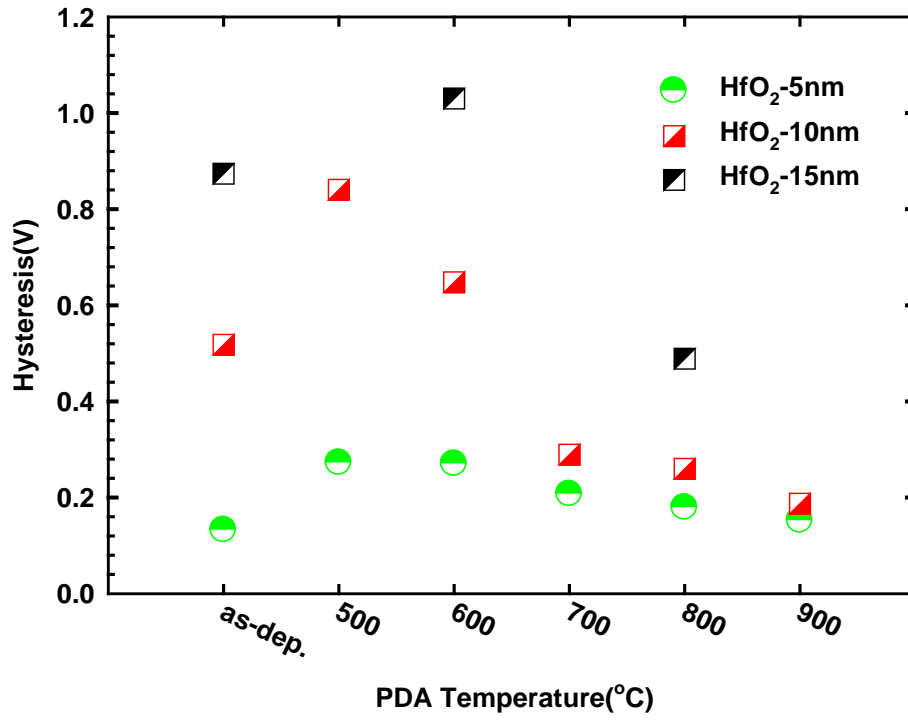
Figure 2.11. The extracted hysteresis window size for HfO$_2$ samples of different thicknesses.
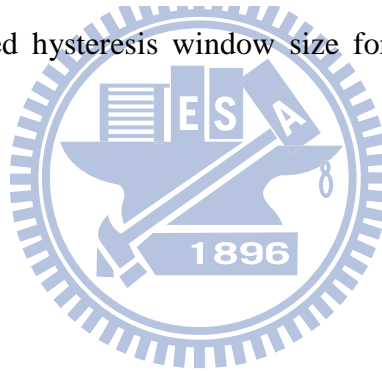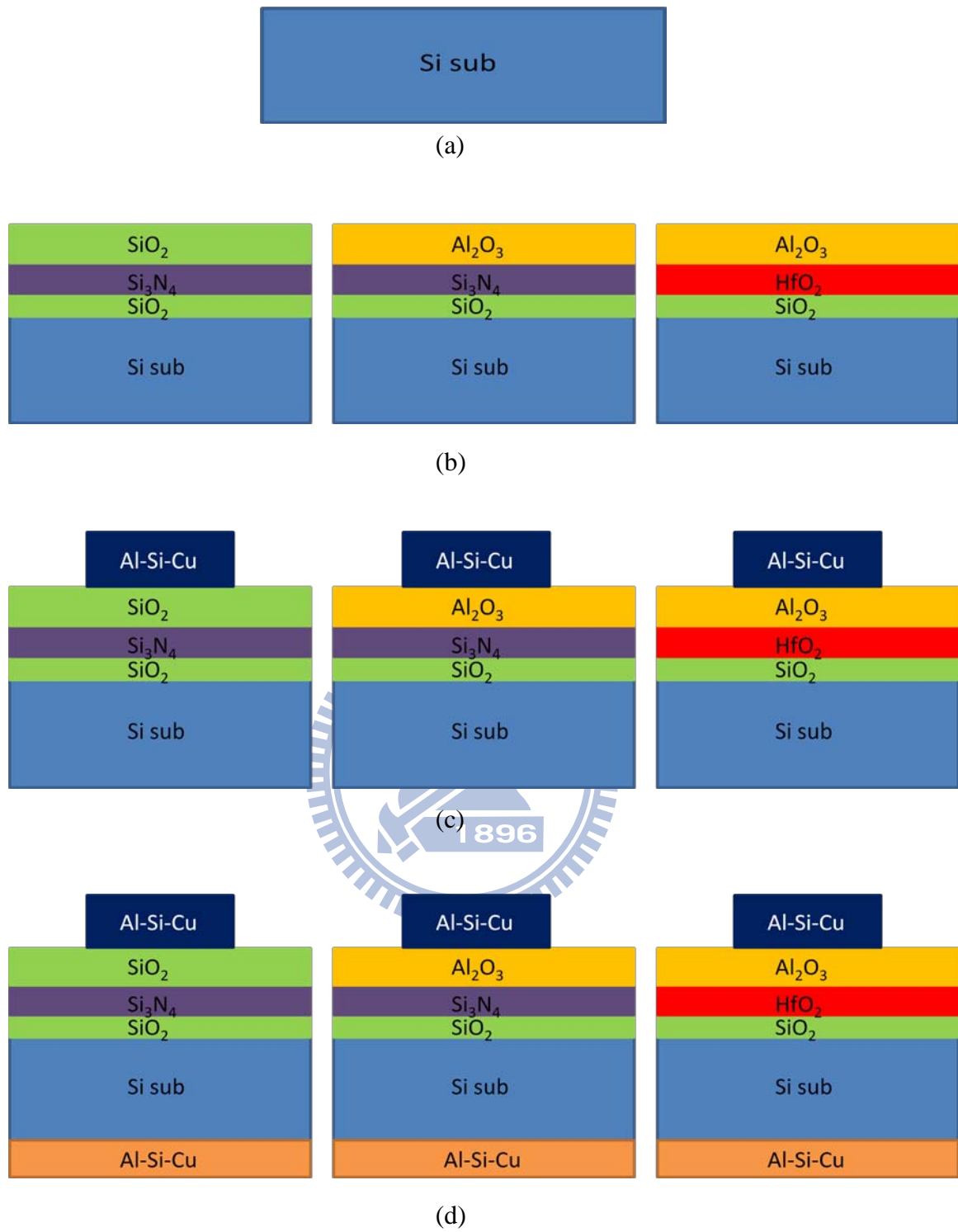
Figure 3.1.   Process flow of the three types of MOS capacitors.
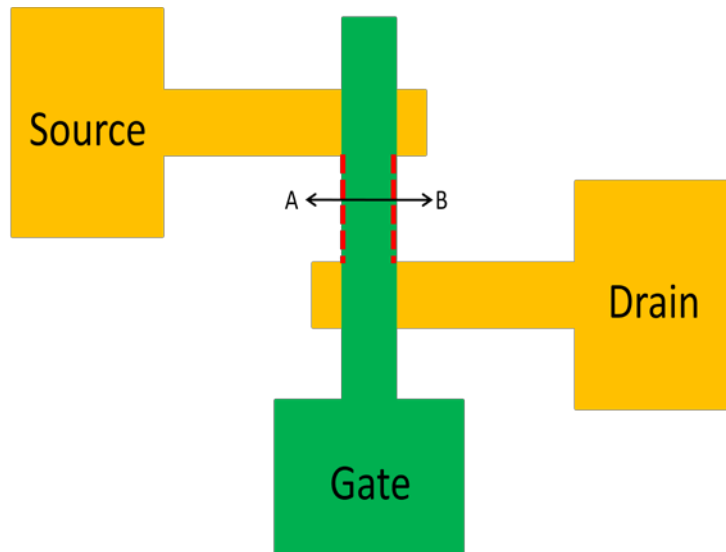
(a)
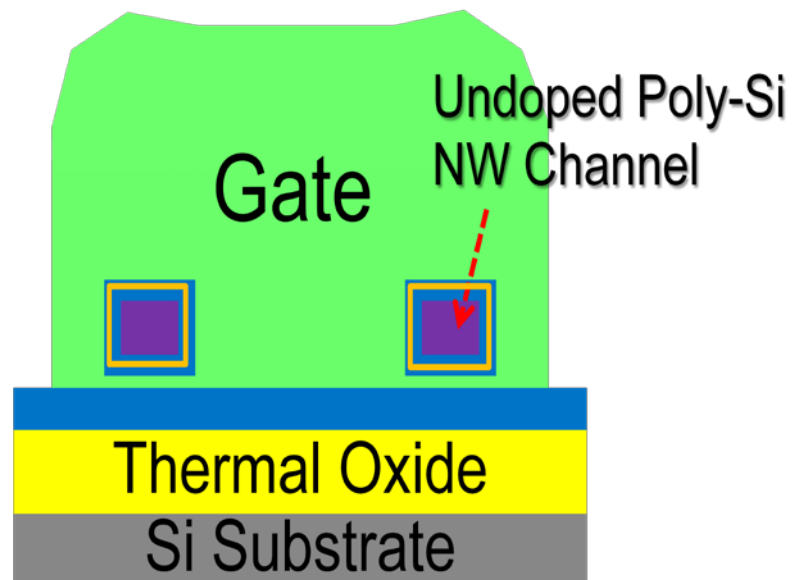
(b)

Figure 3.2.   (a)Top view and (b) cross-sectional view of the NW devices.

(a)

(b)

(c)

(d)

(e)

(f)

(g)

(h)

(i)

(j)

(k)
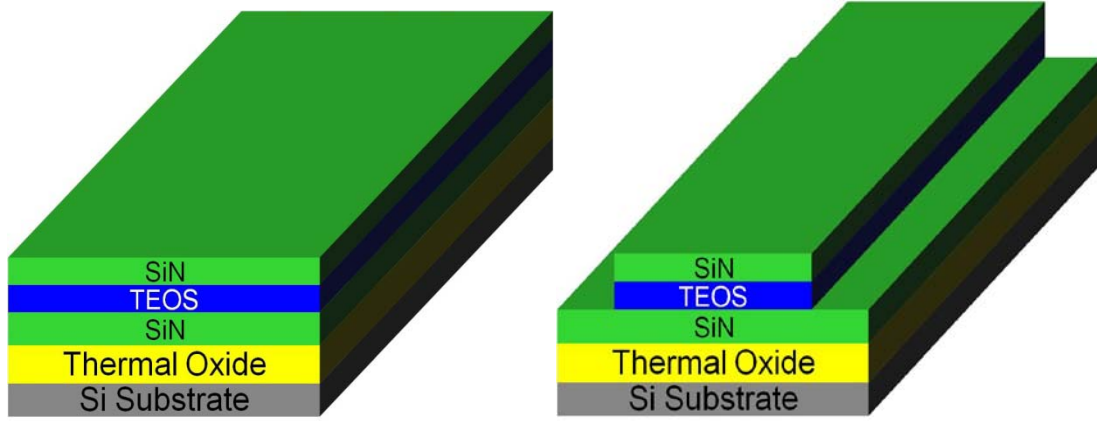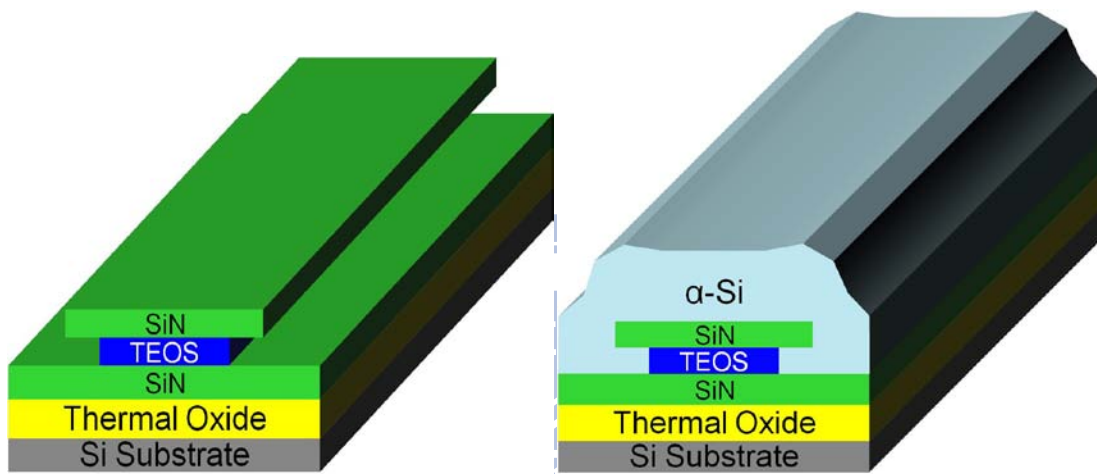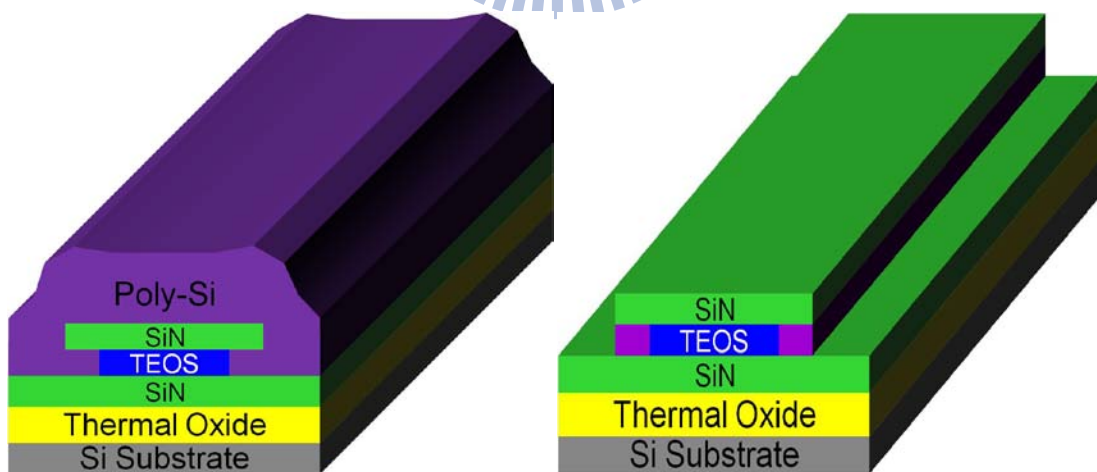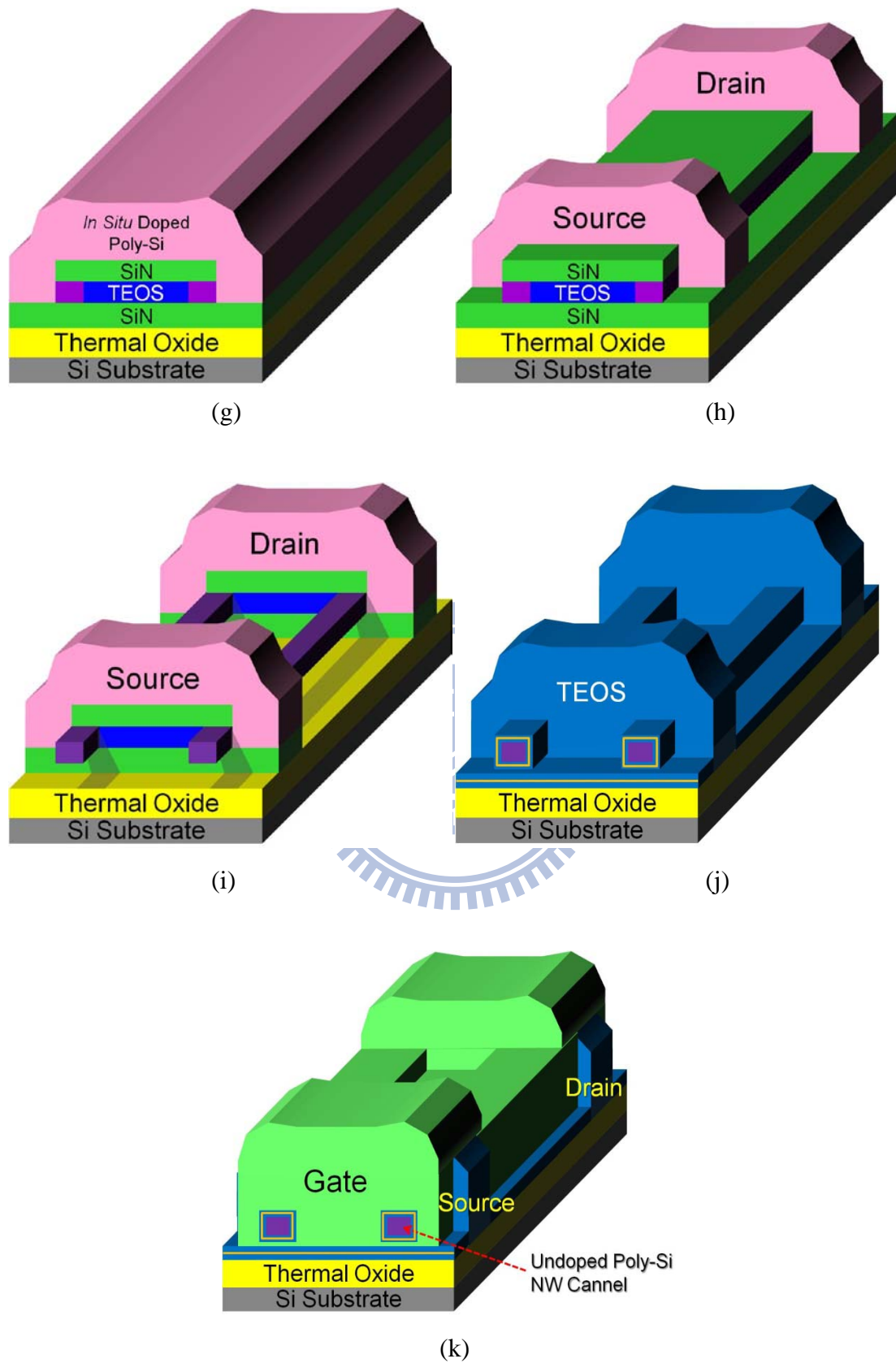
Figure 3.3.   Key process flow of the NW devices.

(a)

(b)

(c)
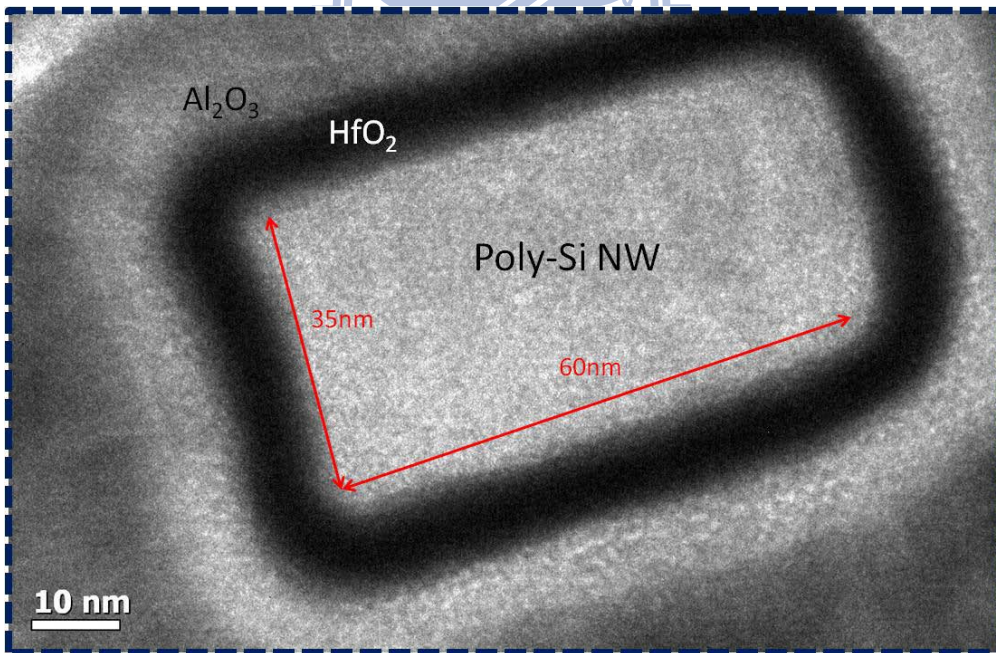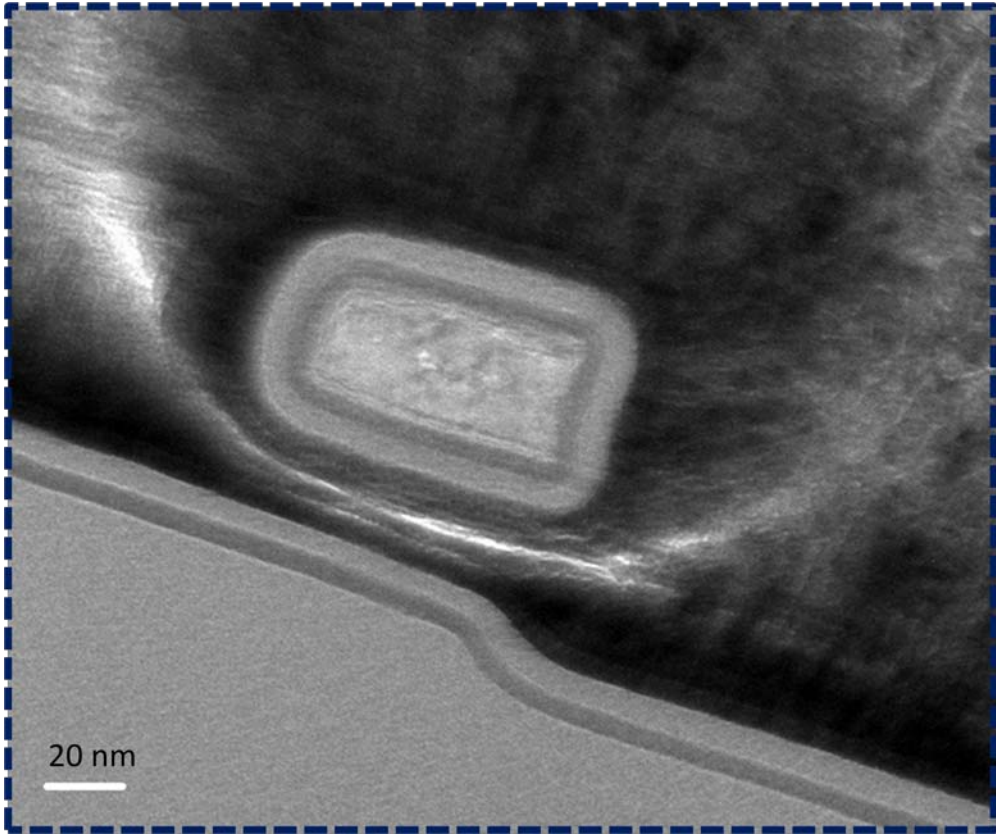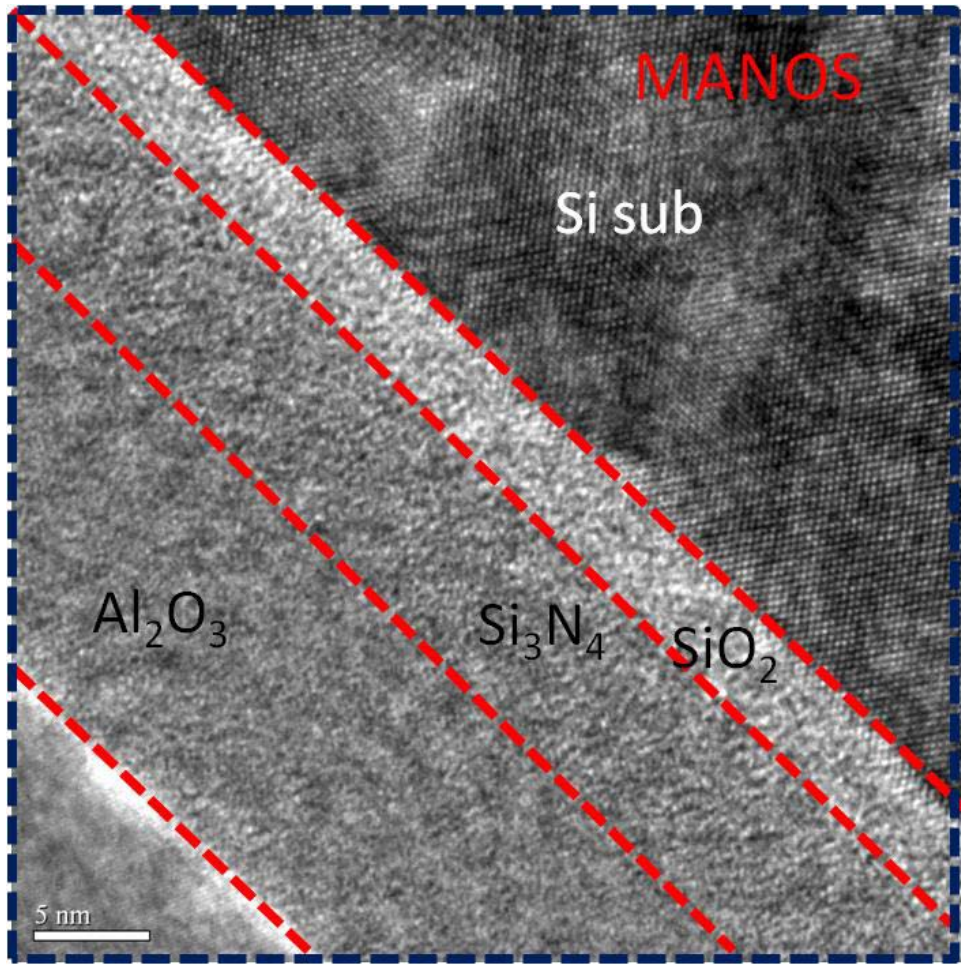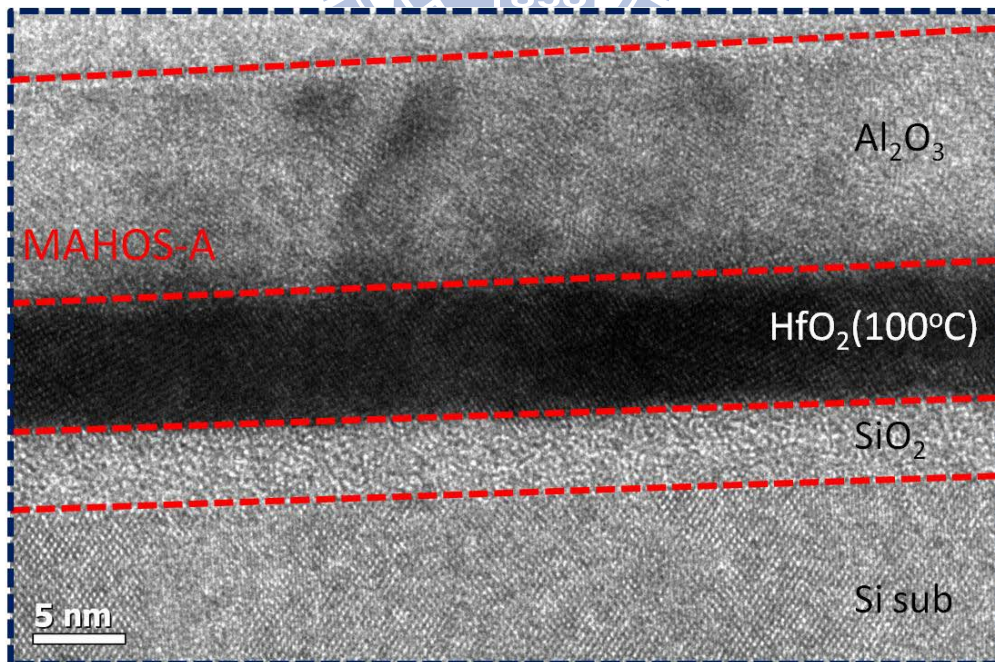
(d)
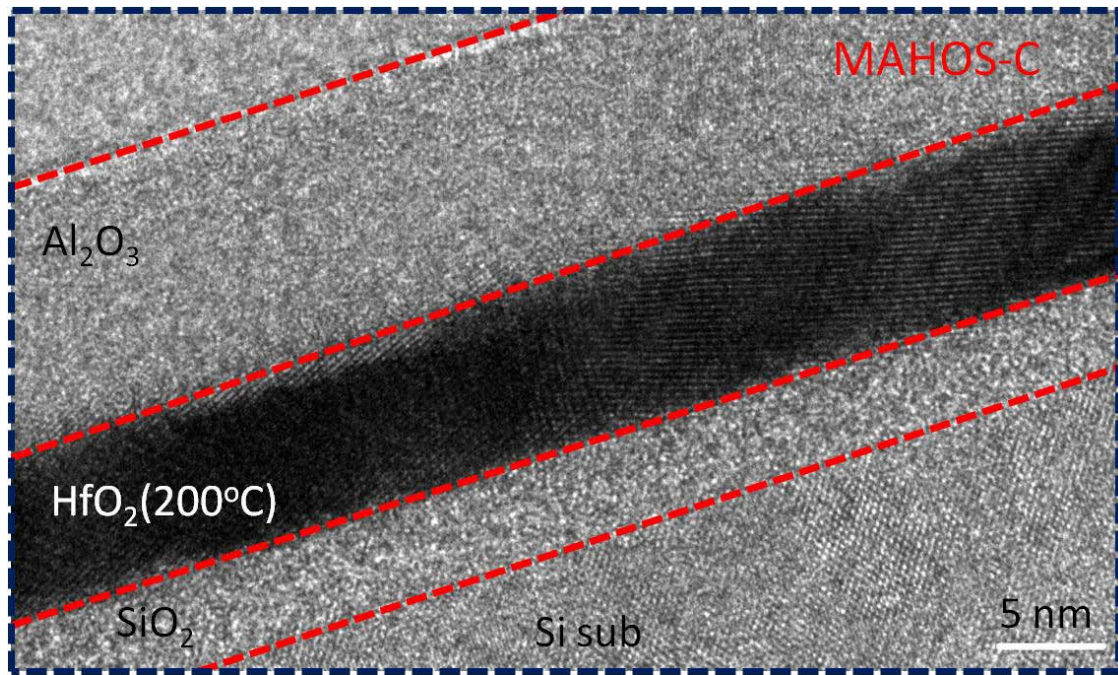
(e)

Figure 3.4. Cross-sectional TEM pictures of (a) NW-TONOS, (b) NW-TAHOS, (c) MOS-MANOS, (d) MOS-MAHOS-A, and (e) MAHOS-C devices.
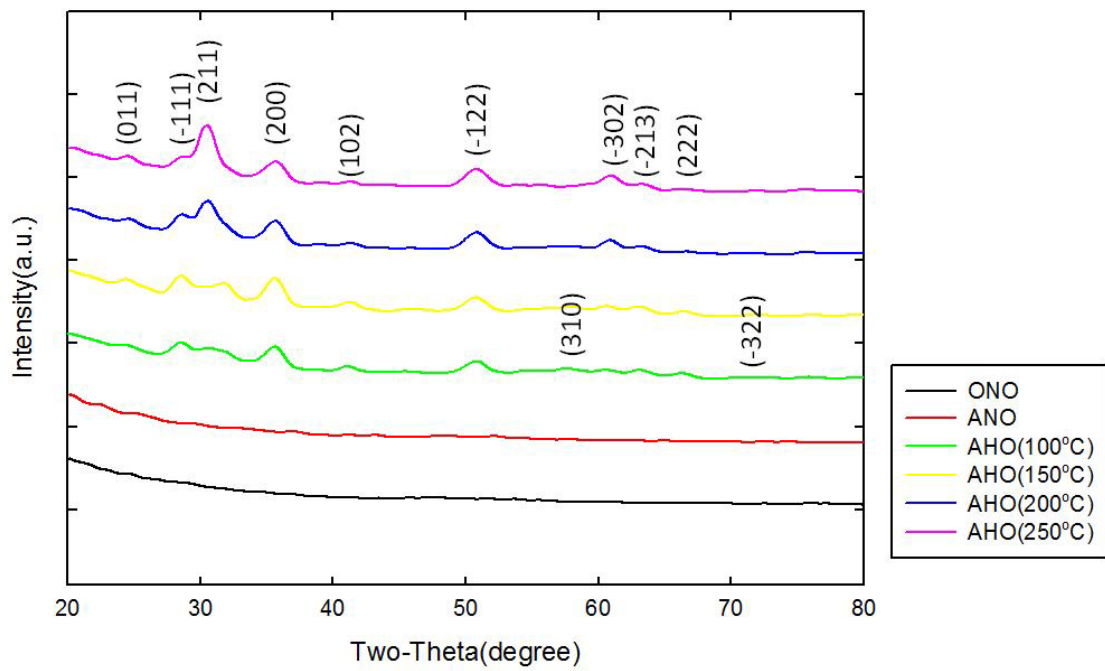
Figure 3.5.   XRD data of the dielectric films in MOS devices.
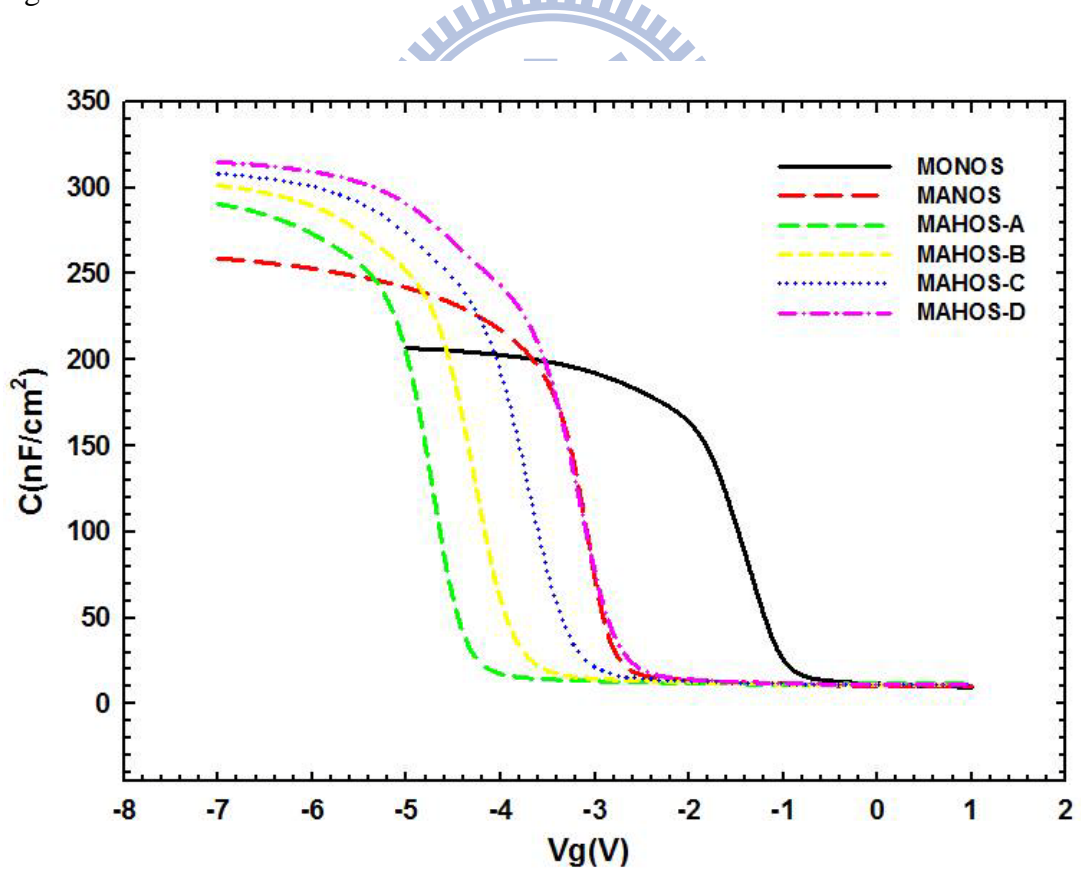
Figure 3.6.   Basic C-V curves of the MOS capacitors (the capacitance has been normalized to the area).

(a)
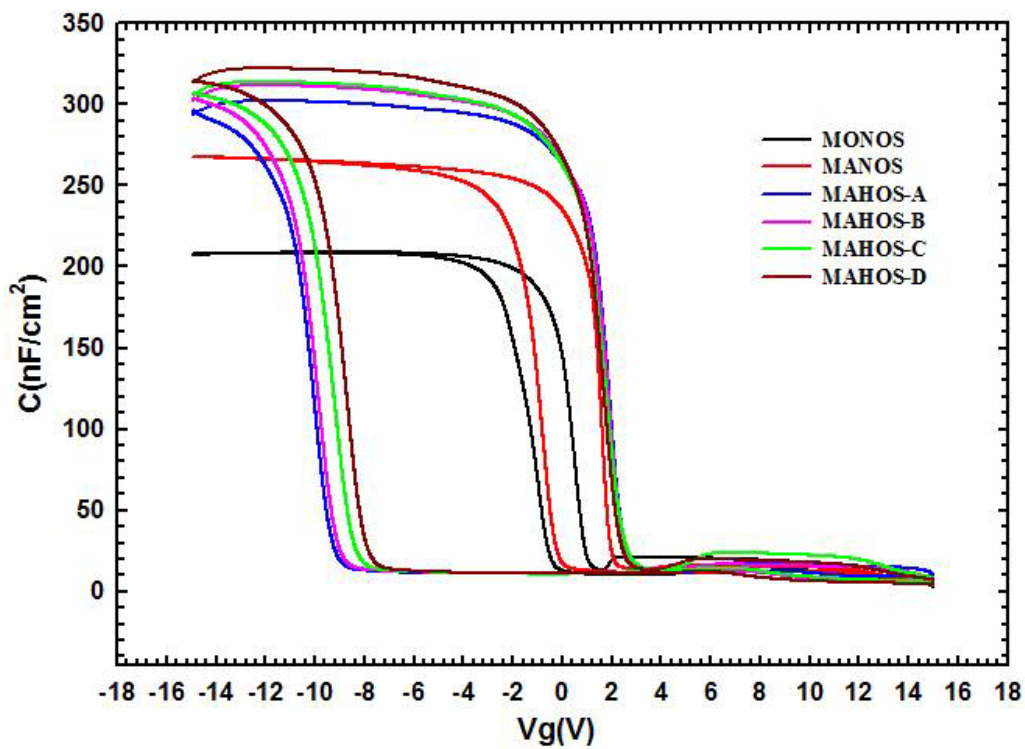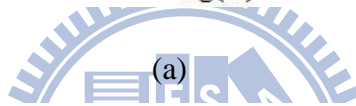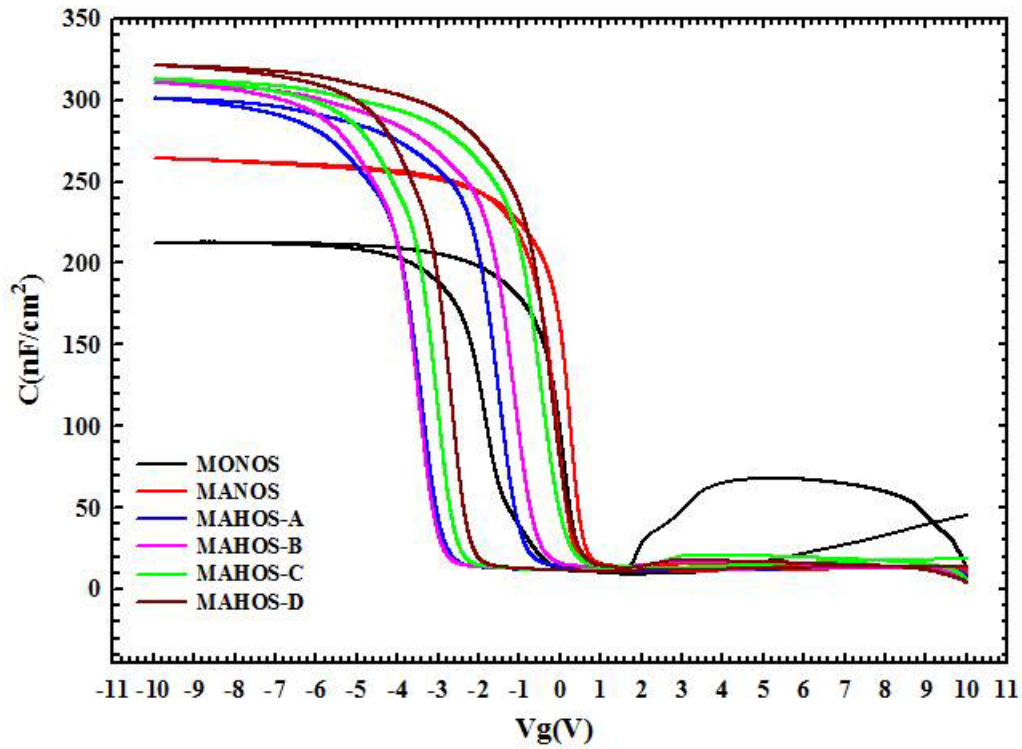
(b)

Figure 3.7. C-V curves of MOS capacitors measured with a sweeping Vg range of (a) ±10 V and (b) ±15 V.

(a)

(b)

(c)
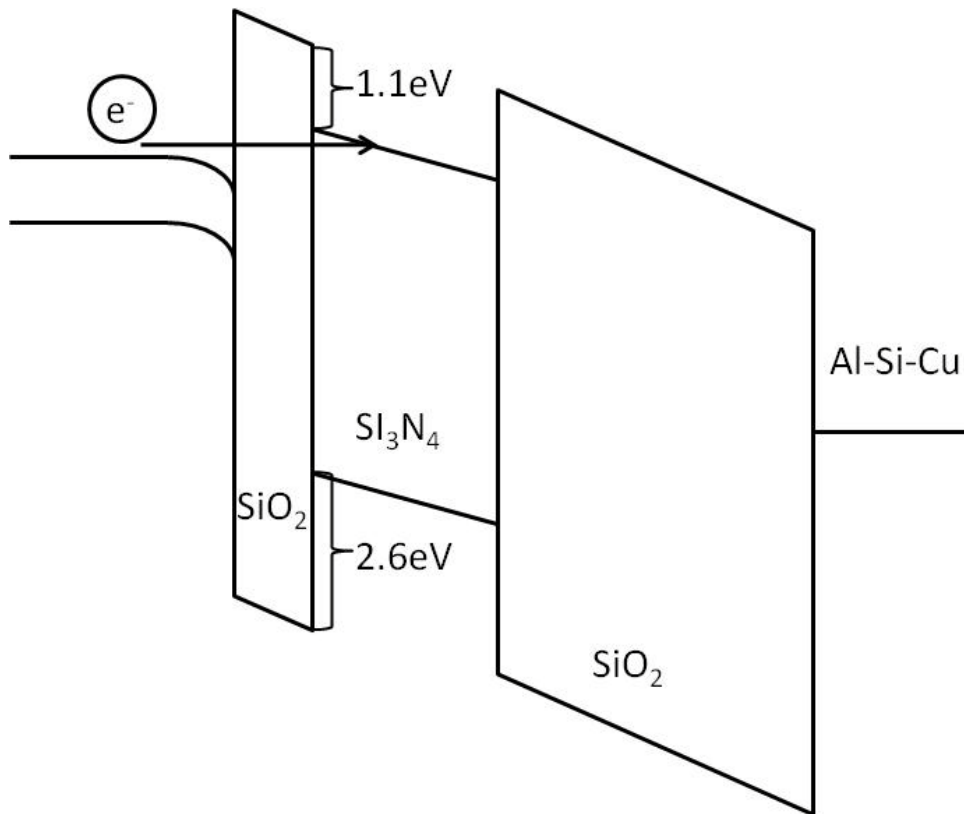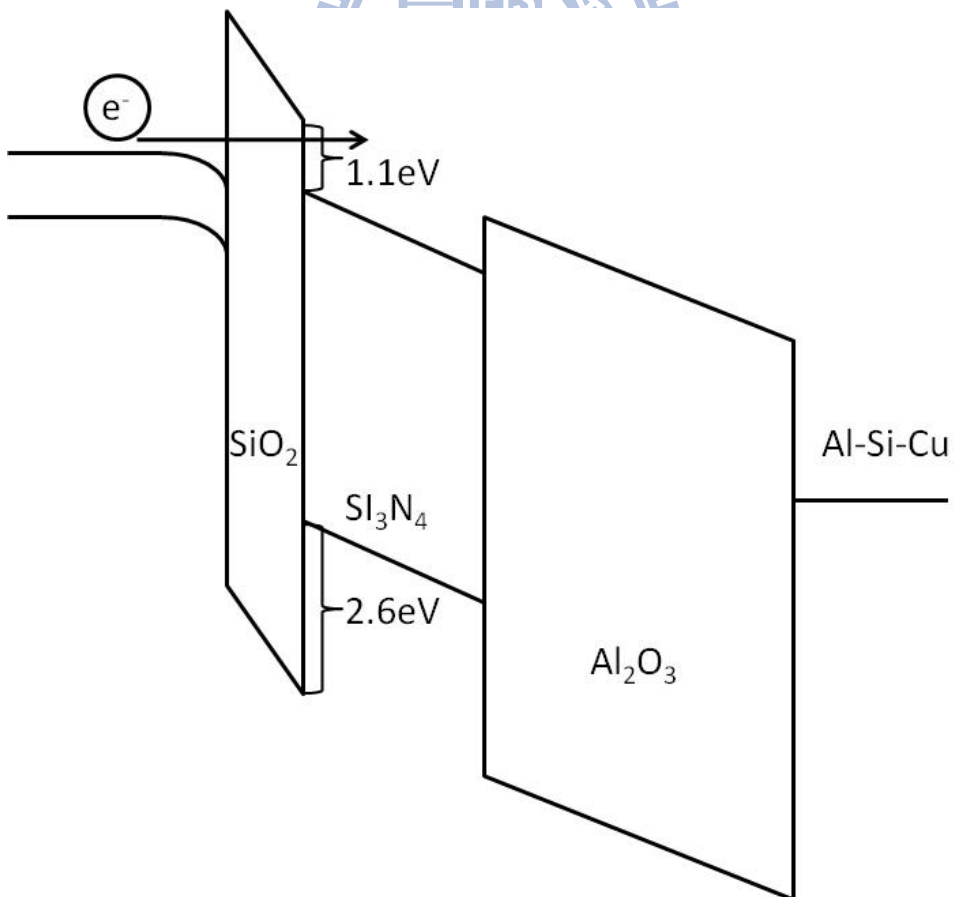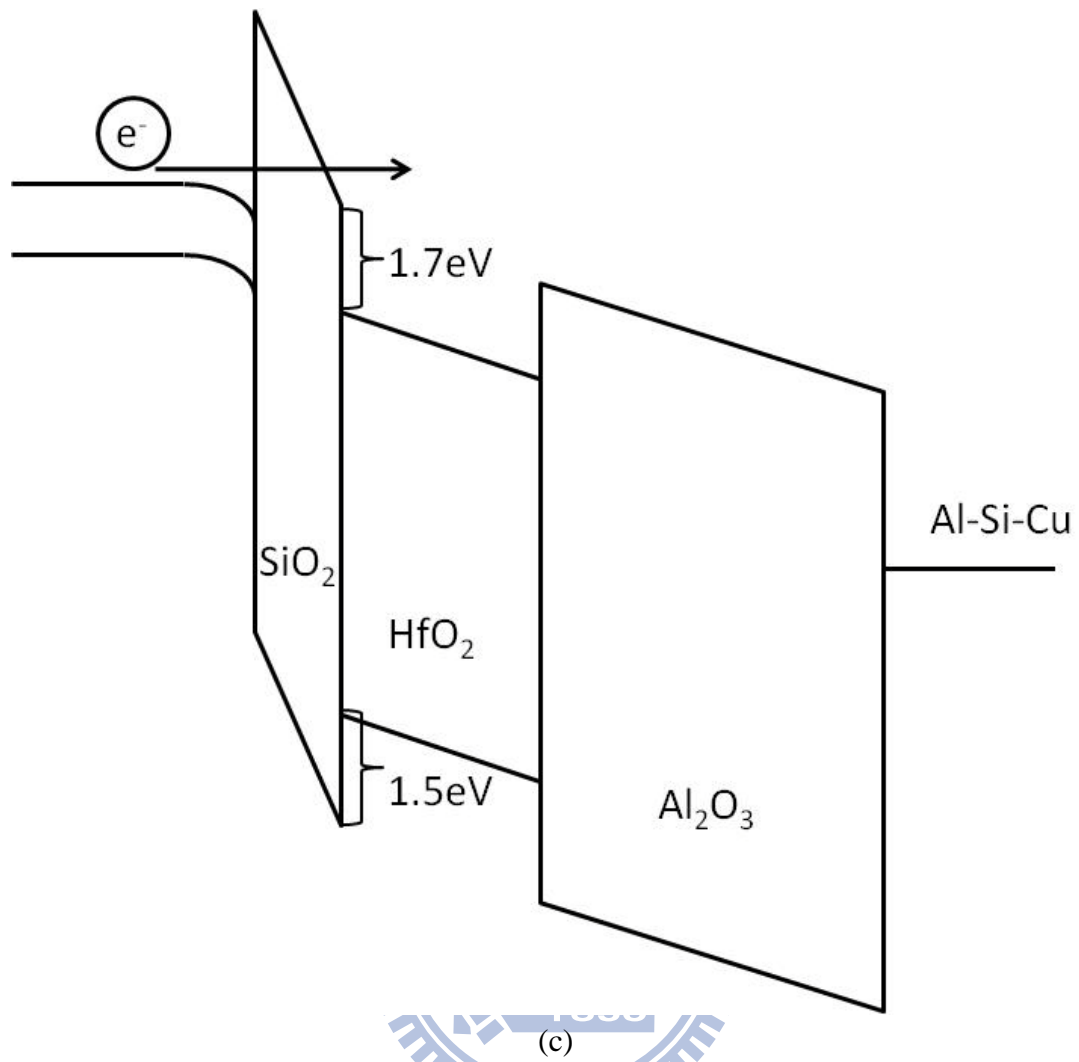
Figure 3.8.   Band diagrams under a positive bias of (a) MONOS, (b) MANOS, and (c) MAHOS capacitors.
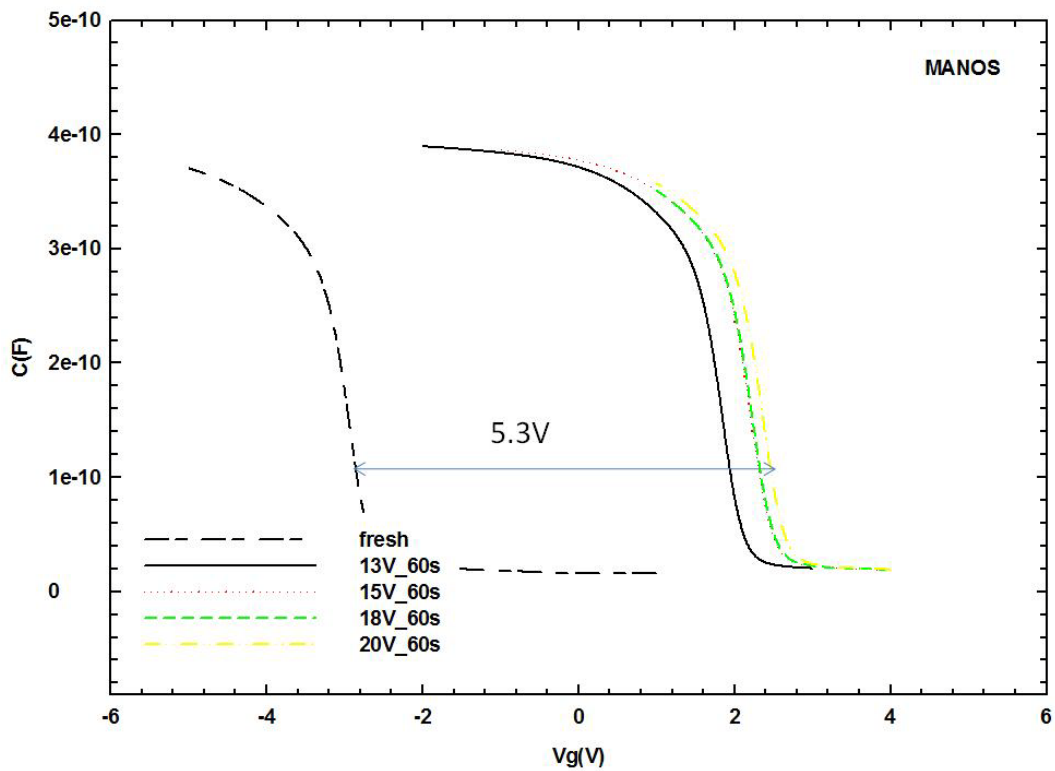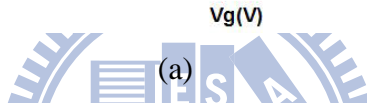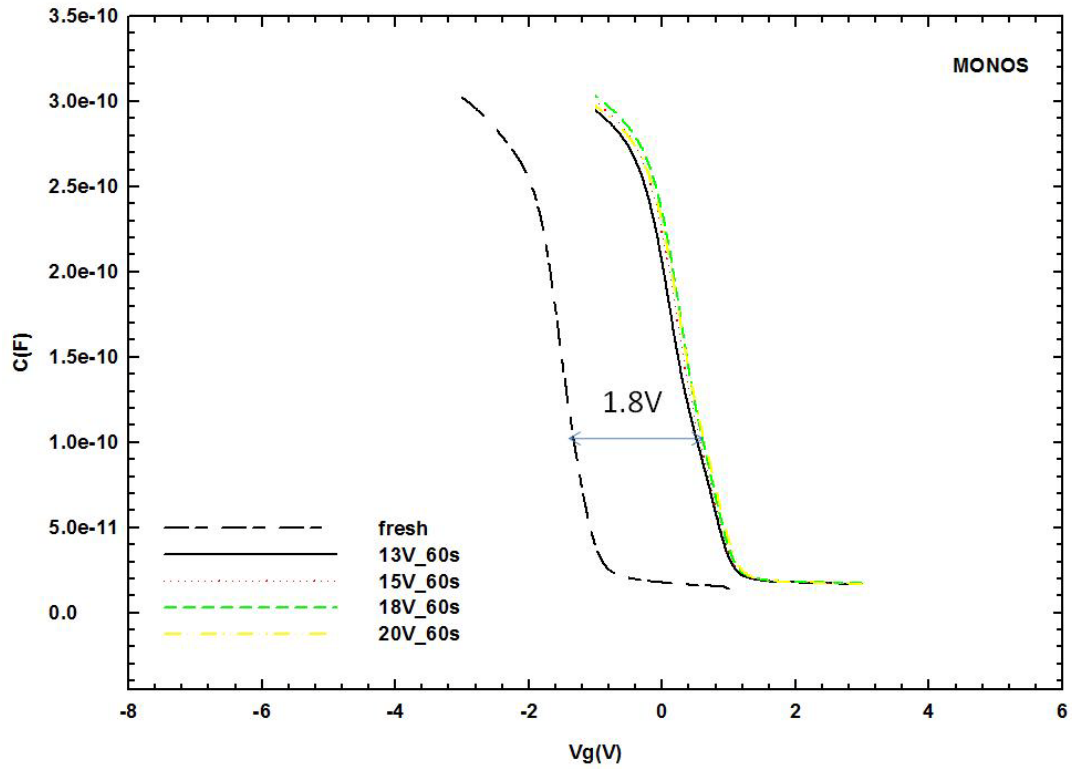
Figure 3.9. C-V plots of the samples before and after applying a positive gate bias
for 60 s. (a) MONOS, (b) MANOS.

(c)

(d)
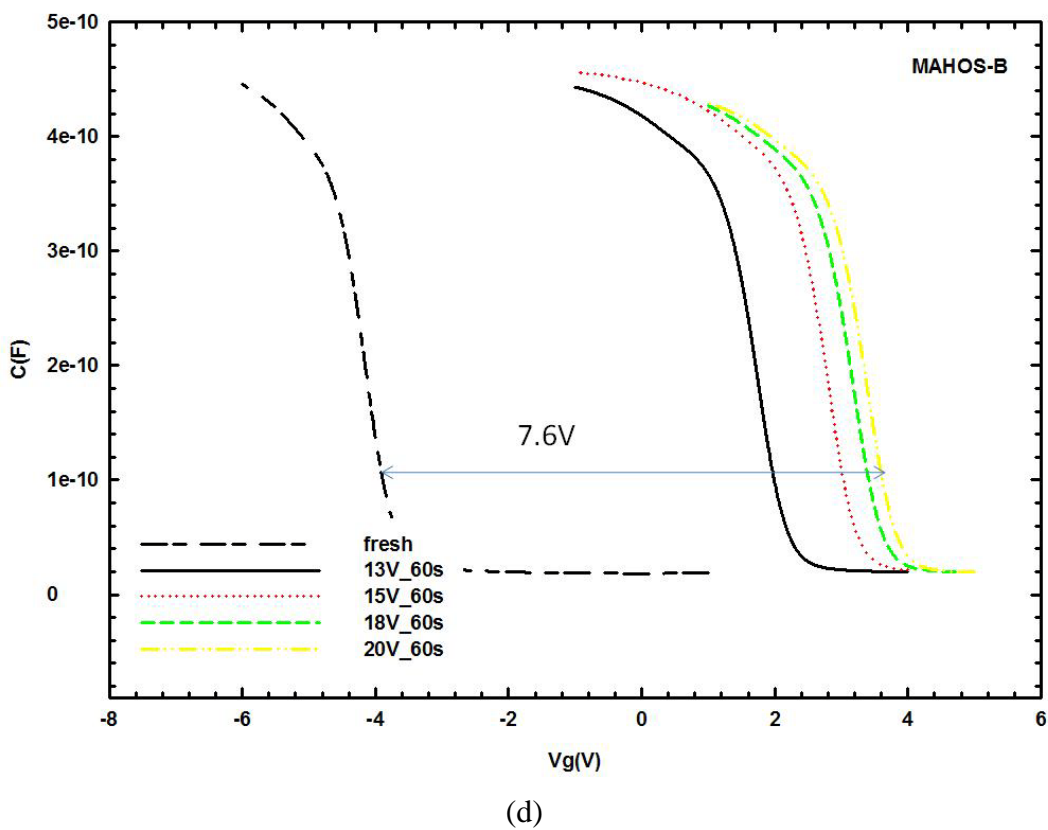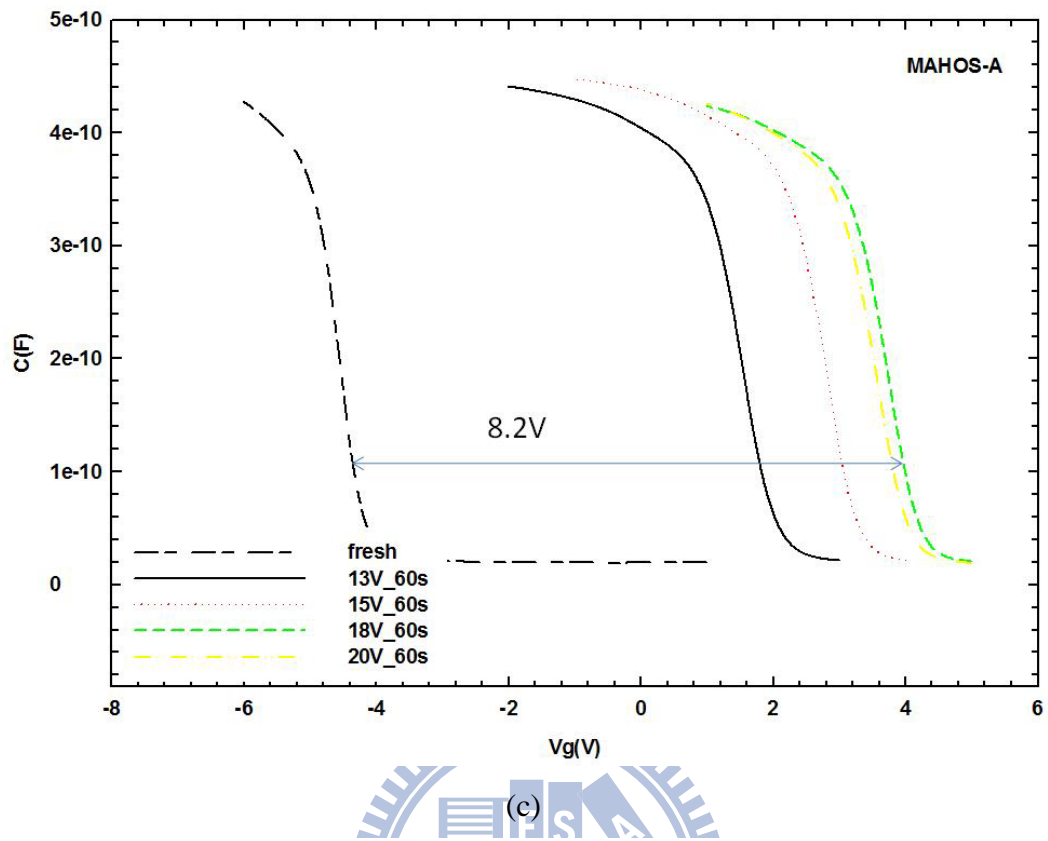
Figure 3.9.   C-V plots of the samples before and after applying a positive gate bias for 60 s. (c) MAHOS-A, (d) MAHOS-B.
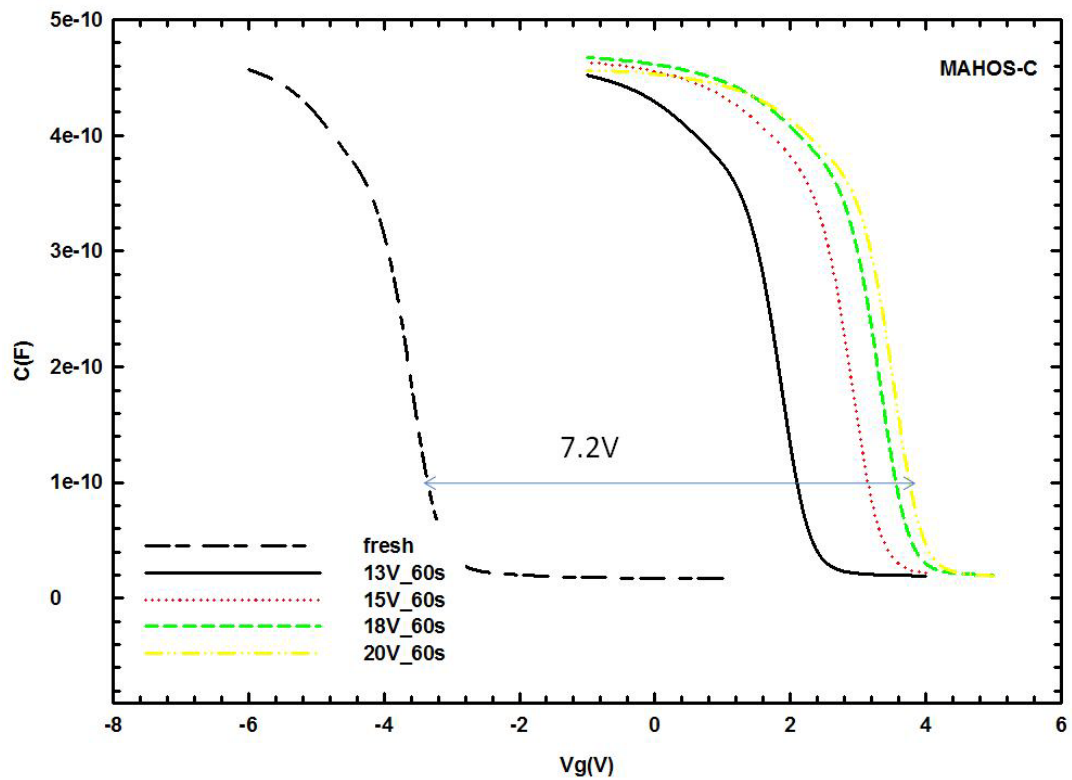
(e)
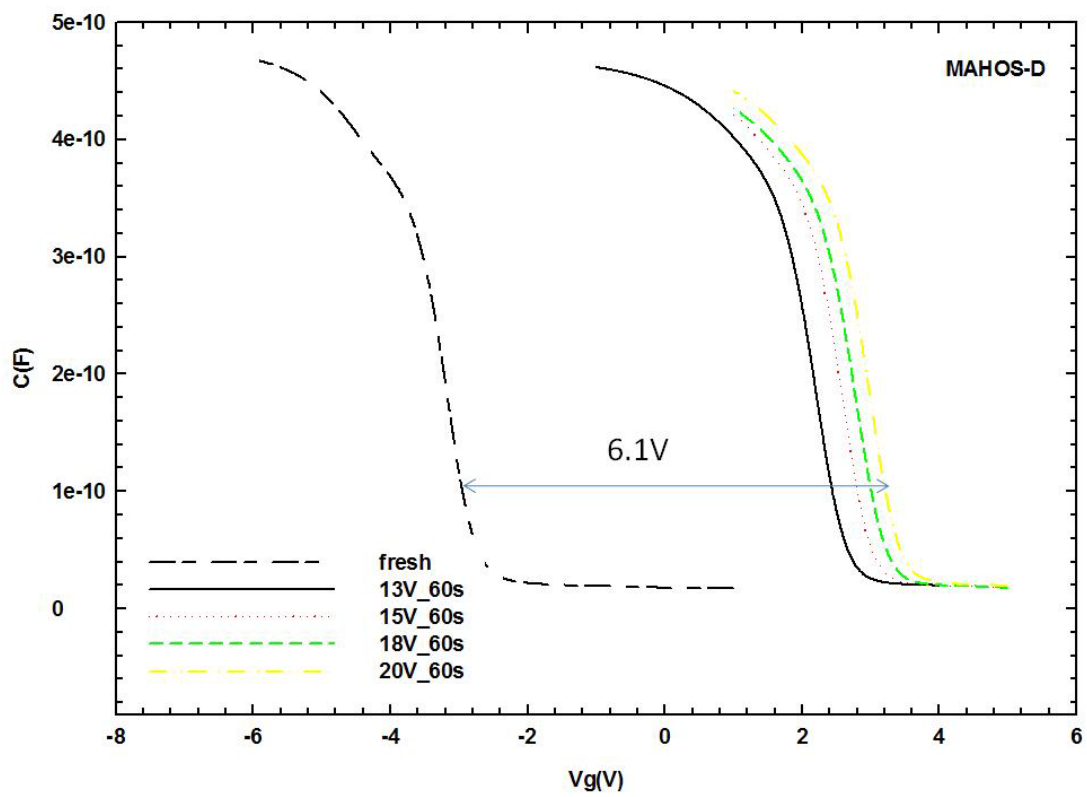
(f)

Figure 3.9. C-V plots of the samples before and after applying a positive gate bias for 60 s. (e) MAHOS-C, (f) MAHOS-D.
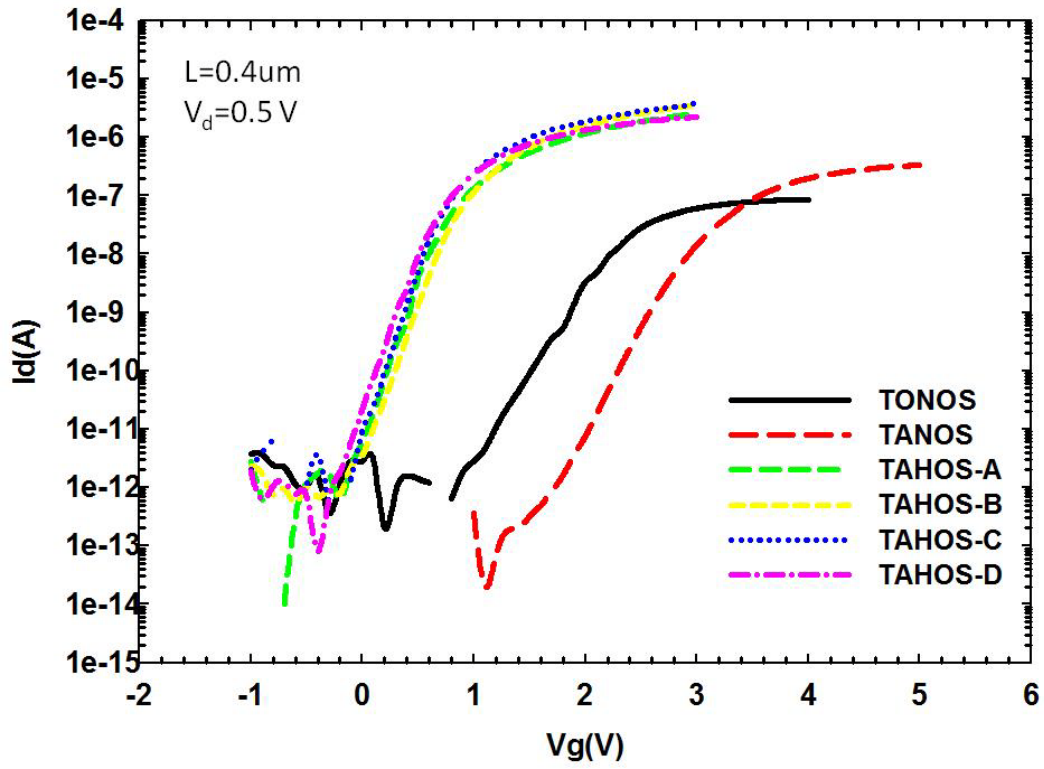
Figure 3.10.　Transfer characteristics of the fabricated devices.

(a)

(b)
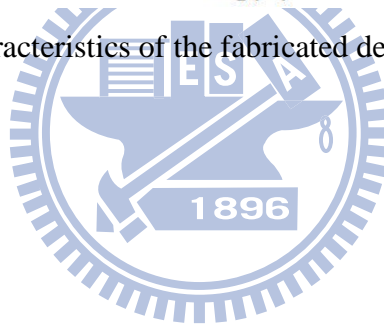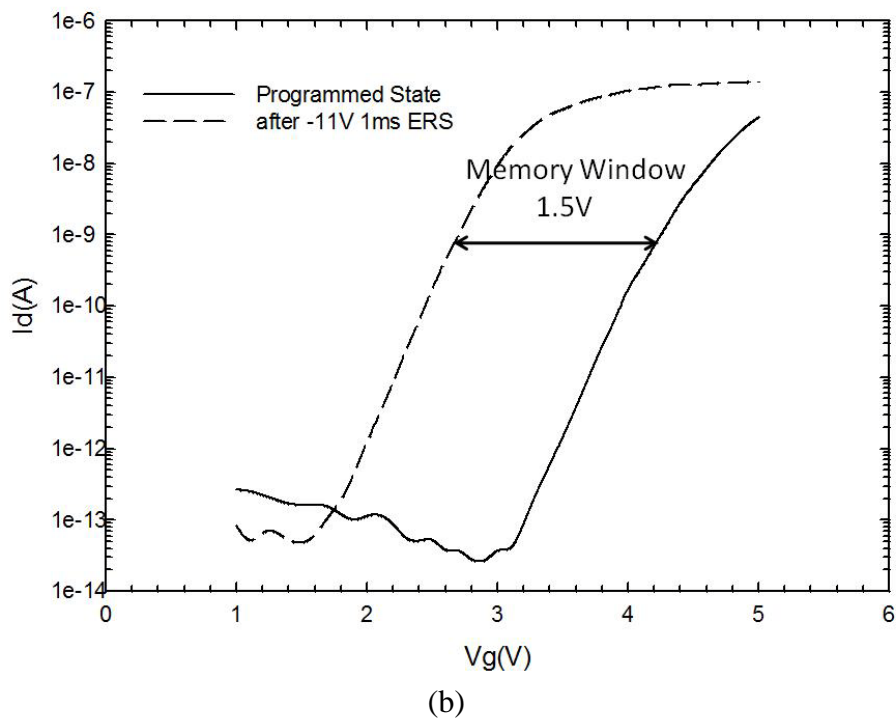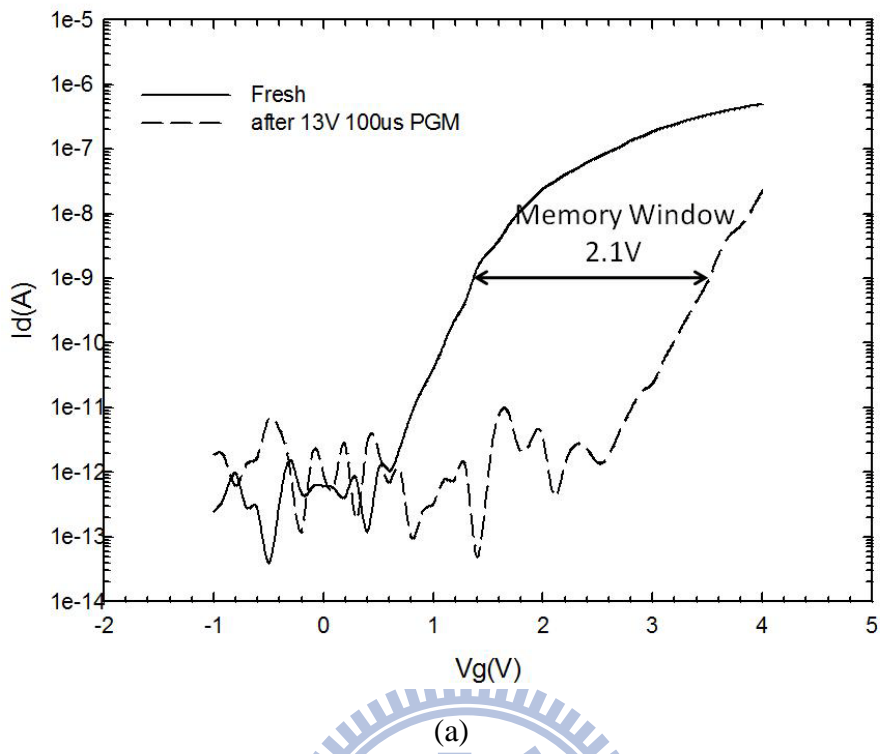
Figure 3.11. Transfer I-V curves of a TANOS device after (a) programming and (b) erasing operation with the positive and negative bias conditions, respectively.
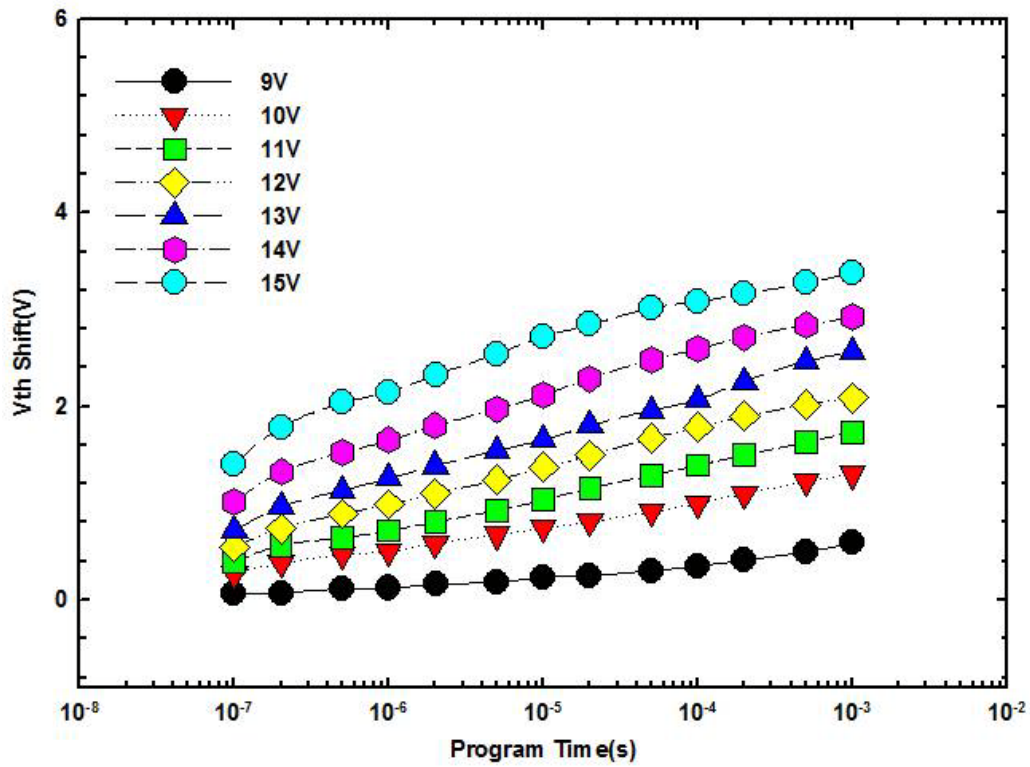
(a)
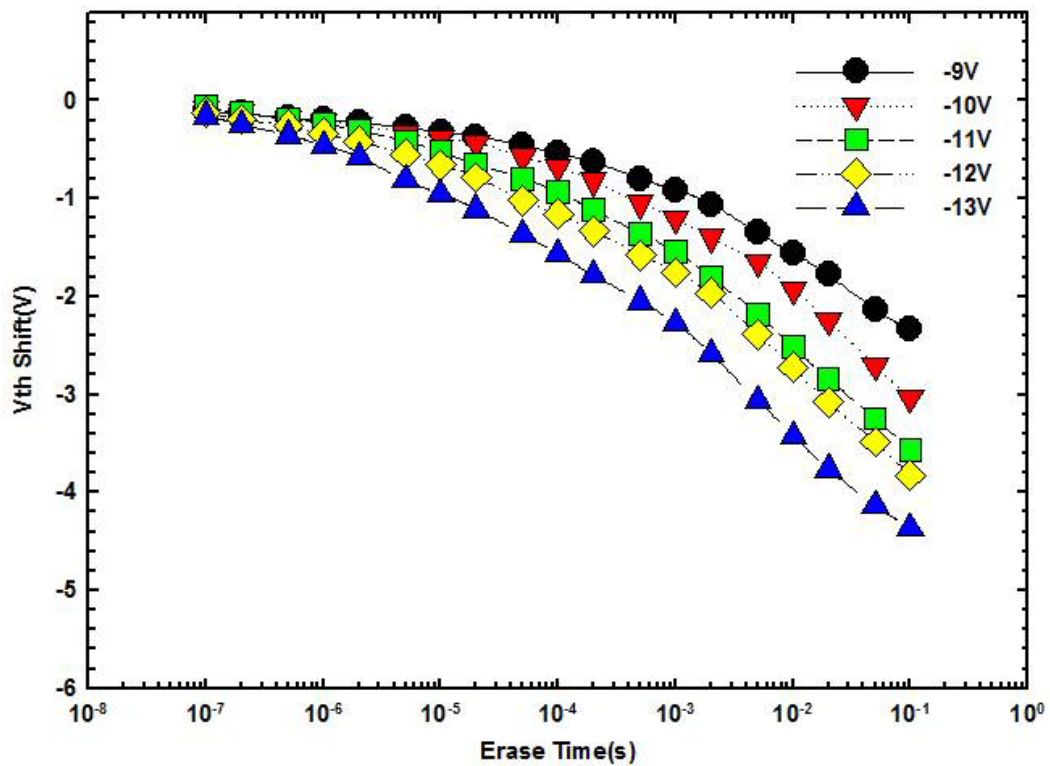
(b)

Figure 3.12.   (a) Programming and (b) erasing characteristics of NW-TONOS devices with different gate biases.
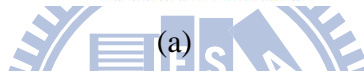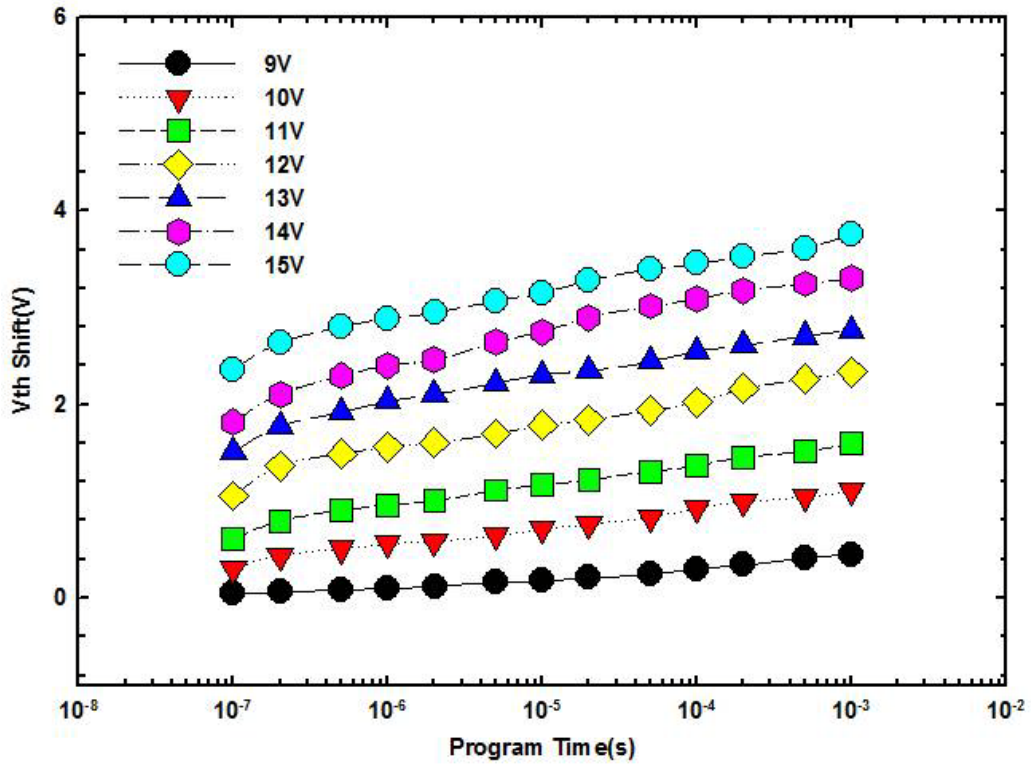
(a)
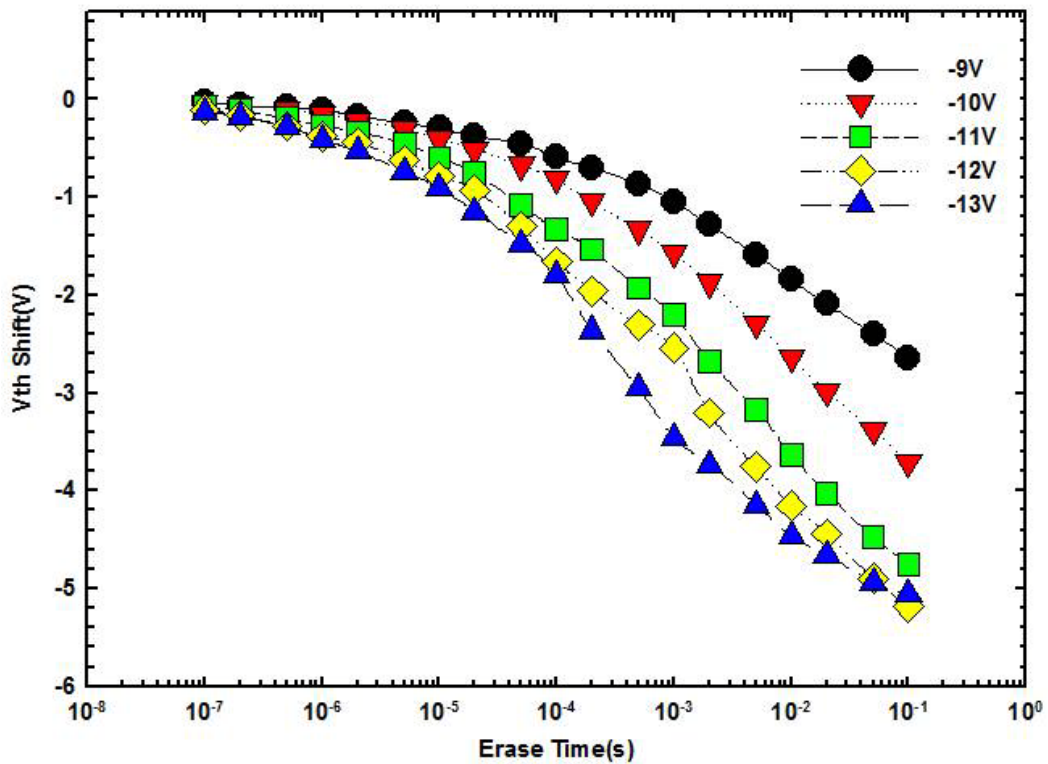
(b)

Figure 3.13.　(a) Programming and (b) erasing characteristics of NW-TANOS devices with different gate biases.
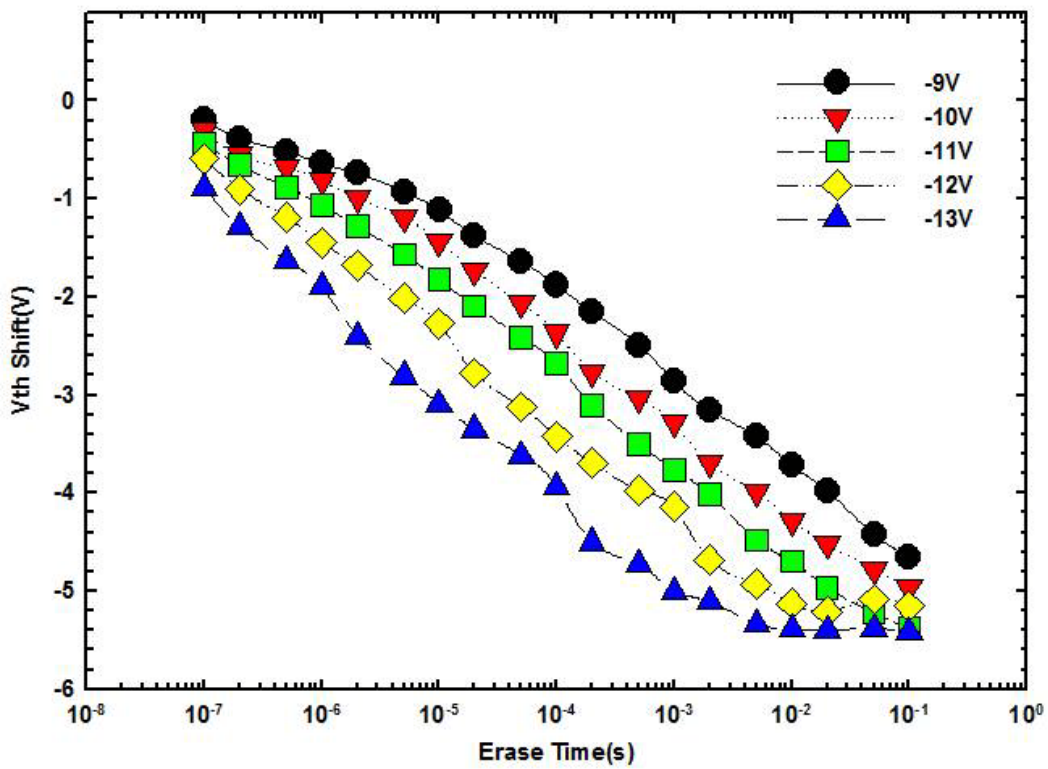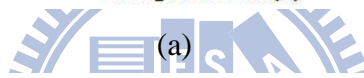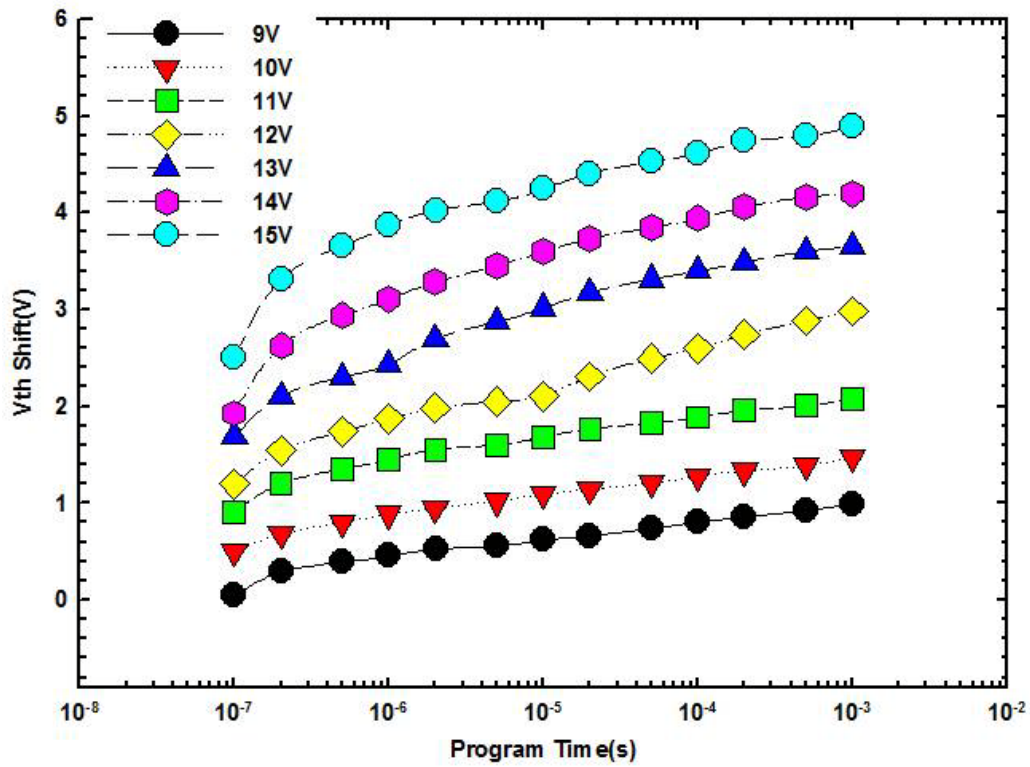
Figure 3.14.　(a) Programming and (b) erasing characteristics of NW-TAHOS devices with different gate biases.

(a)

(b)

(c)
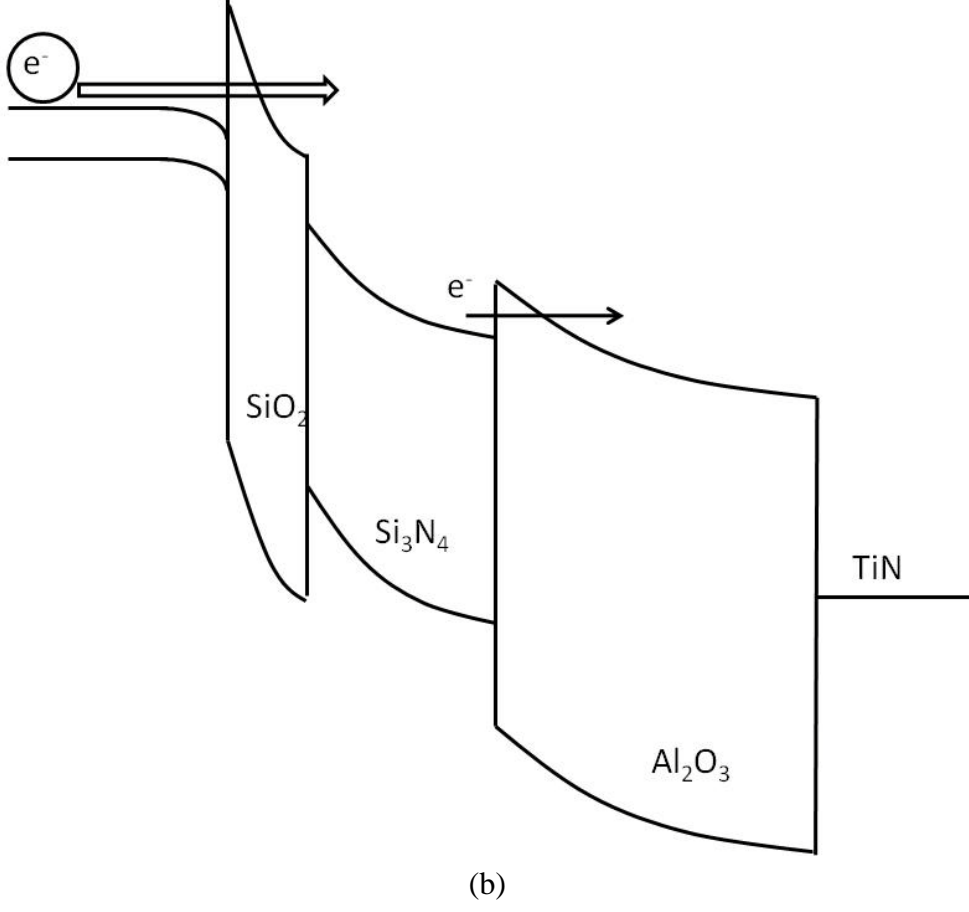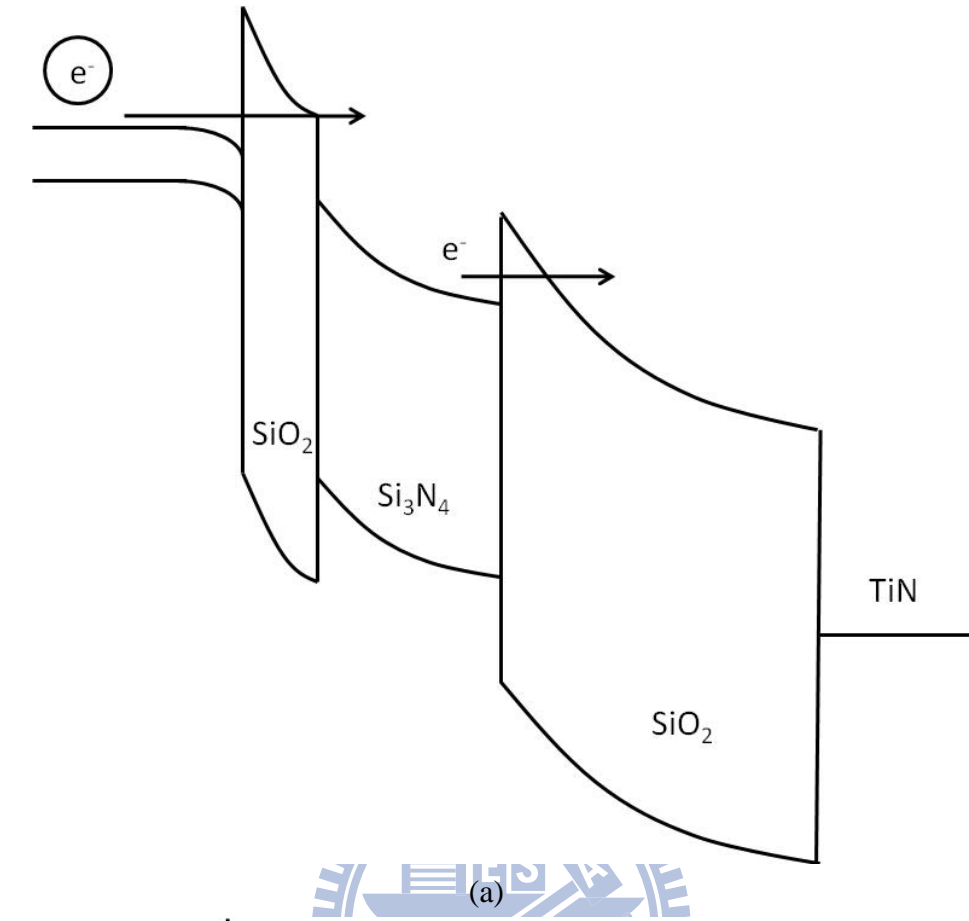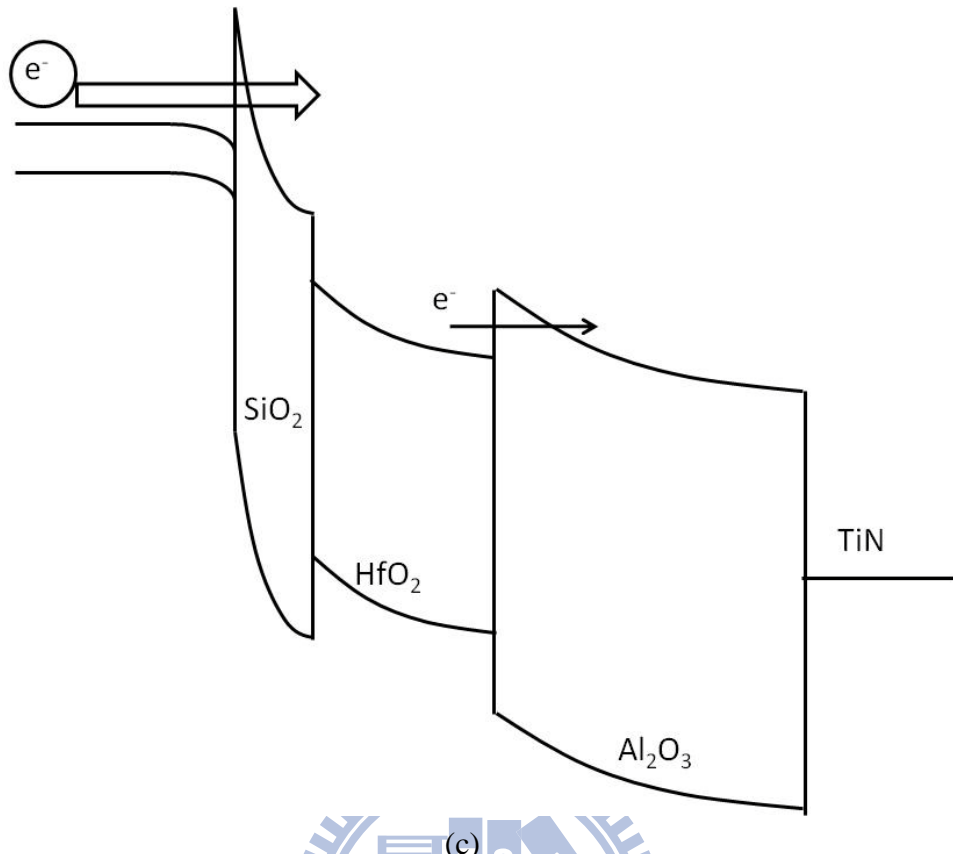
Figure 3.15. Schematic band diagrams of (a) TONOS, (b) TANOS, and (c) TAHOS devices under a positive programming bias.
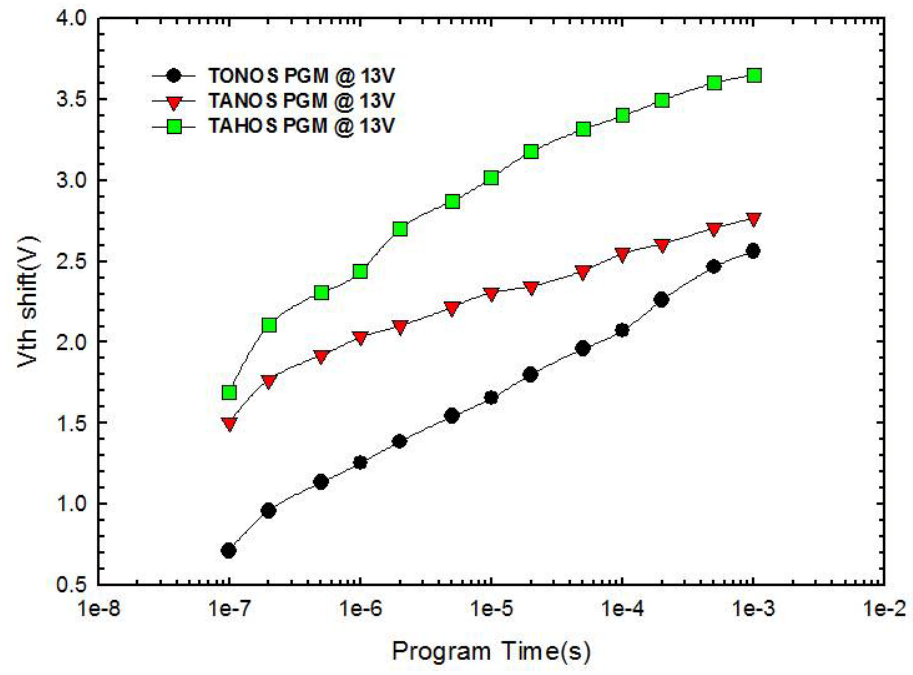
Figure 3.16. Comparisons of programming characteristics of the three types of devices under the same programming bias.

(a)

(b)
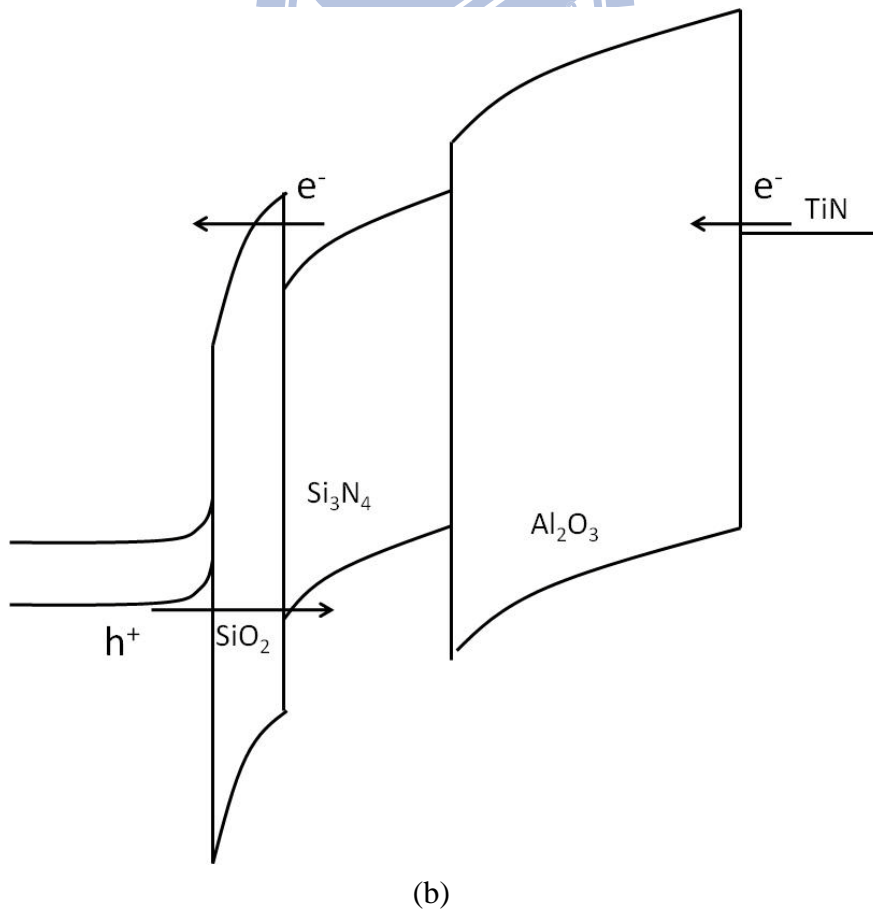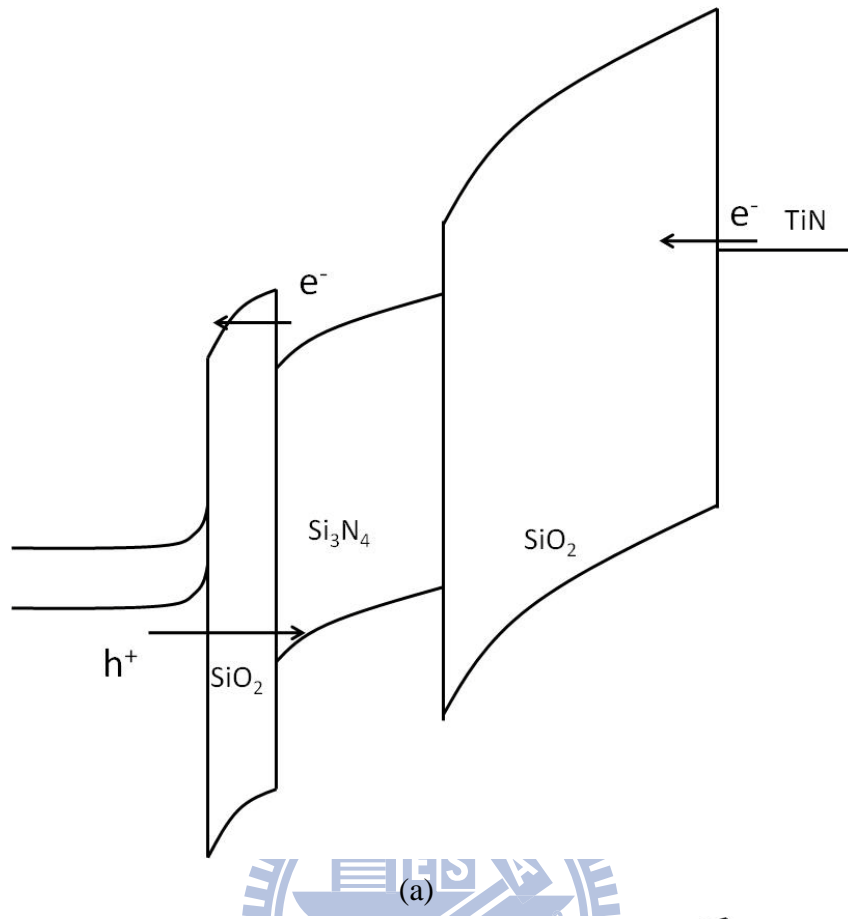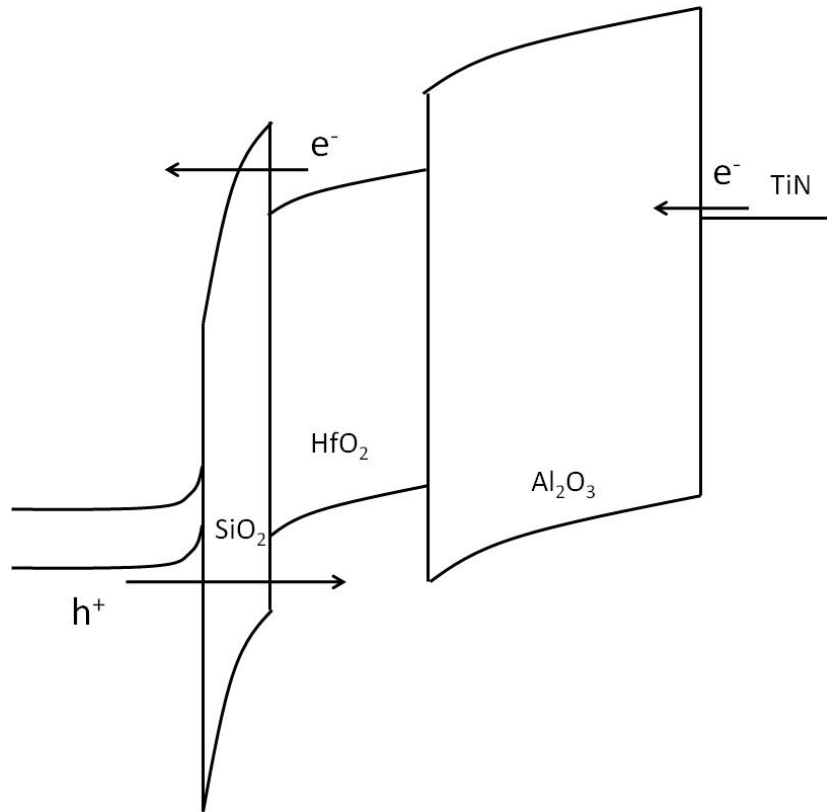
(c)

Figure 3.17. Schematic band diagrams of (a) TONOS, (b) TANOS, and (c) TAHOS devices under a negative erasing bias.
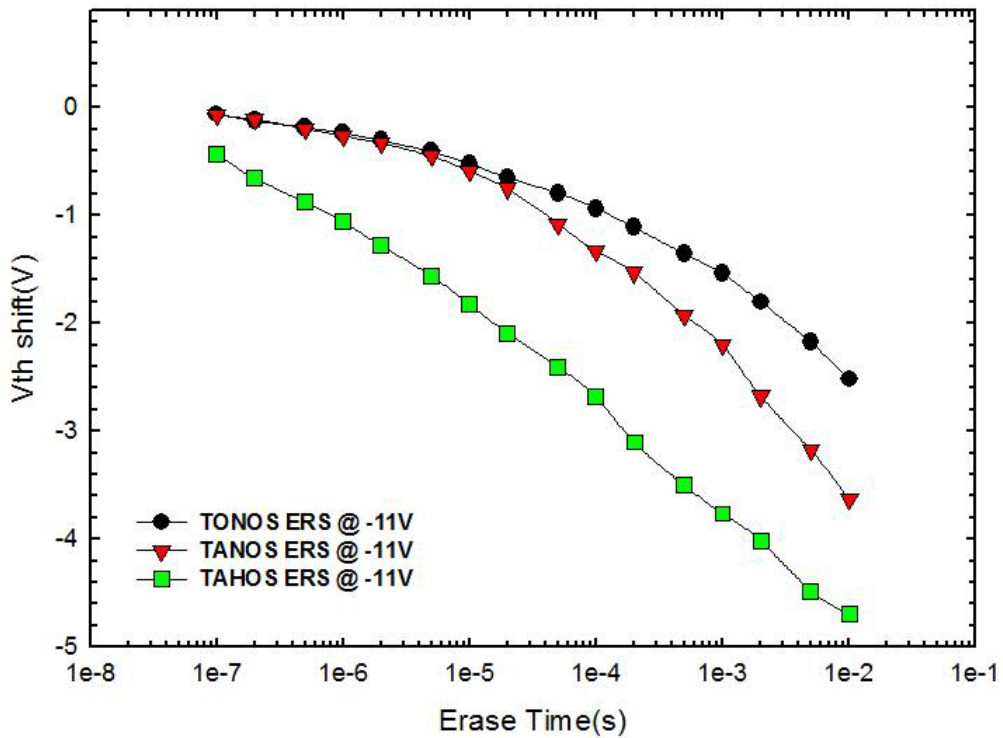
Figure 3.18.   Erasing comparisons of the three devices under the same erase bias.
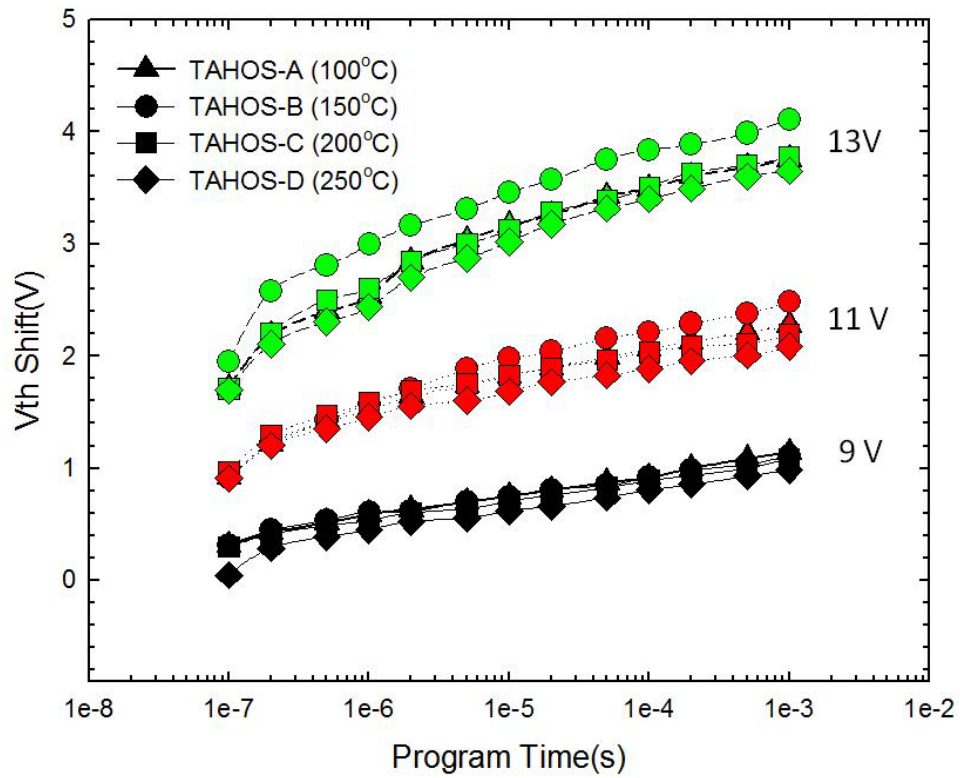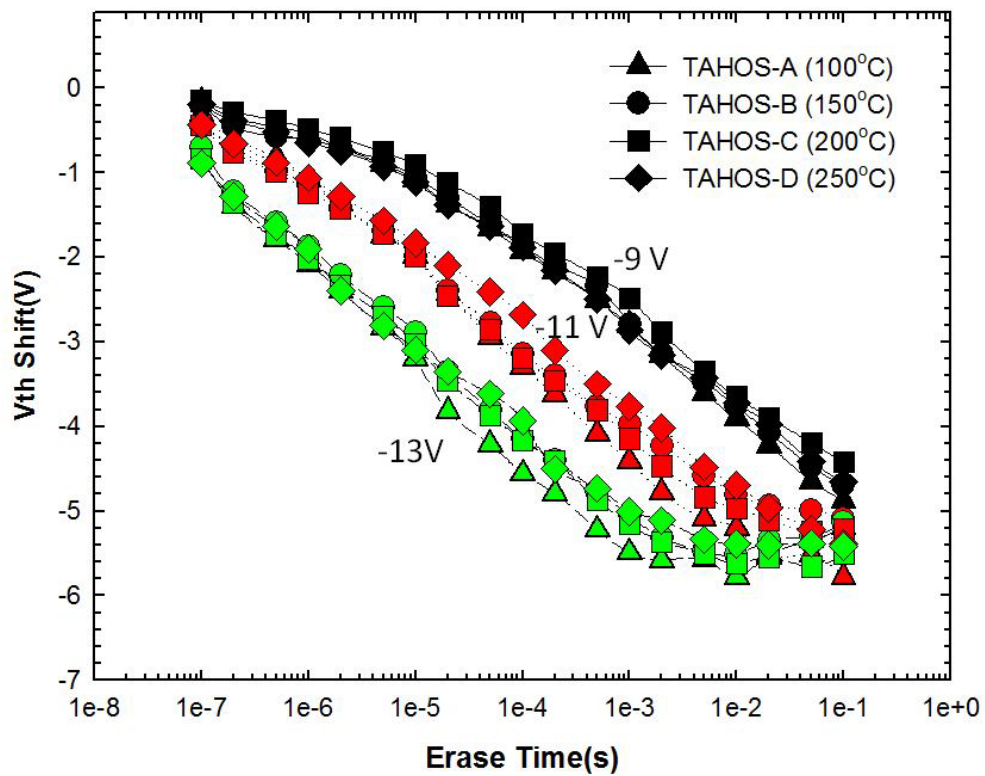
Figure 3.19.   (a) Programming and (b) erasing characteristics of TAHOS devices with HfO$_2$ storage layer deposited at various temperatures.
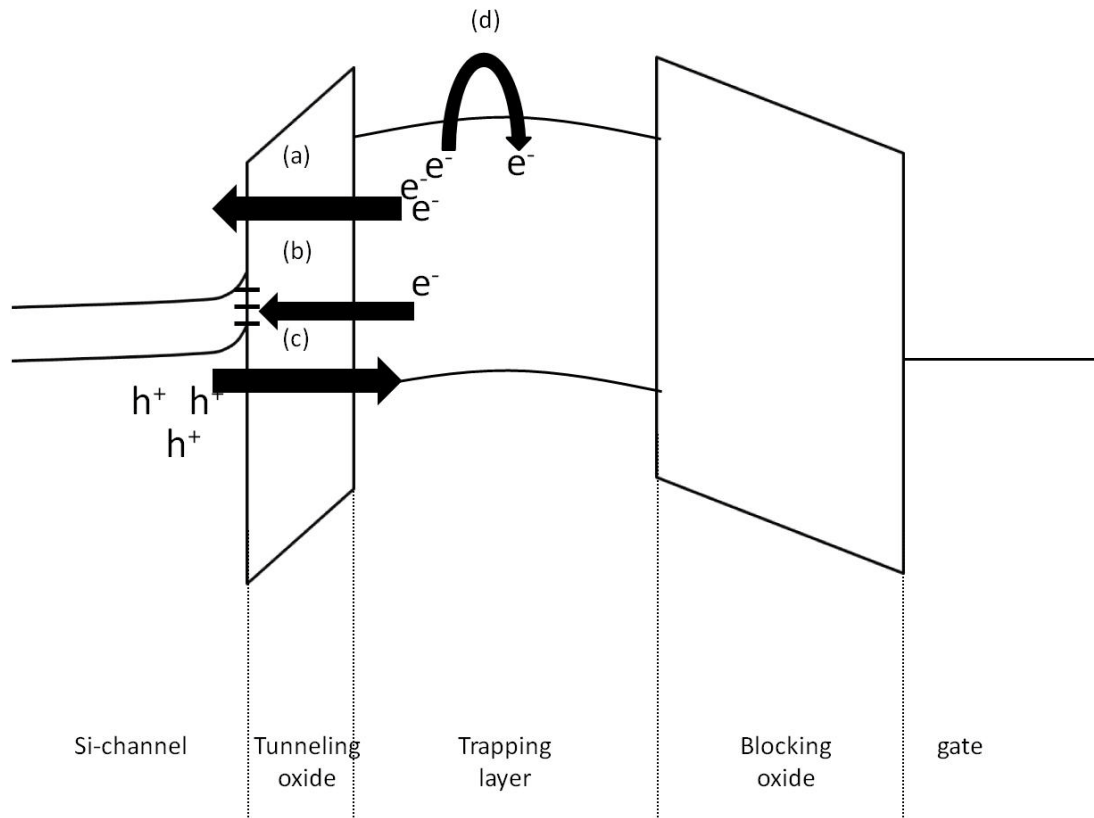
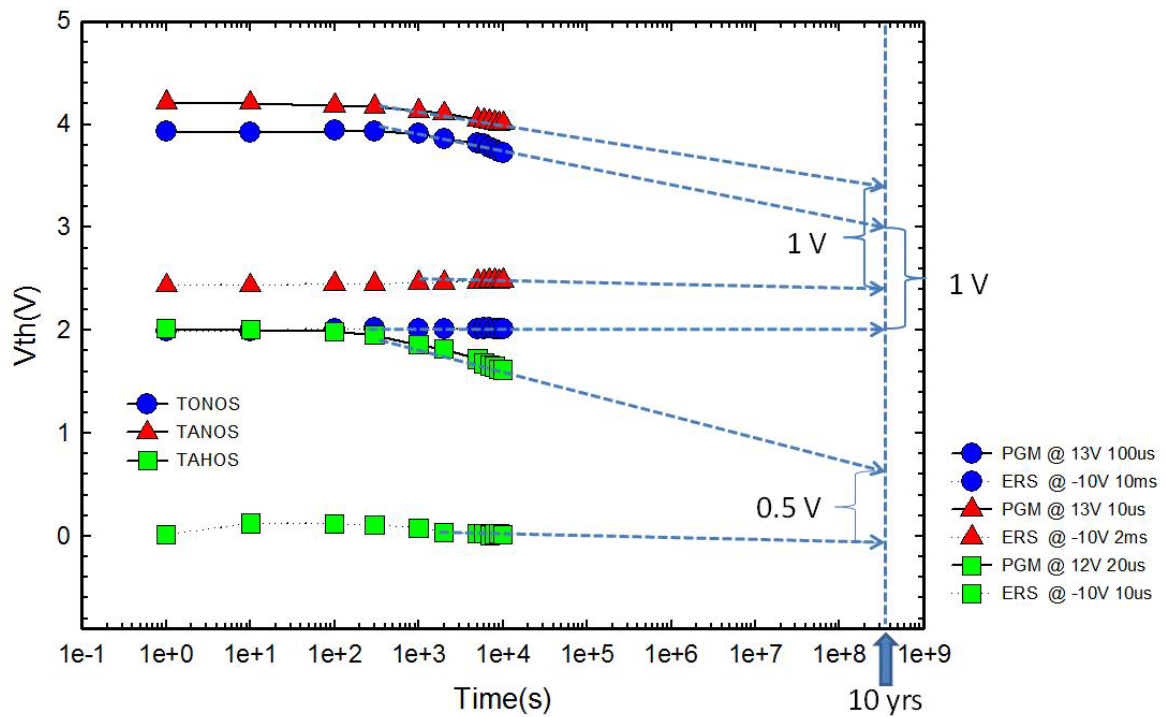Figure 3.20.   Charge loss paths under the retention condition.

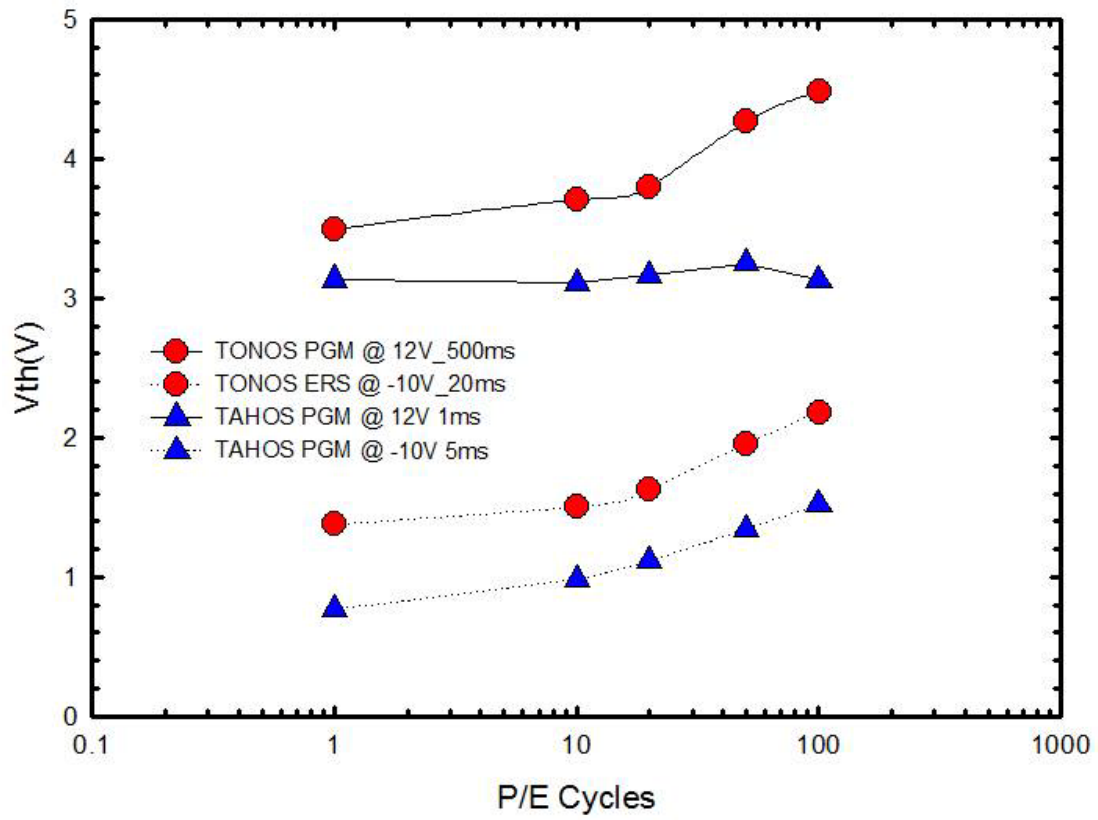Figure 3.21.   Retention characteristics of the three types of devices.
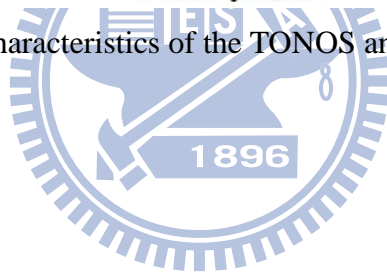
Figure 3.22.   Endurance characteristics of the TONOS and TAHOS devices.
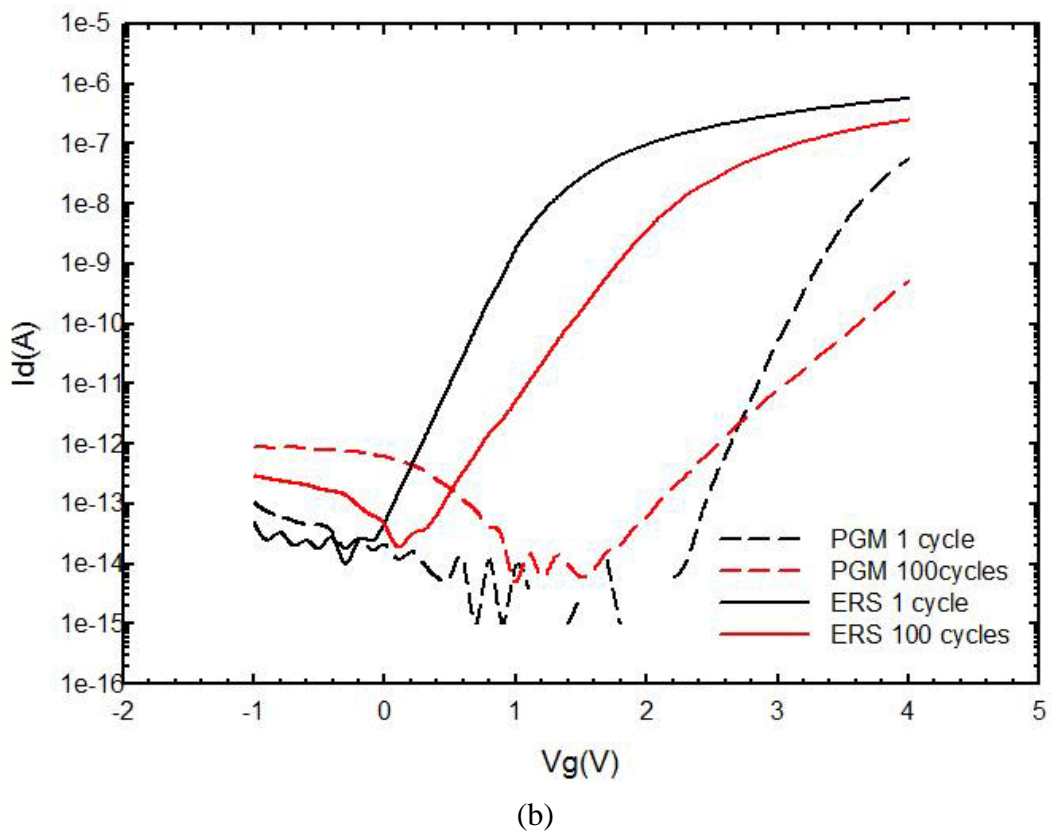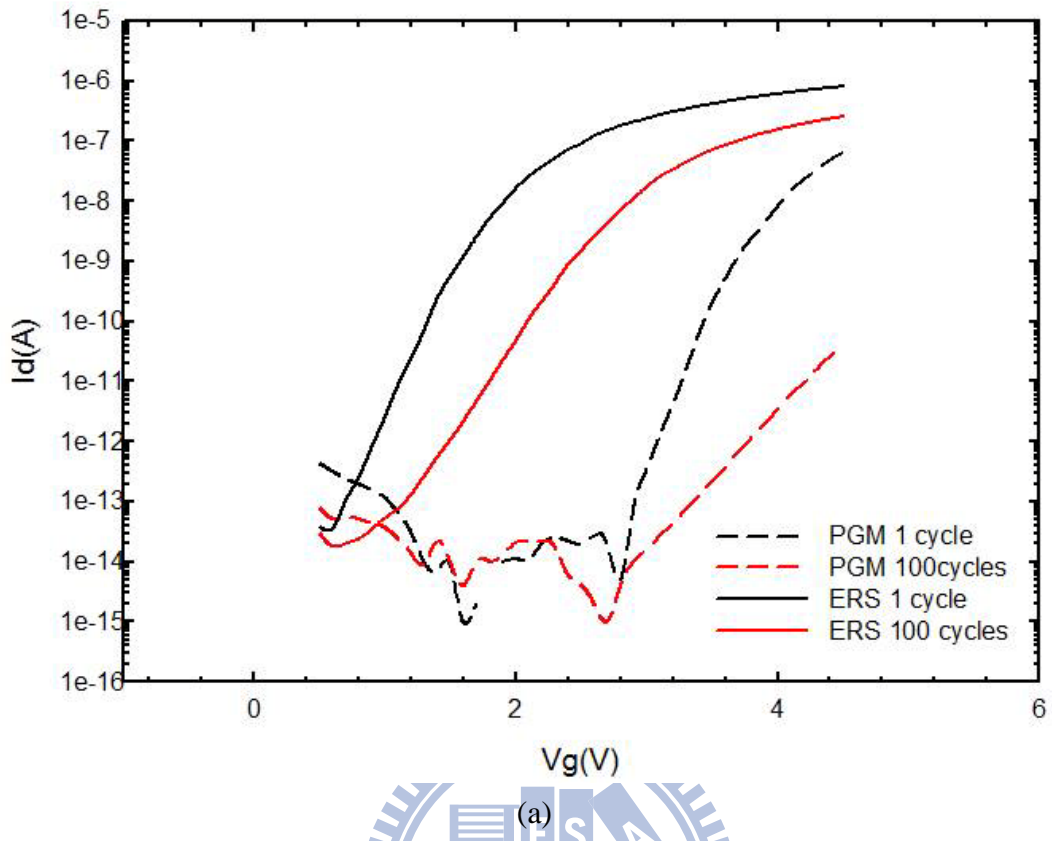
(a)

(b)

Figure 3.23. I-V plots of the (a) TONOS and (b) TAHOS devices with increasing P/E cycles.

Vita

姓　　名：　蘇段凱 Tuan-Kai Su

性　　別：　男

出　　生：　西元 1985 年 01 月 20 日

出 生 地：　台灣 新竹市
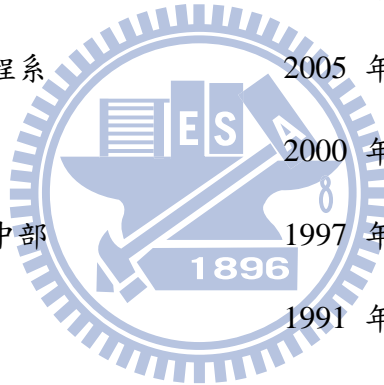
住　　址：　苗栗縣苗栗市北苗里自治路62巷38號

學　　歷：

國立交通大學電子工程研究所	2009 年 9 月 ～ 2011 年 7 月
國立交通大學電子工程系	2005 年 9 月 ～ 2009 年 6 月
私立建台高級中學	2000 年 9 月 ～ 2003 年 6 月
私立建台高級中學國中部	1997 年 9 月 ～ 2000 年 6 月
苗栗縣立建功國小	1991 年 9 月 ～ 1997 年 6 月

論文題目：

高介電常數材料的特性分析及其在多晶矽奈米線非揮發性記憶體之應用

A Study on the Characterization of High-κ Materials and their Applications to Poly-Si Nanowire Nonvolatile Memory Devices

Publication List

[1-1] **T. K. Su**, T. I. Tsai, C. J. Su, H. C. Lin, T. Y. Huang, "Fabrication and Characterization of a Junctionless SONOS Transistor with Poly-Si Nanowire Channels**,**" reported in the *IEEE International Nano Electornic Conference* (2011).